



British Geological Survey

ODA

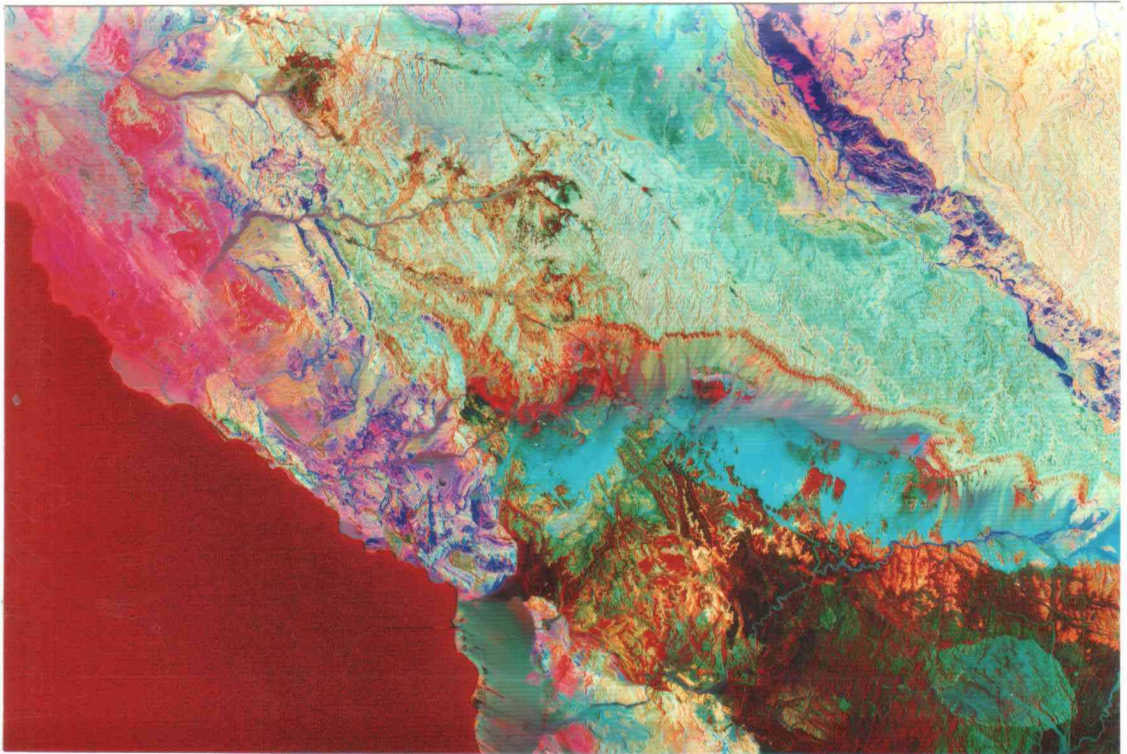
TECHNICAL REPORT WC/95/26  
Overseas Geology Series

# EXPLORATION FOR INDUSTRIAL MINERALS IN ARID AND SEMI-ARID TERRAIN USING SATELLITE REMOTE SENSING: FINAL PROJECT REPORT

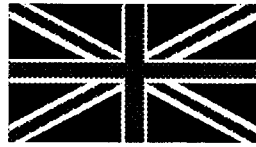
S H MARSH<sup>1</sup>, E A O'CONNOR<sup>1</sup>, D GREENBAUM<sup>1</sup>, D G TRAGHEIM<sup>1</sup>, A J W  
McDONALD<sup>1</sup>, M ABDEL RAZEK<sup>2</sup>

<sup>1</sup> British Geological Survey

<sup>2</sup> Egyptian Geological Survey and Mining Authority (EGSMA)



International Division  
British Geological Survey  
Keyworth  
Nottingham  
United Kingdom NG12 5GG



British Geological Survey

TECHNICAL REPORT WC/95/26  
Overseas Geology Series

# EXPLORATION FOR INDUSTRIAL MINERALS IN ARID AND SEMI-ARID TERRAIN USING SATELLITE REMOTE SENSING: FINAL PROJECT REPORT

S H MARSH<sup>1</sup>, E A O'CONNOR<sup>1</sup>, D GREENBAUM<sup>1</sup>, D G TRAGHEIM<sup>1</sup>,  
A J W McDONALD<sup>1</sup>, M ABDEL RAZAK<sup>2</sup>

<sup>1</sup> British Geological Survey

<sup>2</sup> Egyptian Geological Survey and Mining Authority (EGSMA)

A report prepared for the Overseas Development Administration under the  
ODA/BGS Technology Development and Research Programme, Project 91/6

*ODA classification :*

Subsector: Geoscience

Theme: G1 - Promote environmentally sensitive development of non-renewable  
natural resources

Project title: Remote sensing for industrial minerals in arid regions

Reference number: R5543

*Bibliographic reference :*

**Marsh S H and others** 1995. Exploration for industrial minerals in arid and semi-arid  
terrain using satellite remote sensing : final project report  
BGS Technical Report WC/95/26

*Keywords :*

Egypt, Namibia, industrial minerals, Landsat TM, spectral analysis, remote sensing

*Front cover illustration :*

Landsat thematic mapper satellite image of west central Sinai : colour ratio  
composite, band 5/7(red), 5/1(green), 4(blue)

© NERC 1995

Keyworth, Nottingham, British Geological Survey, 1995

# CONTENTS

## Summary

1. Introduction	1
1.1 Background	1
1.2 Scope of this report	1
1.3 Aims and objectives	2
1.4 Outline of methodology	2
1.5 Applicability, limitations and economic benefits	3
1.6 Selection of test sites	5
1.7 Collaboration and dissemination	5
2. Descriptions of techniques	7
2.1 Remote sensing and image analysis	7
2.1.1 Physical basis of the remote sensing approach	7
2.1.1.1 The use of reflectance measurements in geology	7
2.1.1.2 Remote measurement of reflectance spectra	9
2.1.1.3 The data measured by the TM sensor	9
2.1.1.4 Approaches to image analysis	11
2.1.2 Image processing	13
2.1.2.1 False colour composites	13
2.1.2.2 Atmospheric correction	14
2.1.2.3 Band ratios	16
2.1.2.4 Principal components transformation	17
2.1.2.5 Logarithmic residuals	19
2.1.3 Image interrogation	21
2.1.3.1 Description of T-Spectra software	21
2.1.3.2 The application of T-Spectra to TM analysis	22
2.2 Laboratory analysis	23
2.2.1 Introduction	23
2.2.2 Laboratory spectral analysis	24
2.2.2.1 Sample measurement	24
2.2.2.2 Data pre-processing, reduction and analysis	24
2.2.3 X-ray diffraction analysis	25
2.2.4 Discussion	25
2.3 Theoretical study of TM's spectral capabilities	26
2.3.1 Background	26
2.3.2 Resampling software	26
2.3.3 The spectra studied	28
2.3.4 Results	28
2.3.5 Discussion: practical implications	33
3. Arid test site: Egypt	34
3.1 Introduction	34
3.2 Sinai	37
3.2.1 Geology and setting	37

3.2.2	Image processing	38
3.2.3	Evaluation and field correlation	38
3.2.3.1	Brick clays	40
3.2.3.2	Kaolinite	40
3.2.3.3	Sulphate minerals	42
3.2.3.4	Carbonate minerals	44
3.2.3.5	Other lithologies	44
3.2.4	Spectral analysis	44
3.2.4.1	Insaker area	45
3.2.4.2	Mreir area	45
3.2.4.3	Discussion of the spectral analysis work	50
3.2.5	Laboratory results	50
3.2.5.1	Kaolinite beds	51
3.2.5.2	Kaolinitic sandstone	51
3.2.5.3	Gypsum	53
3.2.5.4	Olivine dolerites	53
3.2.5.5	Comments on laboratory results	53
3.2.6	Summary of main Sinai results and conclusions	54
3.3	El Fayum	54
3.3.1	Geology and setting	54
3.3.2	Image processing	55
3.3.3	Evaluation and field correlation	56
3.3.3.1	Brick clays	56
3.3.3.2	Gypsiferous clays	56
3.3.3.3	Carbonates	59
3.3.3.4	Other lithologies	59
3.3.4	Spectral analysis	60
3.3.5	Laboratory results	60
3.3.6	Summary of El Fayum results and conclusions	63
3.4	Cairo-Suez area	65
3.4.1	Geology and setting	65
3.4.2	Image processing	66
3.4.3	Evaluation and field correlation	66
3.4.3.1	Brick clays	66
3.4.3.2	Carbonates	67
3.4.3.3	Other lithologies and vegetation	67
3.4.4	Spectral analysis	69
3.4.5	Laboratory results	69
3.4.6	Summary of Cairo-Suez results and conclusions	72
3.5	General conclusions: arid areas	72
4.	Semi-arid test site: Namibia	74
4.1	Introduction	74
4.2	Okavango river area	74
4.2.1	Geological setting	74
4.2.2	Data processing	76

4.2.2.1 Conventional image analysis	76
4.2.2.2 Integration of satellite imagery and aerial photography	77
4.2.3 Evaluation and field correlation	80
4.2.3.1 Vegetation	80
4.2.3.2 Clays	81
4.2.3.3 Other lithologies	88
4.2.4 Summary of NE Namibia results and conclusions	91
4.3 Windhoek area	94
4.3.1 Geological setting	94
4.3.2 Image processing	94
4.3.3 Evaluation and field correlation	95
4.3.3.1 Area description	95
4.3.3.2 Field evaluation	95
4.3.4 Karibib-Okahandja reconnaissance	99
4.3.5 Summary of Windhoek results and conclusions	99
4.4 General conclusions: semi-arid area	102
5. Summary, conclusions and recommendations	103
5.1 Summary of approach	103
5.2 General results	104
5.3 Remaining problems and solutions	104
5.4 Conclusions and recommendations	106
Acknowledgements	107
References	108
Appendix	112
Figures	
Tables	

## Summary

Local sources of industrial minerals, including building materials, are important for industry, community development and housing programmes in many developing countries. This need has focused attention on the use of satellite remote sensing for the rapid reconnaissance of large, poorly-known areas. This report summarises the results of BGS project 91/6 (R5543) 'Remote sensing for industrial minerals in arid regions' carried out under the ODA/BGS Technology Development and Research Programme as part of the British Government's provision of aid to developing countries. The report provides a full and detailed description of work carried out and the results obtained; it is a technical account primarily intended for remote sensing geologists in developing countries wishing to implement the techniques for themselves. For the non-specialist, a synopsis is provided at the start of each chapter of the report to outline its content.

The overall objective of the project was to develop an operational methodology for reconnoitring large areas quickly and cheaply using widely available satellite data (Landsat TM). Such information can then be used to plan and target follow-up fieldwork in a more directed manner during the main exploration phase. In order to assess the general applicability and limitations of the approach, study areas were chosen in contrasting arid and semi-arid environments, Egypt and Namibia respectively. The studies attempted to apply the techniques to a limited range of industrial minerals (clays, carbonates and sulphates). Detailed field investigations were undertaken in both countries. In addition, a desk study was carried out to examine the theoretical potential for extending the method to cover a range of other materials of industrial importance.

The techniques depend on the spectral reflectance characteristics of minerals in the visible and near infrared. In arid areas lacking vegetation, the 'log residuals' method, which essentially recalculates raw satellite radiance to values approaching true reflectance, produces images that are interpretable in direct mineralogical terms. Such images may be interactively 'interrogated' on a simple personal computer using spectral analysis software, and provisional mineral identifications made. In semi-arid areas vegetation forms a complicating and limiting factor, and the successful application of the technique here depends very much on local geological knowledge to support the interpretation.

Despite certain limitations, the project has demonstrated for the first time that widely available, broadband multispectral satellite imagery can be analysed spectrally to *provisionally identify*, rather than merely *discriminate*, ground materials. The method does not depend upon the visual interpretation of image colours and so is much more objective than conventional remote sensing approaches. It is capable of targeting a range of industrial mineral occurrences as part of a reconnaissance exploration strategy. It also has significant potential for general lithological mapping. The methods work best in arid environments but can be adapted for more vegetated terrain provided the mineral occurrences sought, or their erosional products, are reasonably exposed at the surface.

## 1. INTRODUCTION

***Synopsis:*** *This chapter outlines the background, underlying rationale and scope of the project, sets out the main development objectives, and provides a general overview of the work carried out.*

### 1.1 Background

Countries in the developing world are often dependent on the local availability of industrial minerals and building materials to support industry, community development, and housing programmes. Supply and demand vary geographically but the low unit-value of many materials (e.g. clays for local brick-making) makes their transport highly expensive or impractical. There is thus a need to develop sources of supply closer to centres where they are needed. Unlike base and precious metals, which are a focus of interest for mining companies, industrial minerals do not tend to attract attention unless clear exploration targets are apparent from geological mapping or reconnaissance surveys. It may therefore fall to the national agencies to instigate the search for what can be regarded as strategic resources. The development of reconnaissance methods to assist in locating these lower value deposits is therefore needed. This project examines the use of satellite remote sensing as a rapid low-cost aid to exploration.

Desert areas commonly lack significant deposits of clays which tend to develop preferentially under more humid climatic conditions. In Egypt for example, as a consequence of over-extraction, the Government in 1986 banned the use of Nile floodplain silts for brick making, and commenced the search for alternative raw materials outside the Nile Valley. Much of the present usage comes from imports. Namibia faces a somewhat similar problem of limited sources of materials for brick making, lime and cement in areas close to centres of population. These two countries thus present the opportunity to test the approach on a limited range of industrial minerals in contrasting arid and semi-arid settings where the anticipated results can be expected to have an important benefit for the local population and industry.

### 1.2 Scope of this report

This report describes the results of BGS project 91/6 (R5543) 'Remote sensing for industrial minerals in arid regions' carried out under the ODA/BGS Technology Development and Research Programme as part of the British Government's provision of aid to developing countries. Some of the results have already appeared in print (Marsh *et al.*, 1992a and b; Greenbaum *et al.*, 1994a and b). This is a technical report in which the scientific basis of the method is described in detail in the context of case studies from Egypt and Namibia. The report provides a detailed account of the techniques, and is primarily written for those intending to implement such a system for themselves. Readers interested only in the general principles and utility of the techniques should confine their attention mainly to Chapters 1 and 5. Additionally, a synopsis is provided at the beginning of each chapter describing its contents.

### 1.3 Aims and objectives

Satellite imagery has been used extensively in the past for geological mapping and exploration for metallic mineral deposits. Attempts to use the data more quantitatively (spectrally) have been directed mainly towards the detection of hydrothermal alteration haloes associated with base and precious metals deposits (e.g. Goetz *et al.*, 1983; Amos & Greenbaum, 1989). The work by Amos and Greenbaum was carried out under a previous ODA/BGS TDR project (89/6 'Application of high resolution satellite data to mineral and geothermal resource exploration'). The present work seeks to adapt and develop these techniques to the search for lower unit-value, bulk industrial minerals.

The **immediate aim** of the study was to examine whether such techniques could be applied to the search for a limited range of minerals (clays, sulphates & carbonates) in Egypt and Namibia, as examples of arid and semi-arid countries. The **wider objective** was to develop a practical, low-cost, operational methodology for exploring large areas of poorly known terrain, quickly and efficiently, using widely available satellite data. Such information could then be used by developing countries either to develop new resources for themselves or to stimulate private sector interest.

The original focus of the work was the detection of clays, sulphates and carbonates, and the main part of this report concentrates on these minerals. Such materials are spectrally distinct as a class on Landsat imagery and can thus be discriminated in arid and semi-arid regions where masking by vegetation is not a problem. The intention here was to develop specific image processing and interpretation techniques that could discriminate, and provide a provisional identification of, the individual minerals or mineral groupings. It is not suggested that the current generation of satellite data could be used to remotely identify economic deposits, but rather that such data can help to target anomalies for field follow-up. By testing the method in an arid and a semi-arid area both the applicability and the limitations of the technique could be assessed. The techniques have, of course, much wider application beyond the two study areas, e.g. elsewhere in Africa, in parts of Asia, and Latin America.

More generally, the techniques have potential for the discrimination and identification of a range of other geological and non-geological materials. In a second phase of the work, a desk study was carried out to determine from a theoretical viewpoint the extent to which the methods could be more widely applied to other industrial minerals. The results of this exercise are also described.

### 1.4 Outline of methodology

All materials show reflectance properties which vary according to wavelength across the electromagnetic (EM) spectrum. In the visible to reflected infrared regions, rocks and minerals exhibit subtle features which can be measured in the laboratory using sensitive instruments called spectroradiometers. Of particular interest are low-reflectance (absorption) features that occur in the shortwave infrared (SWIR) region since these can be diagnostic of mineral groups or individual mineral species. Although current satellite sensors do not possess the spectral resolution to make precise mineral identifications possible, under the right conditions imagery, such as Landsat Thematic Mapper (TM), can be used to recognize the presence of higher-than-average surface concentrations of particular mineral groups (such

as clay minerals). This is the approach previously used to detect rock alteration haloes. The intention here was to determine the extent to which this concept could be extended beyond mere *discrimination* towards the (provisional) *identification* of surface minerals.

The Landsat TM sensor records reflected radiation in six spectral bands (band 1-5 and 7). Band 7 (hereafter referred to as TM7) covers the SWIR region where important absorptions occur. Although the broad spectral width of this band (2.08-2.35  $\mu\text{m}$ ) is not sufficient to determine uniquely the individual minerals causing absorption, the very existence of low TM7 reflectance can indicate a geological anomaly and, in the appropriate geological environment, this can be a strong indicator of mineralisation. Because satellite images are composed of digital numbers, the data can be manipulated mathematically to enhance features of interest. The simplest approach is to calculate the ratio of TM7 against another band in which reflectance tends to be uniformly high, such as TM5. In a 5/7 ratio image, low reflectance values in TM7 result in high ratio values which appear as bright areas on the image. By combining the 5/7 ratio with two other ratios, a ratio false-colour composite (FCC) image can be produced which can further aid discrimination.

Unfortunately, it is not only minerals and rocks that exhibit TM7 absorption. Much of the Earth's surface is covered by soils and vegetation, and green vegetation can produce similar spectral responses to certain key minerals (at the coarse resolution of the TM sensor); thus, it is easy to confuse clay with vegetation on a simple ratio image. For this reason, more sophisticated approaches are needed often involving complex transformations of the data. In this project, various techniques were used to enhance the responses of interest. The most useful of these involved converting the satellite signal to values approaching laboratory reflectance. Having done this, the data could then be assessed spectrally. Despite their coarse spectral resolution, these 'pseudospectra' hold the potential for provisional mineral identification.

### **1.5 Applicability, limitations and economic benefits**

Despite the complexities of the underlying processing, sophisticated software is now available on low-cost image analysis computer systems. Hardware/software have become much cheaper in recent years, and many developing countries are establishing small image processing facilities of their own, often based on powerful workstations. Another development emphasized in this project is the use of image 'interrogation' software which allows the geologist to interactively extract 'spectral' information from the image. This makes image interpretation less subjective by reducing the reliance on visual differences. The technique does not purport to be a truly quantitative approach but the examination of images in spectral terms allows a much more consistent and objective approach to interpretation.

The value of implementing the techniques described here would be an efficient, cost-effective means of providing preliminary regional industrial minerals information. Economic benefits are likely to be seen mainly in the provision of cheap local materials for housing and small industry.

The method is mainly applicable in arid and semi-arid regions where remote sensing works well and where certain minerals are in short supply (Figure 1.1). The techniques are not suited to heavily vegetated areas. Besides minerals, the methods could be applied to general

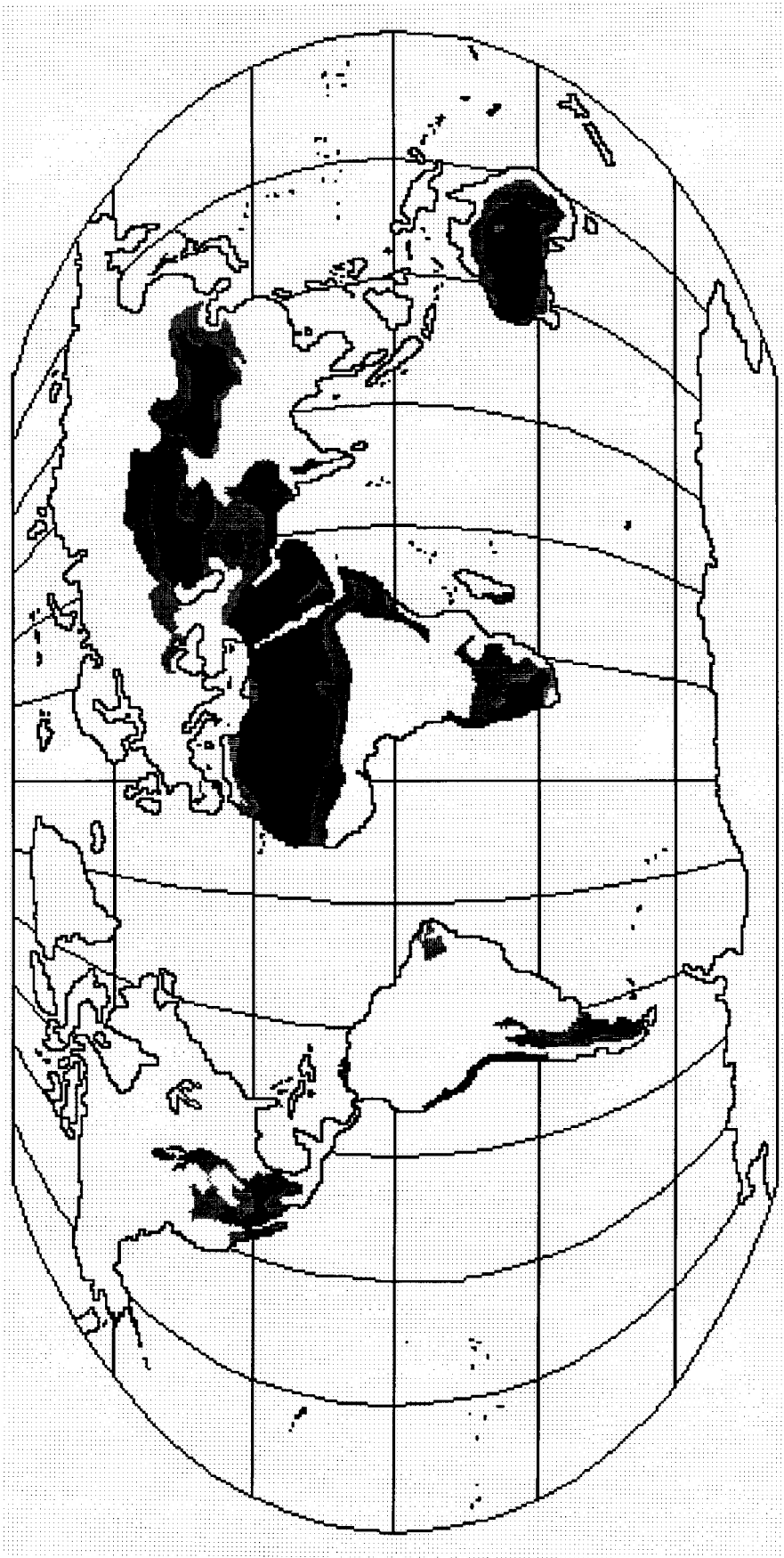


**Figure 1.1** Worldwide distribution of arid and semi-arid areas.

geological mapping. The potential exists to extend the technique to other sectors of relevance to development such as land-use planning or pollution studies.

### 1.6 Selection of test sites

In order to assess the general applicability and limitations of the technique, study areas were chosen in two contrasting environments (arid and semi-arid). The main test site for the arid study was the Sinai region of Egypt where exposure is good and vegetation is virtually absent (Marsh *et al.*, 1992a). Additional sites nearer to centres of population around Cairo, Suez and El Fayum were also examined (Figure 1.2A). For the semi-arid study, two test sites in Namibia were chosen (Figure 1.2B), the first along the Okavango River flood plain in north eastern Namibia and the second in central Namibia east of the capital Windhoek. Both Egypt and Namibia are countries where clays are needed for local housing and industrial uses, but where resources are scarce. Whereas Egypt represents a nearly ideal situation for remote sensing in terms of rock exposure and lack of vegetation, Namibia is representative of areas with moderate amounts of vegetation cover.

### 1.7 Collaboration and dissemination

Each of the studies was carried out with the help and collaboration of the national geological survey; in Egypt, the Egyptian Geological Survey and Mining Authority (EGSMA), and in Namibia the Geological Survey. These organisations collaborated at various levels in the work, as well as providing logistical support, technical facilities, and analyses of samples.

Some training was provided during the course of fieldwork and through local seminars. In addition, early results were presented at several international scientific meetings in New Zealand, the USA and Britain, and published as follows:

1. Marsh, S.H., O'Connor, E.A.O. and Greenbaum, D. 1992. Industrial minerals exploration in Egypt using Landsat TM. *Proceedings of the Sixth Australasian Remote Sensing Conference*, 3, Wellington, New Zealand, 314-323.
2. Greenbaum, D., Marsh, S.H., Tragheim, D.G. and O'Connor, E.A. 1994. Reconnaissance for industrial minerals using satellite remote sensing. *In: (Eds Mathers, S.J. and Notholt, A.) Industrial Minerals in Developing Countries*, Report 18, BGS/AGID, 55-66.
3. Greenbaum, D., Marsh, S.H., O'Connor, E.A.O, McDonald, A.J.W. and Tragheim, D.G. 1994. Advances in industrial minerals mapping in arid and semi-arid environments. *Proceedings of Tenth Thematic Conference on Geologic Remote Sensing, San Antonio, Texas, 9-12 May 1994*, I115-126.

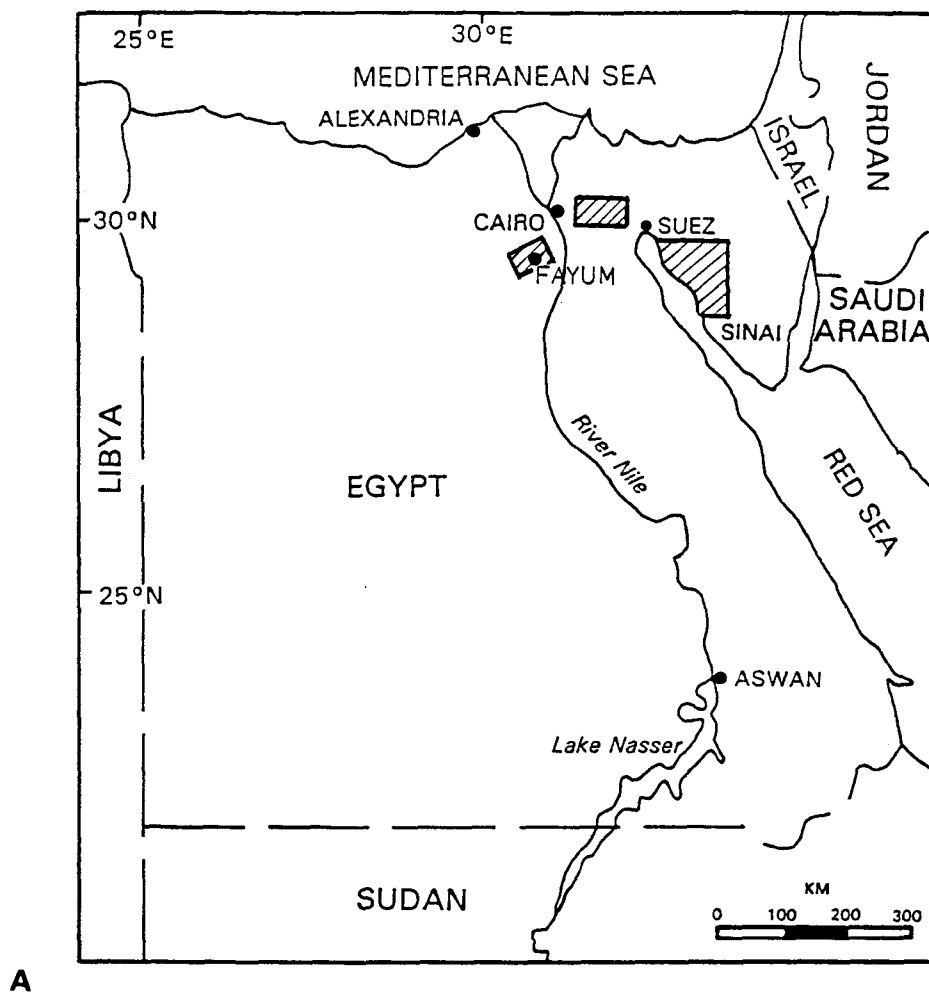
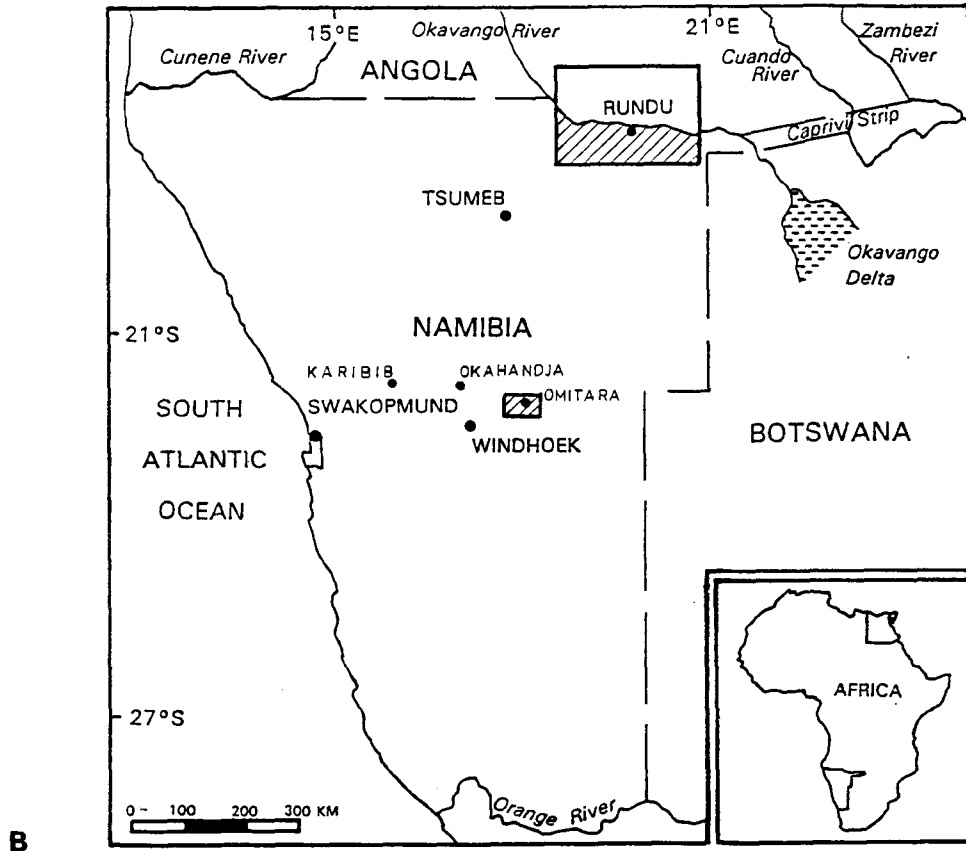


Figure 1.2 Study sites in Egypt (A) and Namibia (B).

## 2. DESCRIPTIONS OF TECHNIQUES

*Synopsis: This chapter describes the characteristics of satellite data, and provides a technical account of the underlying remote sensing theory as applied to mineral identification. Various image processing techniques are described in detail from both a theoretical and practical viewpoint, and a general assessment made of their comparative usefulness. Laboratory analysis techniques, used to provide mineralogical explanations for the variations detected in the images, are described. Finally, an examination is presented of the theoretical potential of the methods to identify a range of other industrial minerals and rocks. This chapter is intended mainly for the specialist remote sensing geologist or image analyst proposing to implement the techniques.*

### 2.1 Remote sensing and image analysis

#### 2.1.1 Physical basis of the remote sensing approach

Remotely sensed data, though commonly presented as an image, can be considered quantitative in the same way as other geophysical measurements. This is because, whilst the data are affected by the topography of the ground surface, they also record a fundamental physical property of the surface - its reflectance. The reflectance properties of rocks and minerals can be used to identify them and so are of potential use to geologists.

##### 2.1.1.1 The use of reflectance measurements in geology

Spectroradiometers can be used to measure the reflectance of incident EM energy from a rock or mineral between 0.4 and 2.5  $\mu\text{m}$  at high resolution, either in the laboratory or in the field. Reflectance values plotted against wavelength commonly show the presence of *absorption features*, representing wavelengths at which less incident energy is reflected due to interactions with the chemical constituents of the surface. The shape of the reflectance spectrum in general, and of the absorption features in particular, depend on the chemical composition of the sample and can be used to uniquely identify the mineral or mineral group.

Between 0.4 and 2.5  $\mu\text{m}$ , energy incident on a surface is absorbed to varying degrees by the electrons within atoms and molecules and undergoes either electronic or vibrational transitions. The most important **electronic transitions** are crystal field effects and charge transfer transitions. In the former, electrons absorb energy as they change to a new energy level; examples occur in minerals containing  $\text{Fe}^{2+}$  and  $\text{Fe}^{3+}$ , which have diagnostic absorption features in the near infrared wavelength region. The latter are due to the transfer of electrons from one ion to its neighbour, a good example being the Fe-O charge transfer which produces absorption in the visible blue-green wavelengths and hence causes the red colour of iron oxides. The minerals displaying Fe-related absorptions include weathering products like hematite and goethite, and rock-forming minerals such as olivines, pyroxenes and the amphiboles; example spectra are shown in Figure 2.1. **Vibrational transition** overtones are responsible for features at slightly longer wavelengths in the shortwave infrared

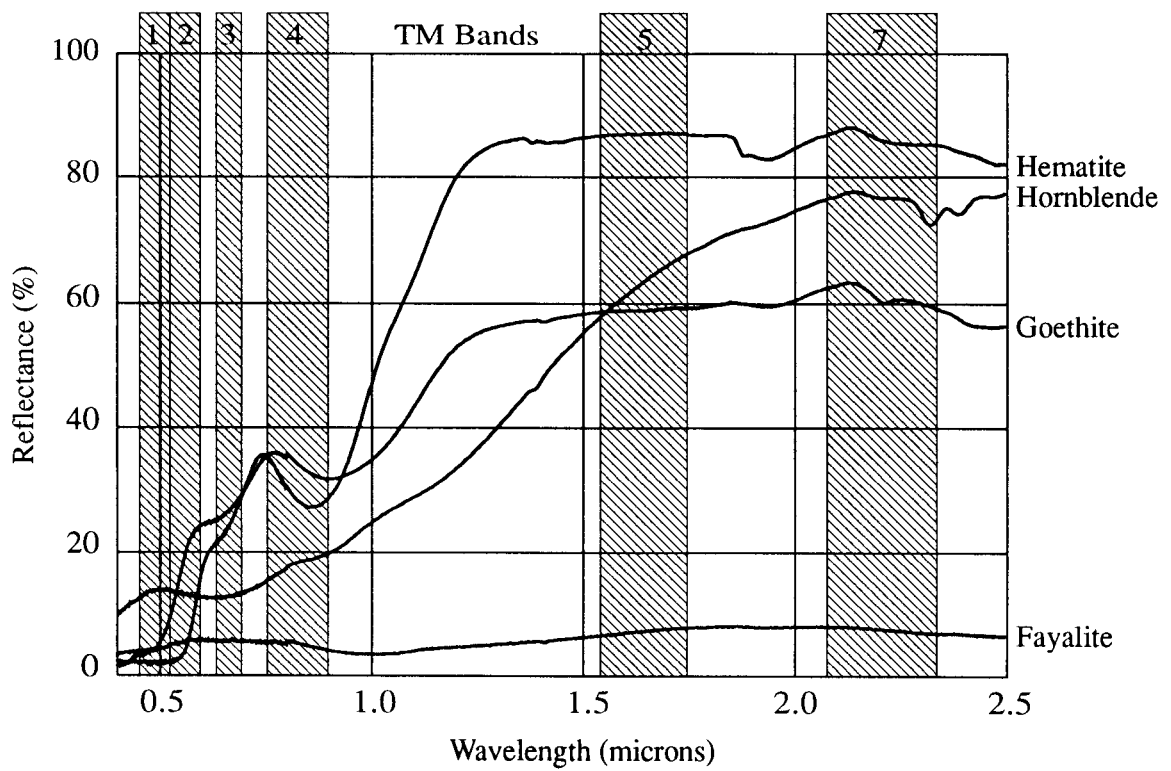


**Figure 2.1** Reflectance spectra of minerals with absorptions due to iron.

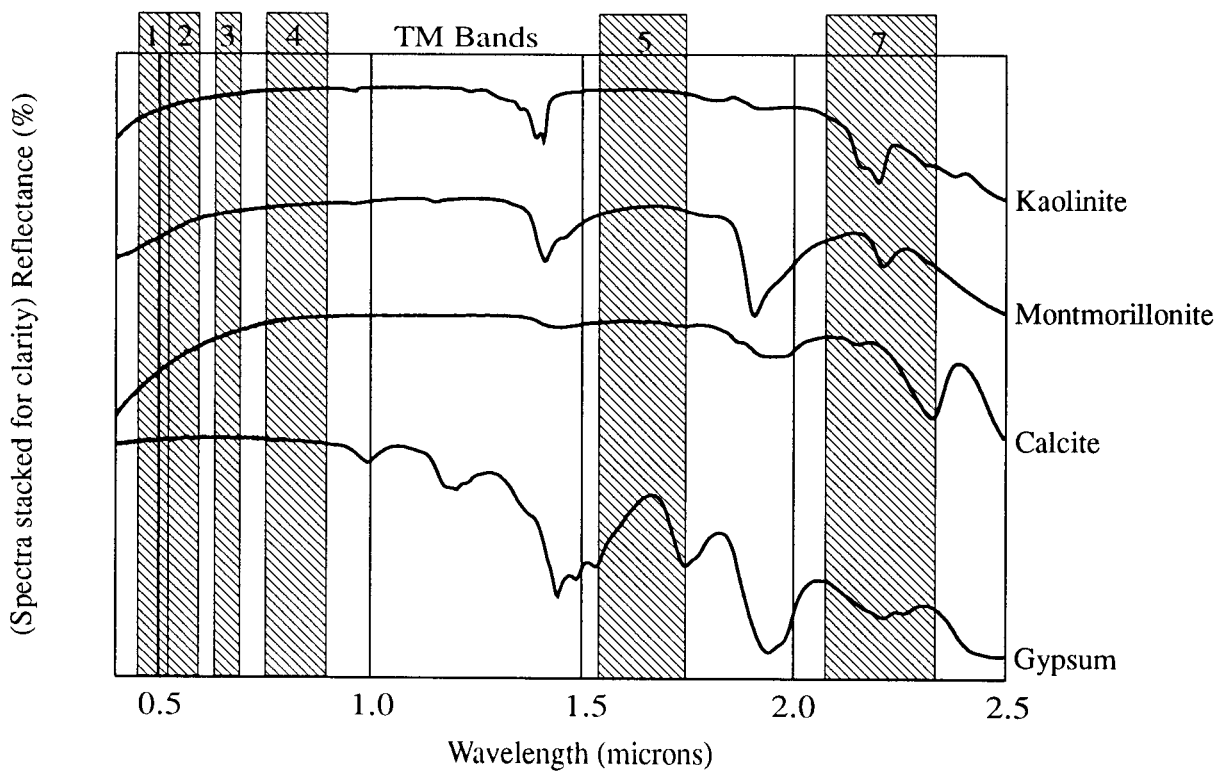


**Figure 2.2** Reflectance spectra of typical clay, carbonate and sulphate minerals.

(SWIR) region. The most important molecules responsible for such interactions are OH, present in rocks in mineral structures or as molecular water, and CO<sub>3</sub>. OH commonly combines with Al, Fe and Mg, so that the spectra of kaolinite, dickite, chlorite, talc, montmorillonite, muscovite and epidote all have absorptions related to vibrational transitions. CO<sub>3</sub> produces absorptions due to vibrational transitions in calcite, dolomite and other carbonates. Figure 2.2 shows some examples of spectra that exhibit absorptions due to vibrational transitions.

In summary, the spectral reflectance properties of minerals in the 0.4 to 2.5  $\mu\text{m}$  wavelength region are well known; they have been described in a series of papers by Hunt and co-workers, summarised in Hunt (1977). Table 2.1 shows the wavelength positions of the most important absorptions for geologists, the transitions and elements responsible for them, and the minerals and rocks of which these are important constituents.

### **2.1.1.2 Remote measurement of reflectance spectra**

The identification of minerals using laboratory or field spectrometry is now an established technique. Data from airborne spectrometers, once they have been processed to reflectance and analysed as spectra, make possible remote mineral identification (e.g. Huntington *et al.*, 1989). However, unlike laboratory spectra, remote measurements display almost complete absorption of EM energy by atmospheric water vapour at certain wavelengths. This masks important portions of the near infrared and SWIR wavelength region in remote sensing imagery; the unaffected region critical for the remote identification of many minerals lies between 2.0 and 2.5  $\mu\text{m}$ . Further complications are caused by the presence of even small amounts of vegetation, which masks the signal from rocks and minerals and produces a similar spectral signal in the SWIR to some minerals.

Unfortunately, remote mineral identification using satellite data is not possible because current satellite sensors measure too few spectral bands and have too coarse a spectral resolution. The crude spectra which can therefore be produced from satellite data such as Landsat TM, whilst indicating the presence of absorbing minerals, do not permit the precise position and shape of the mineral absorptions to be determined. For example, between 2.0 and 2.5  $\mu\text{m}$  the Landsat TM has a single band (TM7) covering the range 2.08-2.35  $\mu\text{m}$ . Thus, whereas satellite data can be used to recognize higher than average ground concentrations of absorbing minerals, the data do not allow the identification of the actual minerals present. Consequently, few researchers have tried to analyse satellite data in a quantitative manner. However, despite the limited spectral resolution of the data, it is possible to identify broad mineral groupings: this approach offers a considerable advance over standard satellite interpretation techniques.

### **2.1.1.3 The data measured by the TM sensor**

The TM is a scanning radiometer - a passive remote sensing instrument which records the Earth's radiant EM energy, modified by the atmosphere, in seven bands, three in the visible (TM1-3), one in the near infrared (TM4), two in the short wave infrared (TM5 and TM7) and one in the thermal infrared wavelength region (TM6) (Figure 2.1). The response of the detectors is recorded as digital numbers (DN) in the range 0-255. Each measurement is made over an area on the ground 28.5 m by 28.5 m, referred to as a 'pixel'. (In the thermal

**Table 2.1** Some common absorption features, their causes and the minerals and lithologies with which they are associated (sources: Hunt (1977), CSIRO, Geoscan, Grove et al (1992)).

Absorption ( $\mu\text{m}$ )	Cause	Minerals	Lithologies
0.4 - 0.55	Charge Transfer, Fe	Limonite	Almost any rock containing Fe which can be released in solution, particularly basic rocks such as dolerite and basalt.
Near 0.48	Charge Transfer, Fe	Goethite	
Near 0.58	Charge Transfer, Fe	Hematite	
0.68	Crystal Field Effect, Fe	Goethite	
Near 0.84	Crystal Field Effect, Fe	Hematite	
0.90 - 0.92	Crystal Field Effect, Fe	Goethite	
0.86 - 0.92	Crystal Field Effect, Fe	Limonite	
0.8 - 1.2	Crystal Field Effect, Fe	Olivine/Pyroxene	Basic rocks
Near 1.4	Vibrational Overtones: H <sub>2</sub> O O-H	Quartz, Gypsum Montmorillonite  Kaolinite Muscovite	Acid rocks, sandstone, schist, evaporite, weathered rocks.
1.9 - 2.0	Vibrational Overtones: H <sub>2</sub> O	Gypsum, Quartz Montmorillonite	Acid rocks, sandstone, evaporites.
Around 2.2	Vibrational Overtones: Al-OH  H <sub>2</sub> O	Kaolinite Muscovite  Gypsum Montmorillonite	Acid rocks, sandstone, schist, evaporites.
2.3 - 2.4	Vibrational Overtones: Mg-OH/Al-OH  C-O	Amphibole Talc Chlorite Epidote  Calcite	Metamorphic rocks, carbonates.

infrared the pixel size is 120 m by 120 m but this study makes no use of TM6). The sensor records the data as images each covering an area of 185 x 170 km, and each image is repeatedly acquired every 16 days.

Before analysing the Landsat TM data in a quantitative manner, the physical nature of the data must be considered. In the wavelength range 0.4-2.5  $\mu\text{m}$  covered by TM1-5 and TM7, almost all of the Earth's radiant energy comprises solar irradiance reflected back toward the sensor by the Earth's surface or by the atmosphere. The data acquired by the Landsat TM thus consist of two components; (i) the reflectance signal from the Earth's surface modified twice by passage through the atmosphere, and (ii) the reflectance of the atmosphere itself, termed the *additive path radiance*. The sum of these two values is modified again during recording by gains and offsets which ensure the final measurement falls within the instrument's radiometric sensitivity. This complicated verbal description of the measurement made at the satellite can be summarised by Figure 2.3 and the following equation:

$$X_{\lambda} = (E_{\lambda}t_{\lambda}A\rho_{\lambda} + a_{\lambda})G_{\lambda} + O_{\lambda} \quad (2.1)$$

which rearranges to

$$X_{\lambda} = E_{\lambda}t_{\lambda}A\rho_{\lambda}G_{\lambda} + a_{\lambda}G_{\lambda} + O_{\lambda} \quad (2.2)$$

where

$X_{\lambda}$	=	Radiance measured at sensor at wavelength $\lambda$
$E_{\lambda}$	=	Irradiance of source reaching surface at wavelength $\lambda$
$t_{\lambda}$	=	Atmospheric transmittance (up) at wavelength $\lambda$
A	=	Slope and aspect based effects for the surface
$\rho_{\lambda}$	=	Reflectance of surface at wavelength $\lambda$
$a_{\lambda}$	=	Atmospheric path radiance at wavelength $\lambda$
$G_{\lambda}$	=	Gain applied at the sensor at wavelength $\lambda$
$O_{\lambda}$	=	Offset applied at the sensor at wavelength $\lambda$

#### 2.1.1.4 Approaches to image analysis

Simple false-colour composites (FCCs) of TM data have been successfully used to analyse geological problems (e.g. Qari, 1989), but do not fully exploit the information contained in the data. Much of this information relates to albedo and is highly correlated between different wavelength bands. The albedo contains information on topography useful for structural mapping, but the discrimination and identification of different lithologies and minerals relies on emphasizing or retrieving the reflectance so that analysis of the mineral-specific absorption features can be carried out. Approaches to image analysis may be split into those aimed at increasing visual *discrimination* when the data are displayed as an image and those which seek to achieve *identification* by retrieving the reflectance ( $\rho_{\lambda}$ ) from Equation 2.2.

In Equation 2.2 the factor A is large and correlated between wavelengths. Discrimination is improved by data processing techniques which reduce this correlation. The simplest method is to contrast stretch the data, which in effect introduces a further gain and offset designed

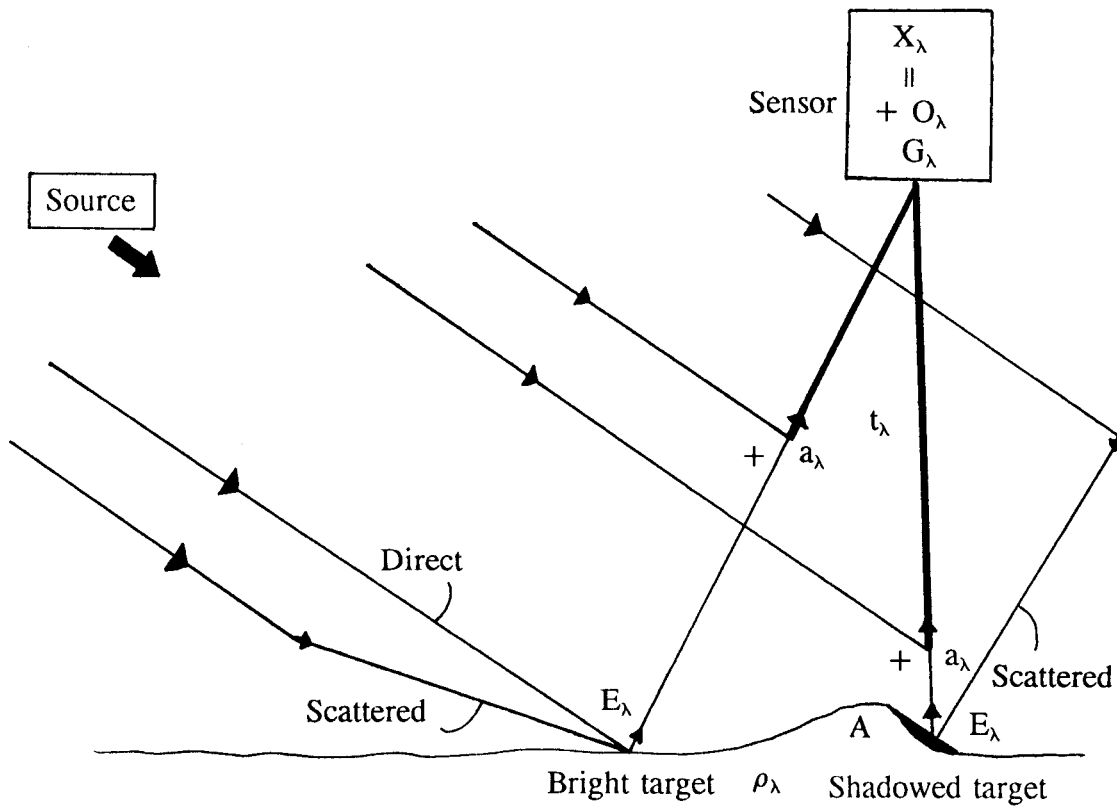


**Figure 2.3** Schematic representation of the measurement made by the TM sensor.

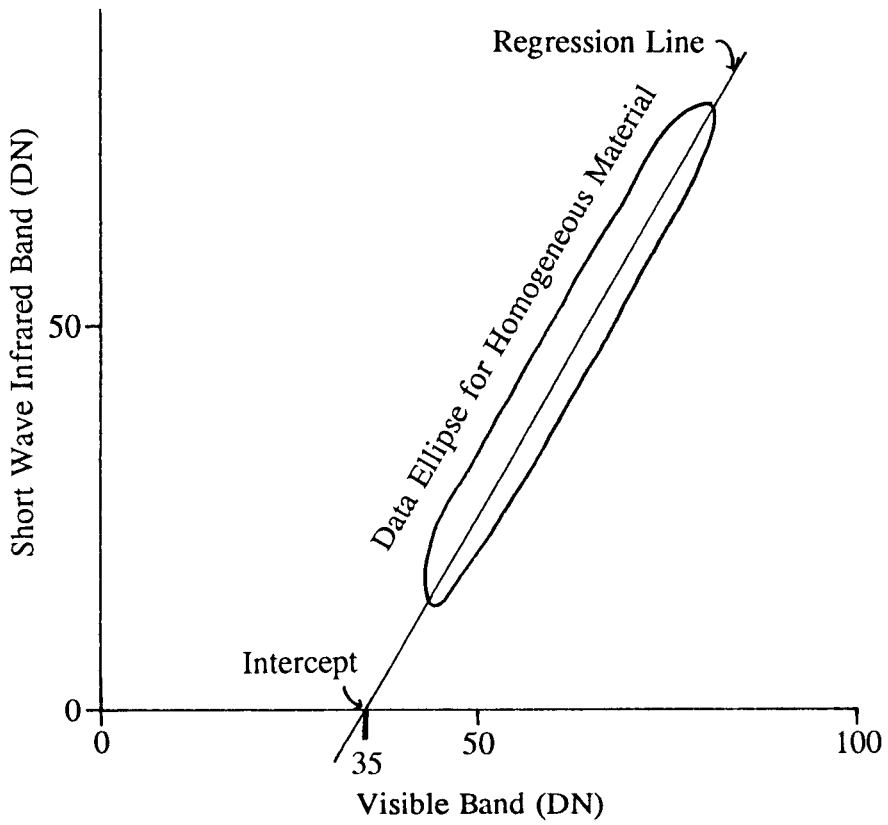


**Figure 2.4** The principle behind the Regression Method for atmospheric corrections.

to improve on the values set at the sensor. This method can also be used to remove the atmospheric path radiance and the other additive components in Equation 2.2 ( $a_\lambda G_\lambda$  and  $O_\lambda$ ). Band ratioing reduces correlation between wavelengths by removing the factor A, which is constant at all wavelengths, by dividing values at one wavelength by those at another. Techniques such as principal components analysis aim to reduce correlation, and hence to increase visual discrimination, by transforming the data's statistical distribution. They have proved successful at highlighting the uncorrelated information of value to geologists but the images are difficult to interpret in any quantitative manner.

In the visible, near infrared and shortwave infrared regions of the spectrum, identification of lithologies or minerals can only be achieved if the parameter reflectance ( $\rho_\lambda$ ) is retrieved from the data and the spectrum of reflectance against wavelength plotted (Hunt, 1980). The geologically significant information often consists of subtle absorption features in the spectrum at particular wavelengths which may form as little as 4% of the signal (Green *et al.*, 1985). The values of  $\rho_\lambda$  contained in the data are modified by several factors, many of little or no geological interest; logarithmic residuals (Green and Craig, 1985) is one technique which aims to retrieve  $\rho_\lambda$  by removing the non-geological factors ( $E_\lambda$ ,  $t_\lambda$ , A and  $G_\lambda$  in Equation 2.2) after noise, offsets, gains, and additive path radiance have been removed.

## 2.1.2 Image processing

### 2.1.2.1 False colour composites

FCCs are created by combining three spectral bands on a computer display monitor. One band is assigned to each of the red, green and blue colour guns of the monitor and the resultant colours are dictated by the relative brightness of each pixel in each of the three bands. This technique is helpful to the analyst since information recorded at wavelengths not normally perceived by the human eye (reflected infrared) can be viewed in colour combinations which assist the discrimination of different target materials. With some knowledge of spectral signatures it is possible to predict the likely identity of some of the materials from the resulting colours.

From the six reflective bands of the Landsat TM sensor it is possible to form 20 different composites. In reality, however, there are 120 composites since the three bands can be assigned to the three display colours in six different ways. There are guidelines for defining the composite combination, and these can help reduce the number to be examined before selecting the most informative. For example, placing the 'noisiest' band on the blue channel can improve the appearance of the composite considerably. Also, a number of composites appear similar due spectral similarities between certain bands. For example, in vegetated terrains TM 4,5,7 and TM 4,5,3 composites look similar because of absorptions in TM7 and TM3 which are both characteristic of vegetation although caused by different mechanisms.

To extract the maximum information from such a display, it is often necessary to carry out further processing to enhance the image. The two most common procedures are *contrast stretching* and *spatial filtering*.

Many parts of the Earth have only a limited range of surface materials. This results in the recorded images exhibiting low contrast since the satellite sensors have to be capable of

recording information from all types of targets ranging from dark water bodies to bright, reflecting sands. The process of contrast stretching aims to increase the contrast of the data by distributing the recorded values across the monitor's full display range. There are various ways to do this; the simplest uses a linear transformation to distribute the data so the minimum becomes 0 and the maximum 255. Contrast stretches can be tailored to each image or even specific parts of an image.

Whereas contrast stretching is used to improve the radiometric quality of the image, spatial filtering is used to change the spatial characteristics. Filters can be used to remove noise from an image by smoothing, to detect edges (i.e. rapid changes in brightness) which may represent lines or boundaries of features, or to sharpen images. The latter process is geologically useful since linear features relating to faults and fractures are enhanced while the overall geological context is retained.

### **2.1.2.2 Atmospheric correction**

The additive atmospheric path radiance, described in section 2.1.1.3, contains no information about the target and is an unwanted component in the received signal. For certain image processing procedures (e.g. colour compositing, filtering), its presence does not adversely affect the result. However, for quantitative procedures such as band ratioing or log residuals transformation, the atmospheric path radiance modifies the calculated values and must be removed. Because of its importance in these techniques, it is reviewed in some detail.

To remove the additive atmospheric component from an image, a correction value is subtracted from each wavelength band of every pixel. The most rigorous procedure for calculating the correction values is to use meteorological data together with a model of the radiative transfer function of the atmosphere. To achieve this, however, meteorological information must be collected over the entire image at the same time as the image is acquired. Logistically this is usually impractical, so the values from the nearest weather station are used as parameters within the modelling program instead. From this information a single value for the atmospheric component at each wavelength can be calculated and removed from every pixel of that spectral band. The use of the same correction factor for a given wavelength across the whole image and the lack of representivity of the weather information limit the reliability of this technique.

In the majority of cases, local meteorological information is not available and alternative methods exploiting the image data have to be used. All of these methods make various assumptions about the nature of the target reflectance and provide only a single correction factor for each wavelength.

The simplest procedure assumes that at least one pixel within the image has zero radiance at the sensor in all bands, such as a pixel in a dark area over a deep, clear water body (water approximates to zero reflectance) or an area of dense shadow (no incident radiation to be reflected). In the presence of atmospheric scatter, however, the recorded value of this pixel at each wavelength is not zero, and the measured values are taken to be representative of the atmospheric scatter across the image in each band and are removed from every pixel by subtraction. In the Histogram Minimum Method (Chavez, 1975), the correction value at each wavelength is taken to be the minimum of that wavelength's histogram, obviating the need

to search for the minimum value pixel explicitly. The disadvantages of this procedure are twofold; no account is taken of the spectral signature of the target (e.g. water does have very low reflectance in the infrared but reflects some energy in the visible implying that the minimum pixel value at shorter wavelengths is a combination of both atmospheric scattering and target signal); and a zero radiance pixel may not exist in the image (e.g. a scene taken over a flat desert). Either of these conditions will result in over-correction of the image.

An alternative method, also proposed by Chavez (1975), uses observations from a spectrally homogeneous, but variably illuminated, target area such as a hill composed of a single rock type with shadowed and sunlit sides. When the radiance values of two spectral bands within this area are plotted as a scattergram (Figure 2.4), they lie on a straight line from bright to dark. In the absence of atmospheric path radiance, this line passes through the origin. Assuming that one of the bands has no atmospheric component (usually a SWIR band less affected by the atmosphere) any offset from the origin where the line intercepts the second band's axis gives the correction factor for that band. Linear regression is used to calculate the offset for each spectral band against the same SWIR reference band. As with the HMM, this Regression Method (RM) has practical disadvantages. Firstly, it is often difficult to find an area in an image that is spectrally uniform but has enough illumination variation to give a statistically acceptable straight line fit. Secondly, all correction factors are relative to the reference band in which it is assumed that zero represents zero radiance. If this assumption is incorrect, correction factors calculated in this manner may well be under estimates.

The Covariance Matrix Method (CMM) is a multi-dimensional extension of the RM proposed by Switzer, Kowalik & Lyon (1981). The basic assumptions of the CMM are similar to those of the RM, but instead of using individual pairs of spectral bands, the CMM calculates the covariance between all the bands. Again, the method is relative and requires the path radiance of one band to be known from other information or alternatively to be assumed.

Crippen (1987) introduced the Regression Intersection Method (RIM) to provide absolute correction factors for all spectral bands without having to assume a value in one band, or find a non-illuminated (shadow) or non-reflective (water) pixel in the image. The method involves calculating regression lines for a number of areas of different, but locally uniform, spectral properties. The only point where these lines can intersect is at zero ground radiance since that is the only point at which the radiometric values of spectrally different materials can all be equal. The co-ordinates of this intersection represent the necessary correction factors. Statistical analysis can be performed on the results by choosing a number of different sites and calculating the intersection for pairs of sites.

In the presence of atmospheric path radiance, a band ratio image will retain topographic shading. If corrections are made for the atmosphere, however, the band ratio will appear flat. This provides another mechanism by which correction factors can be determined. Either the spectral bands can be adjusted interactively until the calculated band ratio appears visually flat, or the variance of the ratio can be minimized. In the Minimum Ratio Variance (MRV) method (Wang & Nunez, 1992), an objective function, which depends on the correction factor in each band and is proportional to the variance of the ratio, is minimized. Again, data must be selected from a spectrally uniform, but topographically variable, area. Furthermore, the path radiance for one band must be estimated using, for example, the HMM.

In summary, there exist various methods of estimating atmospheric path radiance using only the recorded image data. All make assumptions or require specific conditions to be met by the image which at times are difficult to achieve. For example, in a semi-arid desert area there may neither be a water body nor enough topographic shadowing to satisfy the dark object assumption. Furthermore, it can be difficult to identify areas which are unequivocally spectrally uniform. The choice of method currently depends on the characteristics of the study area, and research aimed at finding a solution of the general case continues.

Switzer *et al.* (1981) provide comparisons of the values calculated from some of the methods. The CMM and RM give similar results but those from the HMM, either on small local areas or the scene as a whole, are considerably different, suggesting that the data would be over-corrected if this method had to be used. The significance of small errors in the correction factor has not been reported but will be greater in areas of low signal.

### **2.1.2.3 Band ratios**

As described in section 2.1.1.3, the signal received by the sensor comprises a number of different components, the largest of which is shadowing caused by topography. Although shadows help to emphasise structural features, they can confuse the discrimination of rock units. Assuming that the topographic component in Equation 2.2 is independent of wavelength and that the atmospheric path radiance has been corrected, shadowing can be removed by dividing the radiance in one band by that in another. If performed correctly, the resulting ratio image will appear visually flat with no perceivable topographic features.

The computational procedure for band ratioing is one of simple arithmetic. The ratio is formed by dividing the value in one spectral band by the value in another, pixel by pixel across the entire image. In principle, the calculated ratios can range from zero to infinity but in practice the maximum is seldom above five due to the spectral characteristics of typical surface materials. To be displayed the ratio values have to be re-scaled to the range 0 to 255. Ratio images emphasize spectral differences between the selected bands, and so can be used to help locate specific materials. For example, a high ratio between TM5 and TM7 indicates strong absorption in the shortwave infrared which is commonly related to the presence of the hydroxyl ion in clay minerals and may be associated with hydrothermal alteration. Other useful ratios include TM3/TM1, which responds to absorption due to iron minerals, and TM4/TM3, which can be used to map vegetation health or density.

There are some drawbacks to ratio images. Firstly, they can be difficult to relate to a map since topographic shadowing is removed. Secondly, any random noise within the original data is enhanced in the ratios and leads to anomalous values which may affect the re-scaling of the ratio for display or be misinterpreted as geologically significant. This is particularly apparent when brightness in the band used as the denominator drops to low levels. Various schemes have been proposed to limit this effect but in reality they are only cosmetic. Finally, ratio values are only determined by relative, not absolute, brightness values; albedo differences between different surface types are reduced or eliminated. Thus, rocks of quite different albedo can appear similar in a ratio image. For example, a basalt will appear dark in the individual spectral bands and easily distinguishable from a bright marl. However, the ratio value for the basalt and marl may be similar due to the degree of absorption.

Displays which allow very good discrimination of different surface materials can be created by forming colour composites using three separate ratio images. The difficulty is deciding which three ratios to combine. A total of 15 ratios can be formed from the six reflective TM bands, and from these 455 three-ratio composites are possible. Clearly, it is impractical to select the most informative composite by viewing all of the possible combinations. Some methods of statistically ranking the degree of discrimination in each possible ratio combination have been reported (e.g. Chavez, Berlin & Sowers, 1982), but generally ratios are chosen from a knowledge of spectral signatures.

To overcome the loss of the topographic information used to relate the image to a map, a hybrid colour ratio composite can be created in which two ratio images are combined with a single spectral band. Although this appears to negate the reason for calculating ratios, careful selection and balancing of the spectral band can provide an image retaining much of the ratio information and enough topographic detail to provide a geographic reference.

#### **2.1.2.4 Principal components transformation**

Adjacent wavelength bands of multispectral image data are often highly correlated and will therefore appear visually similar. Consequently, using three highly correlated spectral bands to form a FCC will produce a display with little improvement over a single band image since most of the information is duplicated. Principal components (PC) analysis attempts to remove or reduce the correlation between multispectral data, and hence the redundancy in the information.

PC transformation is most conveniently described in a two-band example, depicted in Figure 2.5. If the data in two bands are correlated to any degree they will lie close to a straight line in a scattergram of the two image bands. The amount of variation in any one band can be increased by establishing new axes, along and perpendicular to the correlation line. Note that almost all the variation in both the original bands is now described by the first of these new axes, a new band of data referred to as PC1. The rotation and shift required to position the new axes can be determined from the variance-covariance or correlation matrices (e.g. Davis 1973, Mather, 1976). It is not necessary to correct the data for atmospheric scattering so that the line of correlation passes through the origin of the scattergram, since the new axes are determined by the orientation of the line and not its position. This concept can be extended to n-dimensions, where n is the number of spectral bands, resulting in the computation of n principal components, none of which is correlated with any of the others, containing decreasing amounts of the variability of the original image.

Image analysis can be helped by PC transformation in two ways. Firstly, it can be used as a data compression technique. Instead of having to choose three spectral bands from six, most of the data variation will be contained in the first four principal components thus making it easier to create a useful colour composite. As the first component is mathematically similar to an albedo image, i.e. one containing the major topographic component in the signal, PCs 2, 3, 4 often form an informative FCC image since they express the spectral part of the signal. Secondly, the PC transformation tends to increase the separation between clusters of data making the resulting colour composite highly discriminating.

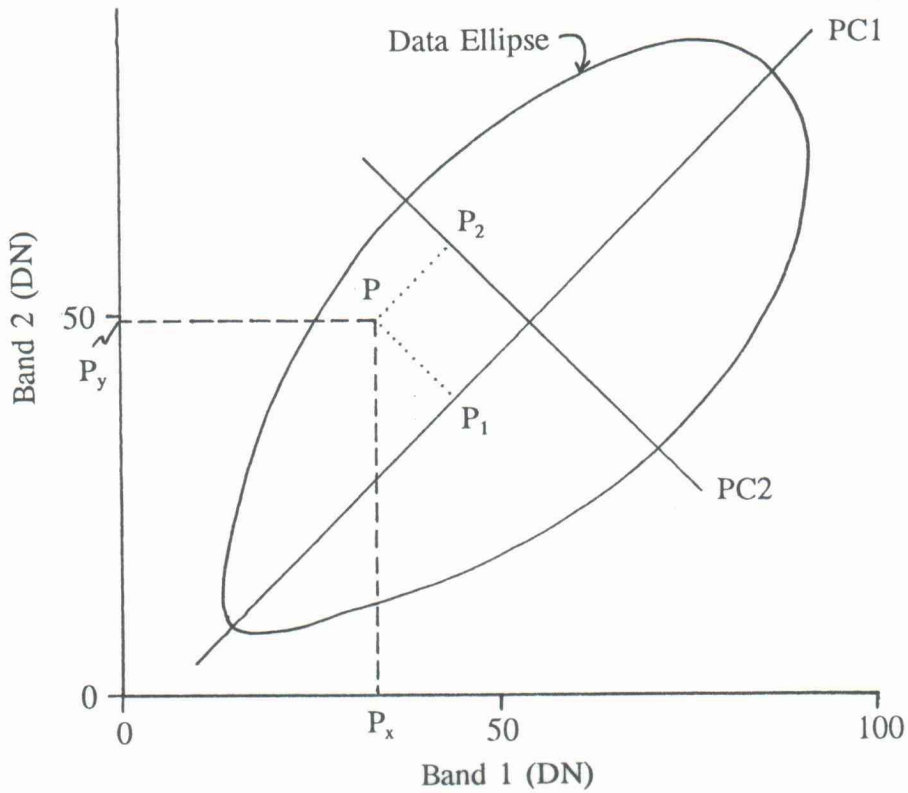


**Figure 2.5** Principal components analysis for the two band case. Point P, which had data values of  $P_x$  and  $P_y$  in bands 1 and 2, has new values of  $P_1$  on PC1 and  $P_2$  on PC2.

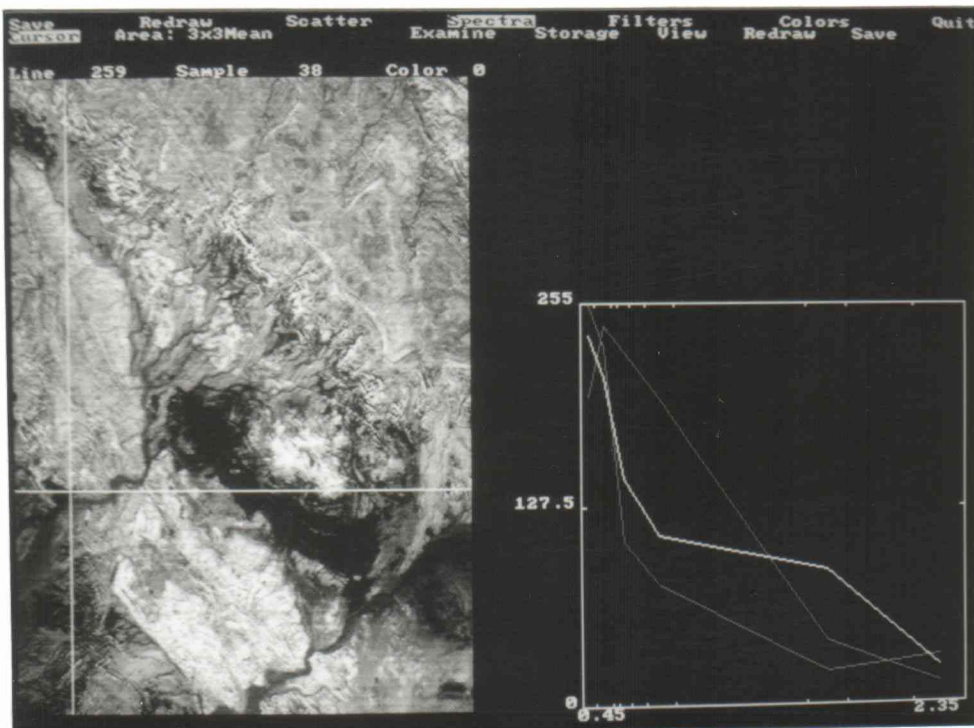


**Figure 2.6** The T-Spectra display with the cursor over a kaolinite mine; the corresponding pseudospectrum is highlighted on the graphic display. Pseudospectra of the Sudr Chalk and the kaolinitic sandstone are shown for comparison in darker tones.

The PC transformation also has disadvantages. Firstly, it can be difficult to relate the different colours to a physical absorption phenomenon since each component is a weighted sum of the input spectral bands. For the lower order components, examination of the weighting factors can suggest which physical material is responsible for variation in that component, but generally this is not the case. Secondly, the PC transformation is scene-dependent since the shift and rotations of the axes for a given image are determined from that image's statistics. The practical consequence of this is that a rock unit represented by a particular colour in a PC 2-3-4 FCC from one scene cannot necessarily be identified by locating the same colour in the same PC 2-3-4 FCC of the another scene, even one immediately adjacent to the first. Indeed, that colour may represent a totally different rock in the second scene.

### 2.1.2.5 Logarithmic residuals

The logarithmic residuals (or log residuals) technique converts radiance data to values approximating reflectance, and was originally designed to be used with high resolution imaging spectrometer data (sensor data comprising numerous, narrow spectral channels). Data of this type have sufficient spectral resolution to be used to remotely identify the composition of the ground surface. Where exposure is good, this allows mineral identification through comparisons with laboratory reflectance spectra of known minerals.

Many other techniques which attempt to convert radiance data to reflectance rely on the remotely sensed data being normalised to ground-based reflectance measurements of known bright and dark target materials. The extensive field work required, ideally at the time of data acquisition, removes a major advantage of remote sensing: reduced reliance on fieldwork in remote places. It also precludes processing of the data before fieldwork begins, removing the advantage of being able to take reflectance-converted imagery into the field. By contrast, the logarithmic residuals technique relies solely on information contained in the data themselves.

The logarithmic residual technique, set out in detail by Green and Craig (1985), is best explained by describing the measurement made at the sensor using an equation. Using the same notation as in Equation 2.2 and assuming that the atmospheric path radiance has been removed as previously described, the measurement at the sensor can be represented as:

$$X_{\lambda} = E_{\lambda} t_{\lambda} A \rho_{\lambda} G_{\lambda} \quad (2.3)$$

Assuming the irradiance of the source ( $E_{\lambda}$ ), the transmittance of the atmosphere ( $t_{\lambda}$ ) and the instrument gain ( $G_{\lambda}$ ) are constant for all pixels in the scene, only the slope and aspect ( $A$ ) and reflectance ( $\rho_{\lambda}$ ) vary for each pixel. For a single pixel  $i$  Equation 2.3 becomes:

$$X_{i\lambda} = E_{\lambda} t_{\lambda} A_i \rho_{i\lambda} G_{\lambda} \quad (2.4)$$

If the remaining multiplicative effects can be removed at each wavelength, the surface reflectance  $\rho_{i\lambda}$ , can be derived from the measured radiance  $X_{i\lambda}$ . For this to be possible, the factors  $E_{\lambda}$ ,  $t_{\lambda}$ ,  $A_i$  and  $G_{\lambda}$  must be found from the data themselves as they are unknowns. The log residuals technique attempts this by the calculation of two geometric means for the scene in question. These are a mean over all wavelengths for each pixel (*spectral mean*) and a

mean over all pixels at each wavelength (*spatial mean*). The spectral mean is calculated in order to remove the slope and aspect effects which vary spatially but are constant for each wavelength of the same pixel. The spatial mean is calculated in order to remove the spatially independent illumination, atmospheric transmittance and instrument gain effects which vary only with wavelength. The spectral mean for pixel  $i$  derived from Equation 2.4 is:

$$X_i = E_t A_i \rho_i G \quad (2.5)$$

where

$\cdot$  = the geometric mean over all wavelengths (other symbols as previously explained).

Division of Equation 2.4 by Equation 2.5 gives:

$$X_{i\lambda}/X_i = (\rho_{i\lambda}/\rho_i)(E_{\lambda}t_{\lambda}G_{\lambda}/E_t G) \quad (2.6)$$

The slope and aspect related factor  $A_i$  is the same in both Equations 2.4 and 2.5 and has been removed by division, resulting in a flat image just as in band ratioing.

Using the same notation for the geometric mean over all pixels, the spatial mean of Equation 2.6 is:

$$X_{\lambda}/X_{\cdot} = (\rho_{\lambda}/\rho_{\cdot})(E_{\lambda}t_{\lambda}G_{\lambda}/E_t G) \quad (2.7)$$

Division of Equation 2.6 by Equation 2.7 gives

$$(X_{i\lambda}/X_i)/(X_{\lambda}/X_{\cdot}) = (\rho_{i\lambda}/\rho_i)/(\rho_{\lambda}/\rho_{\cdot}) = LR_{i\lambda} \quad (2.8)$$

where

$LR_{i\lambda}$  = the logarithmic residual at wavelength  $\lambda$  for pixel  $i$

In this second step, the gain, irradiance of the source and atmospheric transmittance factors are the same in both Equations 2.6 and 2.7 and can thus be removed by division. Only reflectance terms remain. LRs do not represent purely the reflectance of pixels at one wavelength ( $\rho_{i\lambda}$ ), since they retain contributions from mean reflectances for the whole scene at all wavelengths ( $\rho_{\cdot}$ ), sample  $i$  at all wavelengths ( $\rho_i$ ), and wavelength  $\lambda$  for all samples ( $\rho_{\lambda}$ ). If the term ' $\rho_{\cdot}/(\rho_i \rho_{\lambda})$ ' approximates to 1, however, the logarithmic residual value will approximate to the reflectance  $\rho_{i\lambda}$  as desired. The further the mean spectra depart from this ideal, the further will  $LR_{i\lambda}$  deviate from the actual reflectance. If care is taken when collecting statistics for the LR calculation to avoid obvious anomalies such as clouds and to include a full range of scene components, then the residuals will closely approximate to reflectance. For computational ease the geometric means are computed from arithmetic means of logarithms, hence the term logarithmic residuals.

Like PCs, LR data consist of real values; these can be analysed as pixel spectra, with the LR values plotted at the correct wavelength positions. Such LR spectra can be compared to the

spectra of pure minerals measured in the laboratory, and characteristic spectral signatures can be used to identify the dominant minerals in a pixel. For display purposes, selected log residual bands may be combined in a FCC (after scaling to byte values in the normal manner). Since correlated information such as topographic variation has been removed and only reflectance remains, such images commonly allow a similar level of discrimination to PC images.

### **2.1.3 Image interrogation**

Section 2.1.2.5 described the conversion of remotely sensed data to values approximating reflectance using the logarithmic residuals technique. As noted, these converted data provide highly discriminating FCCs and can be interpreted in conventional ways by visual inspection. However, the real advantage of the log residuals data is that they closely approximate to reflectance, a physical property of rocks and minerals which varies in a predictable fashion with wavelength and which can be accurately measured in a laboratory.

Although the log residuals technique was originally designed to be used with hyperspectral data, there is no reason why it cannot be used with broadband satellite data such as Landsat TM. In this case, however, the resulting reflectance curve will be a very crude approximation of a true spectrum, referred to here as a '*pseudospectrum*'. In the case of a TM pseudospectrum, this will consist of values for each of the six reflective bands. As an alternative to simple visual image interpretation, each pixel of an image may be analysed spectrally in terms of the six log residual values by comparing pseudospectra for pixels in the image with known mineral spectra sampled over the same wavelengths. Most conventional image analysis systems do not have the tools to carry out this type of spectral analysis, but specialist software is available. In the present study, a system called T-Spectra was purchased to undertake this analysis.

#### **2.1.3.1 Description of T-Spectra software**

T-Spectra is a spectral analysis software package which runs on IBM-compatible PCs under DOS. It allows any type of satellite or airborne radiance data to be read in and supports most data formats. The user has access to a limited number of standard image processing techniques; the display of a single band as a 16 grey-level black-and-white image; calculation and display of image statistics and scattergrams; contrast stretching; band ratioing; and edge-enhancement. The package can be used to analyse data already converted to reflectance, or to carry out the conversion of radiance data to reflectance values using logarithmic residuals or another similar technique.

Using T-Spectra, it is also possible to read in field or laboratory reflectance spectra, display them, resample them to the resolution of a particular sensor, and perform mathematical operations on them. The real strength of the software, however, is the ability to analyse image data in spectral terms. The user displays a single band image of LR data for reference (usually one in which a key mineral displays strong absorption) and is then able to plot the LR spectrum for any selected pixel location (Figure 2.6). This image spectrum can be compared with spectra from other locations in the image and with library spectra measured in the laboratory or field. Each spectrum can be saved for future reference so that, as analysis proceeds, it is possible to build libraries of image spectra; when a new image is

analysed, its spectra can also be compared to those from previous images, which may even have been acquired by different sensors.

Several spectral libraries were set up within T-Spectra for this project. In addition to libraries containing the spectra measured for all the field samples and for some typical rock samples from around the world (see section 2.2.2.2), two existing spectral libraries in the public domain were used. The first is a library containing the reflectance spectra of 160 common minerals, measured by Grove *et al.* (1992) and hereafter referred to as MINLIB. Subsequent work using these spectra resulted in two further libraries which are fully described in section 2.3.3. The second imported library, VEGLIB, was provided by the NERC Equipment Pool for Field Spectroscopy and contains the reflectance spectra of 26 typical vegetation types. This library was mainly used to assess vegetation cover in the less arid test sites in Namibia. The Appendix lists all spectral libraries in full.

### 2.1.3.2 The application of T-Spectra to TM analysis

Laboratory and aircraft spectrometers enable a full reflectance spectrum to be recorded from which the composition of a sample can be determined. By contrast, the Landsat TM sensor measures the reflectance of the Earth's surface in just 6 broad wavelength bands, from which only crude 6-band pseudospectra can be produced. Despite the limitations of these data, the simultaneous analysis of 6 bands is an advance over the visual interpretation of 3-band composite images. The approach has the potential to allow much better discrimination of minerals and lithologies exposed at the surface. Indeed, with some ground verification and experience gained from the interrogation of previous images, work in this project has shown that it is possible to begin to identify broad mineral groupings from the characteristic shapes of the TM pseudospectra associated with them.

A logical approach to the spectral analysis of TM data is to extrapolate from the known to the unknown within the image under study. In this project, sites of known mineralogy, such as mines, were 'inspected' using T-Spectra to see if they had a consistent pseudospectrum. This was done by displaying the pseudospectrum of a single pixel, or the average of a group of pixels, positioned at the cursor. Once the characteristic pseudospectrum for a location/mineral within the image was identified, it was stored and other locations where known minerals occur analysed in a similar way. This process resulted in characteristic pseudospectra for different minerals/rocks of the image. Having done this, analysis was extended to unknown parts of the image. Areas of interest included regions previously identified as prospective by conventional image interpretation techniques. Pseudospectra typical of these new areas were collected as before and compared with the stored pseudospectra. Where they matched those from one of the known sites, the new area could be provisionally identified.

If the conversion of the TM data to reflectance values is accurate, the image spectra may also be compared to laboratory or field spectra resampled to TM's wavelength bands, so that information relating to the site's mineralogy can be extracted. Even in situations where calibration of the TM data has been less successful, any error in the conversion to reflectance affects all pixels equally; although in this case comparisons to library spectra are difficult, the pseudospectra within one lithology remain internally consistent and the approach based on extrapolation from known to unknown image spectra can still be used. Using either of

these approaches, or both in combination, many parts of an image can be provisionally classified.

Following this approach, subsequent field studies are more focused because they are targeted on the most prospective sites and performed with advance knowledge about the minerals and lithologies expected to be found. As more scenes are analysed and pseudospectra typical of particular lithologies and environments are stored in image spectra libraries, an increasing percentage of each new image will be amenable to analysis using T-Spectra. Ultimately, it may be possible to perform an automatic classification of a new image, either using standard classification techniques applied to the log residuals data or by the application of an expert system.

## **2.2 Laboratory analysis**

### **2.2.1 Introduction**

The spectral analysis of TM data requires a knowledge of the spectral responses of ground materials. This understanding can be gained from studying samples in the laboratory or field using a high resolution spectroradiometer. The several publications of Hunt and co-workers cover in great detail the subject of laboratory spectral measurements for various groups and families of minerals. Building on this, researchers have accumulated comprehensive spectral reference libraries of naturally occurring minerals (e.g. Grove *et al.*, 1992). This information has been used mainly for interpreting high spectral resolution imagery, in particular airborne imaging spectrometry data, but can equally be applied to the study of TM data.

Although this spectral library data is helpful, the response from ground pixels corresponds only approximately with the pure mineral spectra recorded in the laboratory. This is because the ground composition within the area of one pixel (30 m x 30 m for Landsat TM) is a complex mixture of materials including green and dry vegetation, lichen, soil, weathered rocks and minerals, all modified by surface processes which create variations in texture and shadowing. Even where significant amounts of a pure mineral occur it represents only one component among several materials comprising the pixel. Thus, its remote sensing signal is likely to differ significantly from the pure laboratory spectrum. A second problem relates to the reflectance calibration of the remotely sensed data; as described above, the radiance value recorded by the sensor is significantly modified by atmospheric effects and by topographic shadowing. Where these are not entirely corrected for, residual errors occur in the pixel spectra that are not present in the laboratory measurements. In particular, there are a number of atmospheric absorption bands where the remotely sensed signal cannot be utilised at all.

In order to obtain better laboratory correlation, samples of ground materials - many impure but to some extent representative of the actual surface - were collected during fieldwork for subsequent laboratory spectral measurement. Samples representing both the minerals sought and composites approximating to the average surface composition in the area were collected. Despite these efforts, such samples seldom represent the true average ground composition since they ignore the components which vary at a larger scale than the sampling, such as outcrop, vegetation and shadow. However, they are closer to the target response than pure mineral spectra and can be used as a first approximation to evaluate the imagery.

## 2.2.2 Laboratory spectral analysis

For each of the study areas, lithologies were sampled so that the spectral variations seen in the imagery could be investigated. The sampling was biased toward those materials causing TM7 absorption, these being likely to contain the minerals of interest to this study.

### 2.2.2.1 Sample measurement

The aim of the laboratory spectral analysis was to produce absolute reflectance spectra for each sample over the wavelength range of the TM sensor. The samples were measured using a GER Mk IV IRIS spectroradiometer from the Natural Environment Research Council's Equipment Pool for Field Spectroscopy. The use of this instrument is described in Milton and Rollin (1987). The procedure was as follows. Each sample was placed on a measuring tray directly below the IRIS sensor with the sample filling one half of the instrument's field of view. The sample was illuminated using a 1000W Tungsten-Halogen lamp. The IRIS measures the energy reflected from the sample's surface at 965 wavelength positions between 0.4 and 2.5  $\mu\text{m}$ , simultaneously measuring the reflectance of a spectrallon reference plate filling the other half of the field of view. The spectrallon plate's reflectance is accurately known and is close to 100 % across the wavelength range under study. The digital data resulting from each measurement were stored on a PC running software provided with the instrument.

For a given locality the sample taken and spectra measured depend on the nature and mix of the materials present. Where possible, the fresh rock surface, the weathered surface and the typical surface cover or soil were measured so that the fresh rock could be related to its weathering products. In naming the spectra, the following convention was used:

letter/number	=	locality number
f	=	fresh surface
w	=	weathered surface
a, b, s, etc	=	soil

### 2.2.2.2 Data pre-processing, reduction and analysis

Before analysis of the measured data could begin, several pre-processing steps were necessary. The sample and spectrallon plate measurements were each corrected for the instrument's gain and dark current settings; the sample's reflectance measurements were divided by those of the plate to produce reflectance relative to spectrallon; various instrument corrections were applied; and finally, the relative reflectance measurements were converted to absolute reflectance using the known reflectance of the spectrallon plate. Several measurements of each sample were made to ensure a representative result, and averaged.

The resulting spectra can be analysed in a limited way using the software provided with the IRIS instrument. More sophisticated analysis, including the comparison of the measured spectra with existing mineral spectra and image data is best performed using T-Spectra or other similar software. The use of T-Spectra was described in section 2.1.3. For this project, spectral libraries containing the absolute reflectance spectra of the field samples were set up in T-Spectra called EGYPT and NAMIBIA. In addition, a library of typical rock spectra,

ROCKLIB, was created from measurements of rock samples from various BGS collections. The analysis of particular spectra is described in the relevant sections of Chapter 3 (Egypt) and Chapter 4 (Namibia).

### **2.2.3 X-Ray diffraction analysis**

X-ray diffraction (Zussman 1967) is a determinative mineralogical technique carried out on a ground sample of a material usually smeared onto a glass slide from a slurry prepared in acetone. XRD had two main purposes in the present study: first, the identification of the minerals present to validate identifications made through laboratory spectral analyses, and second the semi-quantitative estimation of the proportions of different compounds. Mineral identification is achieved by comparing the positions and relative intensities of atomic diffraction peaks against reference data. It is a well-established and reliable analytical technique except where very small quantities of a mineral are concerned. The estimation of mixtures is more difficult and depends on comparing the relative intensities of diffraction of the constituent materials present. At best it is an approximate method.

XRD analysis of clay minerals involves additional difficulties since clays are less perfectly crystallized, platy, extremely fine grained and have a variable content of inter-layer water molecules. Thus, diffraction peaks are broader, intensities are lower and there are fewer measurable diffractions.

In this study, selected samples from several field areas were measured in various laboratories. Samples from Sinai and El Fayum in Egypt were measured at the BGS; XRD analyses were carried out on crushed and ground portions of 35 samples using a Phillips PW1700 series automatic diffractometer (Prior, 1992). In addition, 5 samples from Sinai and 18 samples from the Cairo-Suez field area were measured in Egypt by colleagues in the Egyptian Geological Survey using the same type of diffractometer (Razek, 1993; El-Saiy *et al.*, 1993). Samples from Namibia were measured in Namibia by Dr G Schneider at the Geological Survey. In each case, the results were reported in the form of a table listing major, minor and trace minerals for each sample. They are discussed in the sections of the report dealing with the relevant field area.

### **2.2.4 Discussion**

The two methods of laboratory analysis differ in several respects. XRD analyses are carried out on powders formed by crushing the field sample in a pestle and mortar and so relate to the bulk mineralogy of the whole rock. In contrast, laboratory spectral measurements are usually made over the surface of the undisturbed field sample and thus reveal the surface mineralogy. Moreover, samples are chosen to provide surface materials as close as possible to those seen by the TM sensor. Consequently, the IRIS reflectance measurements are normally of the weathered surface and are biased toward secondary minerals, whereas XRD analyses are of the primary mineralogy.

Each technique provides useful information. Since the XRD analyses relate to the bulk mineralogy and are semi-quantitative, they are better suited to the assessment of the rocks' industrial utility and economic value. On the other hand, the IRIS analyses are a closer analogy to the TM data, representing a similar type of measurement on the exposed surface;

they provide the link between the remote sensing observations and the actual mineralogy of a sample, without which the significance of the occurrences identified using the TM data could not be evaluated.

## **2.3 Theoretical study of TM's spectral capabilities**

### **2.3.1 Background**

In order to assess the degree to which other minerals might be expected to be differentiated, or identified, using TM data, a theoretical study was undertaken. This involved reducing the high resolution laboratory reflectance spectra for various minerals to TM's 6 wavebands and assessing which minerals retained distinctive or distinguishable spectra. The data were also resampled to the resolution of a newer satellite sensor, the Japanese Earth Resource Satellite 1 (JERS-1). This sensor has 8 bands comprising equivalents of TM2, TM3, TM4 (2 bands to give stereo), TM5, and 3 bands covering the wavelength range of Landsat's single band TM7. Resampling therefore results in 7 band pseudospectra (omitting the stereo band) which offer the potential for increased discrimination amongst clay, sulphate and carbonate minerals mainly due to the increased resolution in the SWIR wavelength region.

### **2.3.2 Resampling software**

The T-Spectra software can be used to resample laboratory or field reflectance spectra to the resolution of another sensor, but the calculation is not performed rigorously; the software merely takes the full-resolution reflectance value at the central position of each TM band, resulting in a 6 band pseudospectrum. The rigorous procedure is more complicated, and involves multiplying the values from the full-resolution spectrum by the sensor's detector response function across the wavelength range of each TM band, resulting in a single value for that band. The six values calculated in this way are equivalent to those the TM sensor *would* measure on the sample if used in the laboratory. This is important for broad bands such as TM7, which covers a wavelength region containing several mineral absorption features at different wavelength positions; merely taking the value at the centre wavelength of TM7 (as T-Spectra does) is clearly inadequate. This effect is seen in Figure 2.7, which depicts laboratory reflectance spectra for two minerals and their equivalent pseudospectra created using the simplistic and the rigorous approaches to resampling.

To achieve the correct resampling procedure, new software called SPECTCNV was written in the Turbo C computer language to run on a PC. The executable version is simple to implement, runs under DOS on any IBM-compatible PC, and produces pseudospectra which can be viewed using T-Spectra without modification. Individual spectra are converted using the routine JUSTDOIT, while groups of spectra contained in a list file can be converted using a batch routine, DOITALL. Spectra measured using the two most common laboratory spectrometers, the GER Mk IV IRIS (used in this project) and the Beckman (widely used in the USA), can be converted to reduced resolution spectra for any sensor for which the response functions of the bands are held. In this study this information was provided for both Landsat TM and JERS-1 by the NERC Equipment Pool for Field Spectroscopy.

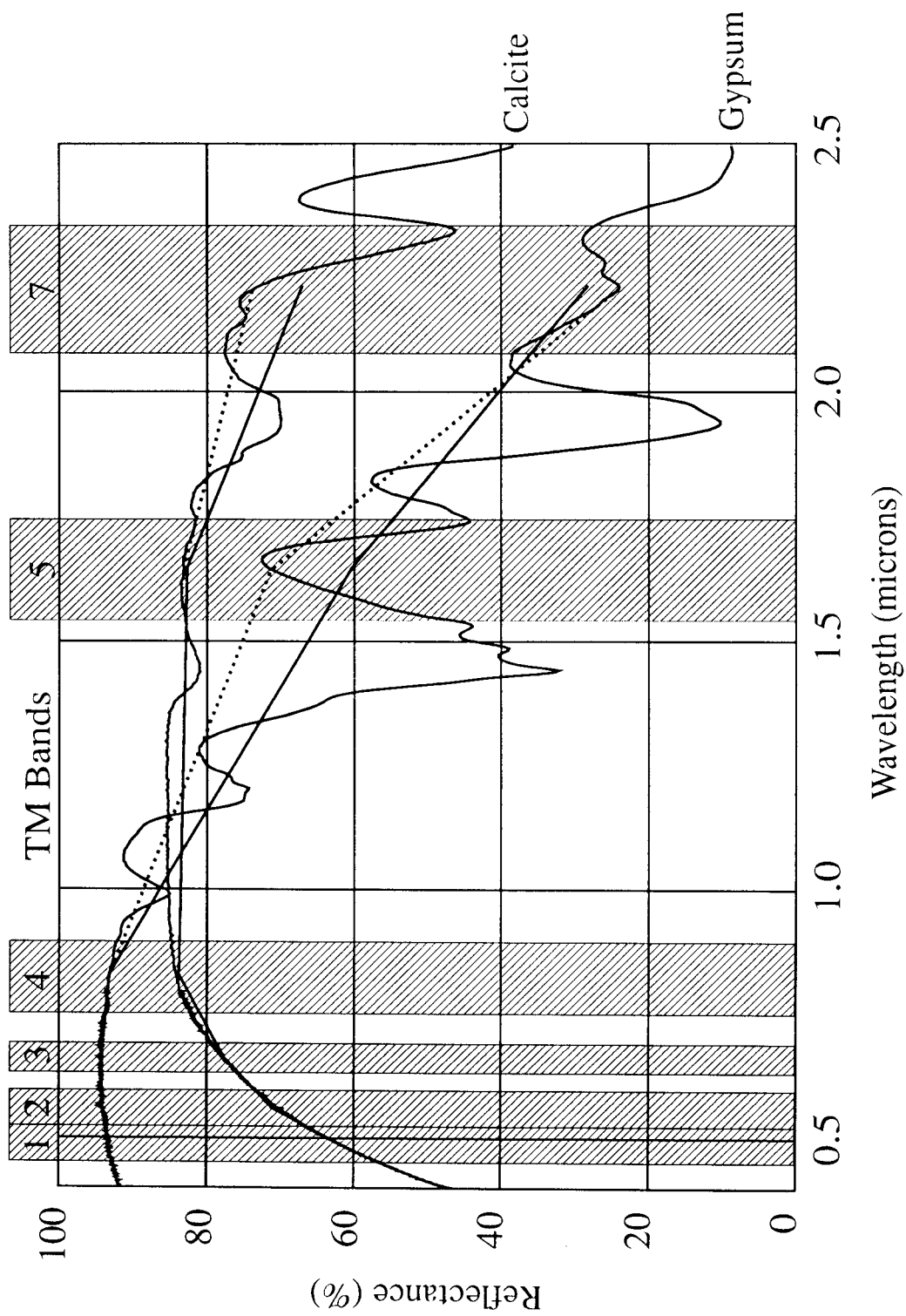


**Figure 2.7** Reflectance spectra for calcite and gypsum. The solid lines show their laboratory spectra at full resolution and resampled to TM's wavebands using the rigorous approach. The dotted lines show the effect of merely taking the central wavelength value in each band.

### 2.3.3 The spectra studied

In assessing the spectral capabilities of Landsat TM, it is necessary to rationalise the list of possible minerals for consideration. Even the inclusion of all 160 minerals for which reflectance spectra are available in ROCKLIB presents an enormous task. For practical reasons it was decided to restrict the study mainly to minerals of industrial significance and to sedimentary rocks associated with them. Although all the minerals in ROCKLIB were resampled to the resolutions of both TM (stored in TMLIB) and JERS-1 (stored in JERSLIB), only the following minerals were selected for the study:

Oxides:	corundum, hematite, magnetite, rutile
Hydroxides:	brucite, gibbsite, goethite
Sulphates:	anhydrite, barite, gypsum
Clay minerals:	illite, kaolinite, montmorillonite
Carbonates:	calcite, dolomite, siderite, trona
Other non-silicates:	apatite, halite, graphite
Micas:	biotite, muscovite
Other silicates:	quartz (crystal), quartz (sand), quartz (chert), albite, orthoclase

### 2.3.4 Results

Resampled TM pseudospectra for the above minerals are shown in Figure 2.8. It is immediately apparent that the majority of the detailed spectral information contained in the laboratory reflectance data has been lost and only simple curves remain. Despite this, many of these curves have distinctive shapes which suggest that some minerals may still be identifiable (e.g. siderite, brucite). Further study of the pseudospectra indicates that they can be placed in six groups each having a similar general form. These are: (1) flat pseudospectra, (2) pseudospectra with a general TM1 absorption; (3) more complex pseudospectra with TM1 absorption; (4) pseudospectra with a general TM7 absorption; (5) pseudospectra with both TM1 and TM7 absorption; and (6) complex spectra different from those of groups 1-5. These groups are shown in Figure 2.9.

Although mineral identification with data at the resolution of TM in this geological environment is rarely possible, the curve shapes allow the range of possible minerals for a given pseudospectrum to be greatly reduced. For example, a flat bright spectrum is likely to be either barite, halite, crystalline quartz or orthoclase feldspar. Similarly, a flat dark spectrum is likely to be magnetite or graphite. Figure 2.9 shows that it should be possible to discriminate between several minerals which cause TM7 absorption using pseudospectra. Gypsum has a quite different curve shape to kaolinite and calcite, while brucite has a distinctive peak in TM3. Further discrimination may be possible based on the depth of the TM7 absorption; the curve for kaolinite is steeper from TM5 to TM7 than that of calcite. Similar distinctions can be made for minerals causing absorption in the visible and near infrared wavelengths. For example, the Fe-bearing minerals hematite, goethite, siderite and biotite all show similar absorption in the visible wavelengths but the detail of their curve shape in TM1-4 allows them to be separated from each other.

Figure 2.10 shows JERS resolution pseudospectra for the minerals hematite, goethite, calcite, kaolinite and montmorillonite. The reduced resolution in the visible, with no JERS-1 band

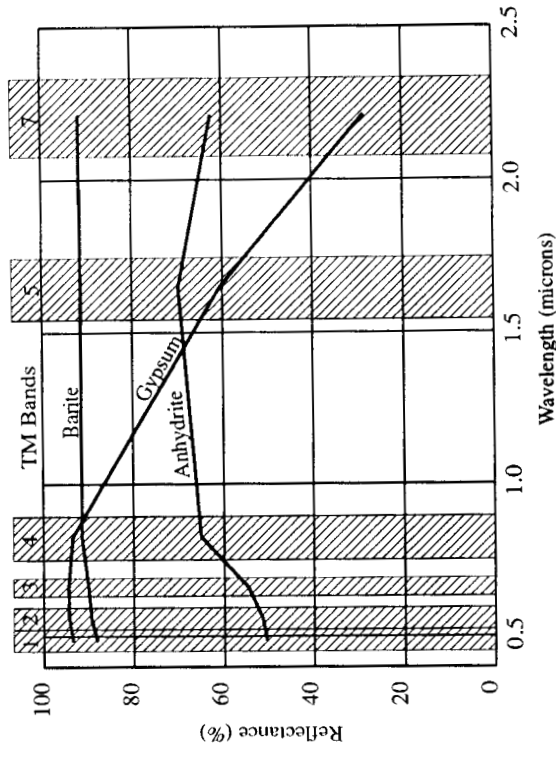
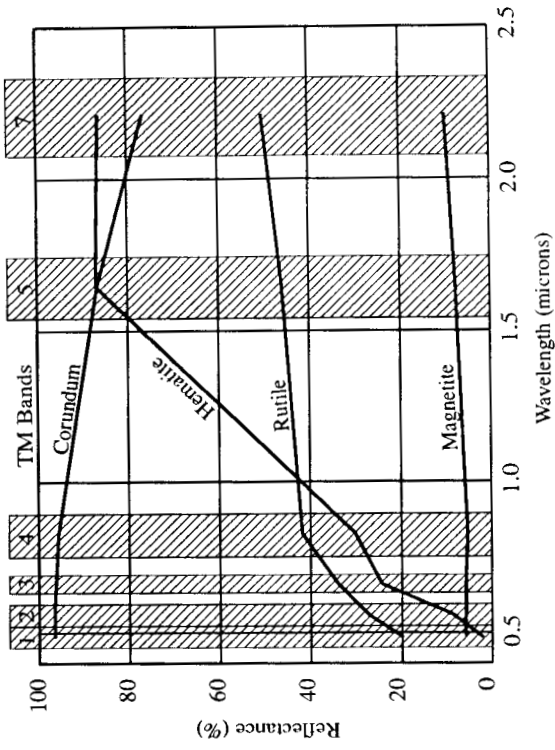
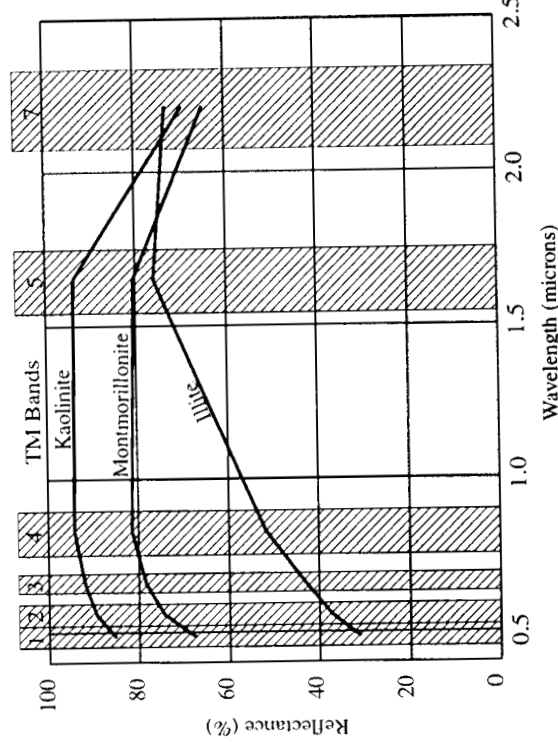
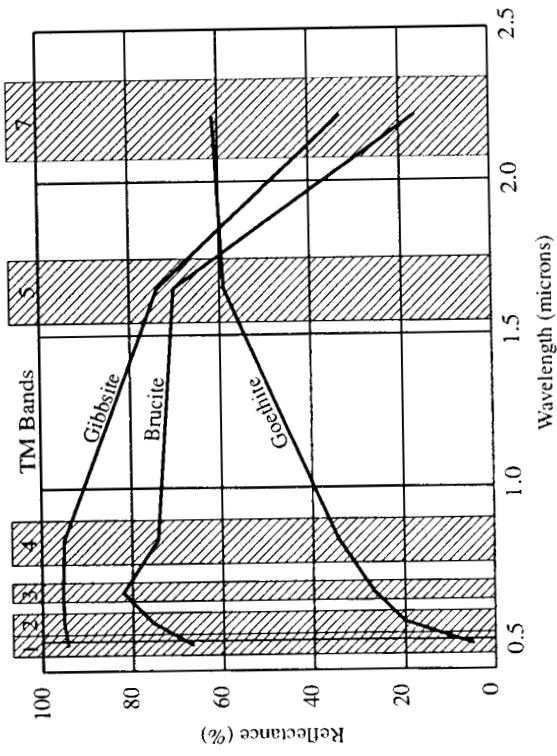


Figure 2.8 Laboratory reflectance spectra resampled to TM's resolution for oxides, hydroxides, sulphates and clay minerals.

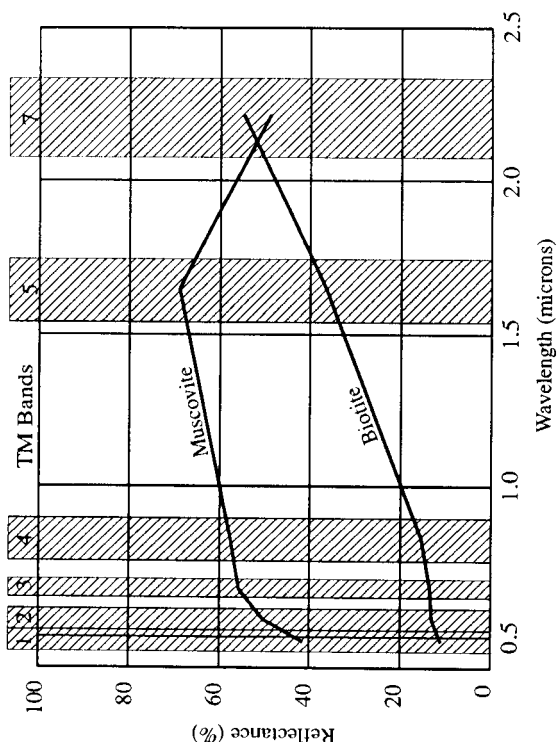
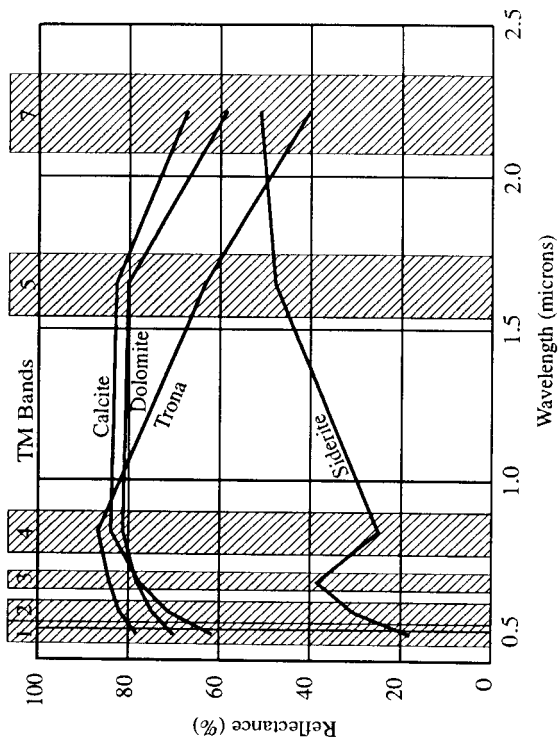
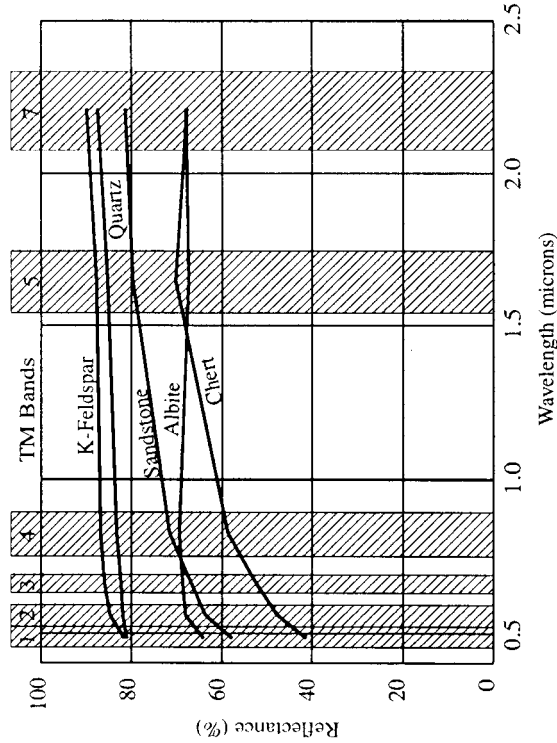
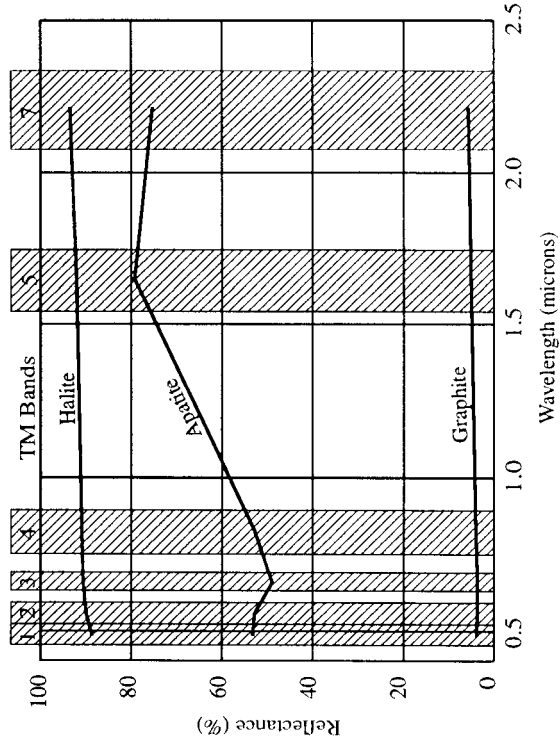
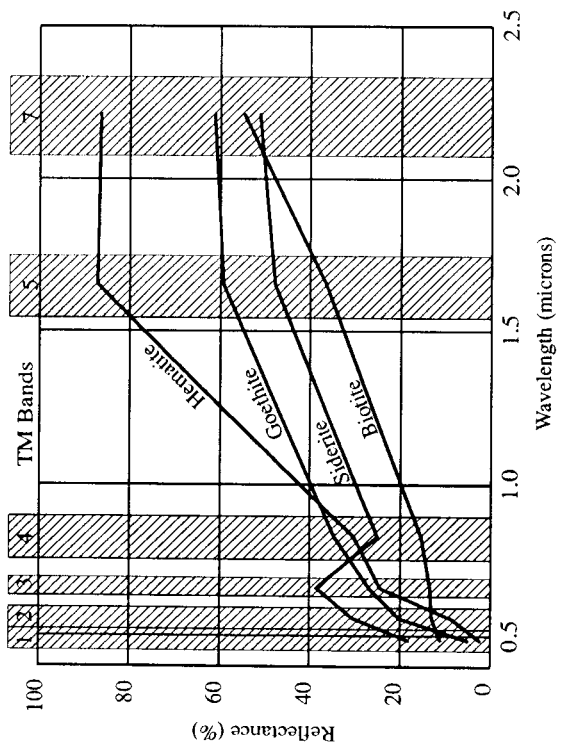
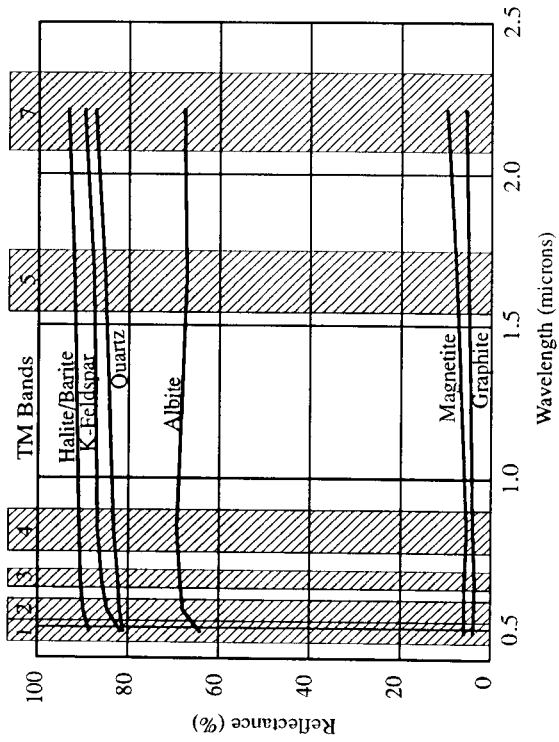
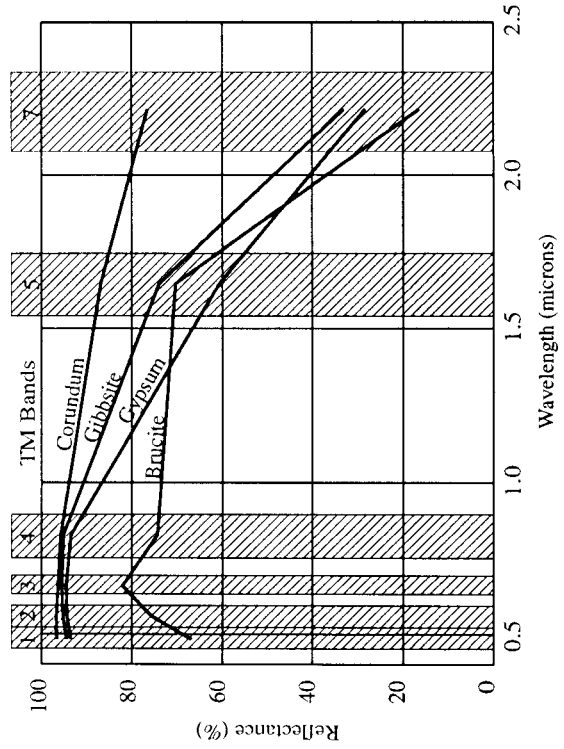
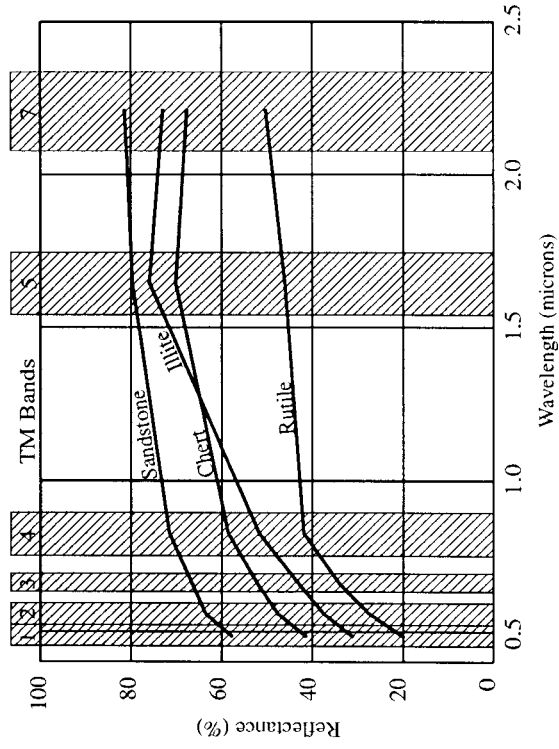


Figure 2.8 Laboratory reflectance spectra resampled to TM's resolution for carbonates, various non-silicates, micas and various silicates.



**Figure 2.9** Laboratory reflectance spectra for various minerals grouped according to shape.

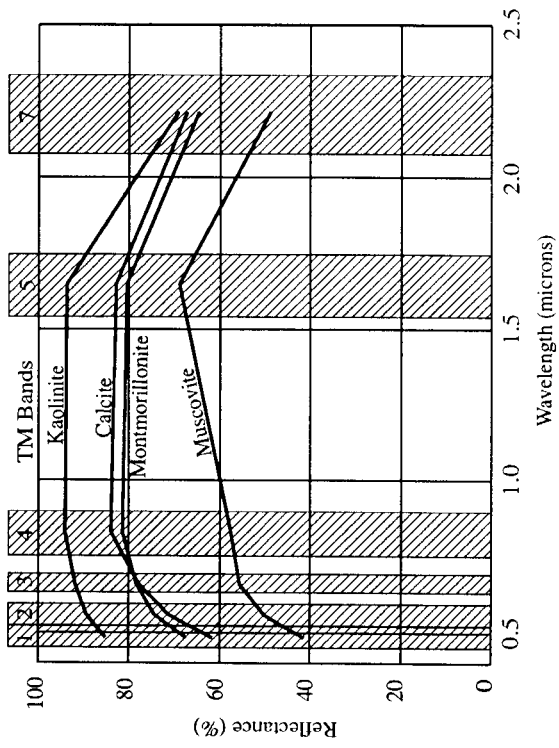
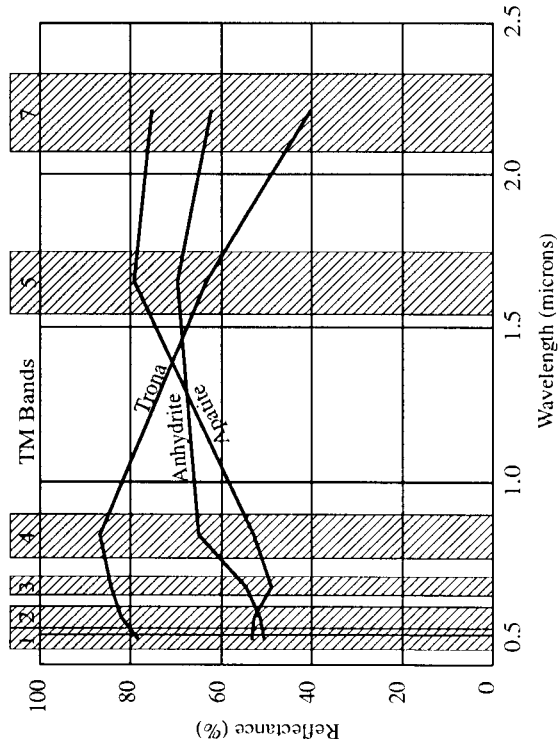


Figure 2.9 Laboratory reflectance spectra for various minerals grouped according to shape.

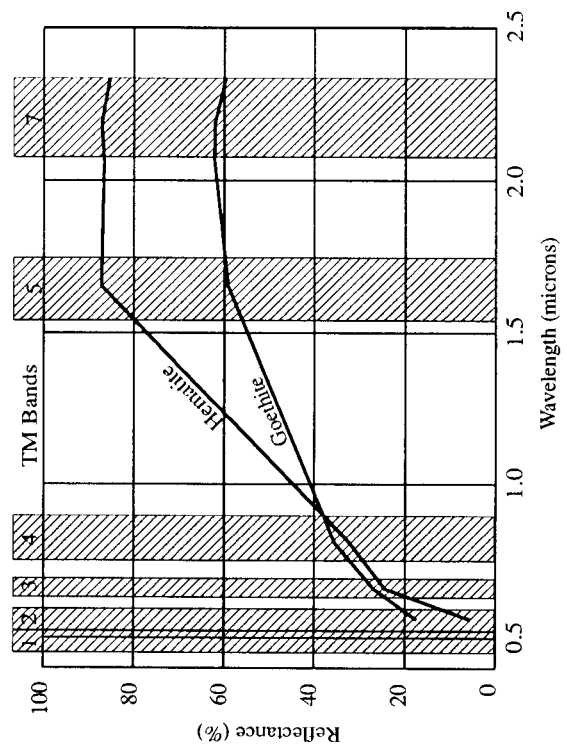
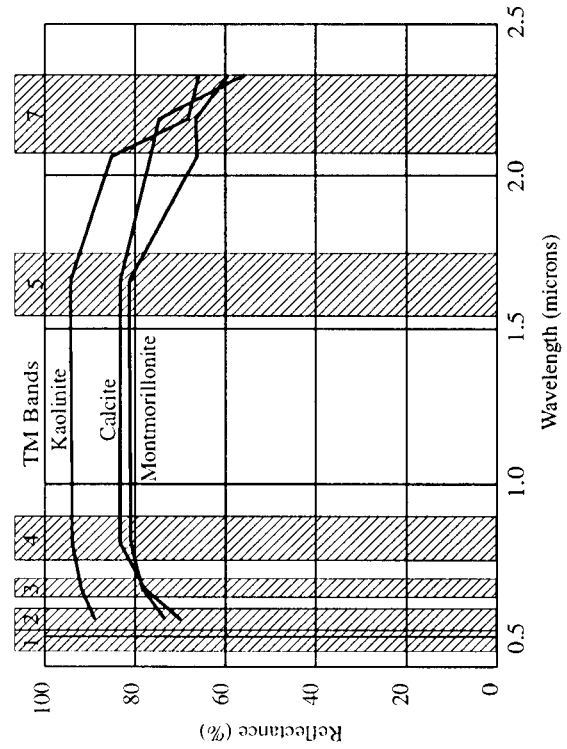


Figure 2.10 JERS-resolution laboratory reflectance spectra for various minerals.

equivalent to TM1, makes it more difficult to separate hematite and goethite. Conversely, the improved resolution in the SWIR has a dramatic impact on the ability to separate those minerals causing TM7 absorption; montmorillonite has a stronger absorption in JERS band 6, kaolinite shows a distinctive feature in JERS band 7 and the main absorption of calcite is in JERS band 8. These three minerals are difficult to separate at the spectral resolution of the TM, as seen in Figure 2.9.

### **2.3.5 Discussion: practical implications**

The theoretical study has demonstrated the extent to which mineral discrimination/identification might be expected using TM or JERS data in a sedimentary geological environment. However in practice, there are other factors to consider. For example, the study considered the spectra of pure minerals, whereas at the 30 m spatial resolution of TM data, few pixels comprise a single pure mineral. Most will be complex mixtures of soil and rock, and will consist of several minerals producing a mixed spectral response. Moreover, the study assumes there is complete exposure of rocks and residual soils, but in practice, as the aridity of an area decreases so the vegetation increases, adding its own spectral response to the combined reflectance signal. Unmixing algorithms aimed at identifying the constituent minerals in each pixel are being developed for both high spectral resolution data (e.g. Ben-Dor *et al.*, 1994) and TM data (e.g. Bierwith, 1990), but they are beyond the scope of the present study. At higher vegetation densities, unmixing becomes more difficult as the mineralogical component of the signal becomes weaker and weaker.

The JERS sensor, although clearly providing better discrimination between clay, carbonate and sulphate minerals, has encountered several problems since the launch. Firstly, the important SWIR wavelength region displays varying amounts of noise, and complex procedures must be used to clean the data before processing can begin, thus making it difficult to use compared to TM. Nevertheless, the data can be cleaned and useful results achieved (Denniss *et al.*, 1993). The second problem is that the sensor was only fully operational for the first 18 months of its life, after which the SWIR sensors stopped operating. Images of many parts of the world were collected during this initial period and can be purchased at minimal cost, but only the launch of JERS-2 will make the regular use of this data a practical proposition.

### 3. ARID TEST SITE: EGYPT

***Synopsis:** This chapter gives a full and detailed account of work carried out in arid sites in Egypt. It provides descriptions of: the geology and industrial minerals of the study areas, image processing techniques, data interpretation, spectral analysis approaches, laboratory studies, and field correlation. Examples of the processed imagery are provided, with explanations. The information is technical and will be mainly of interest to remote sensing geologists and image analysts wishing to understand fully the advantages and limitations of the methods, and to implement the techniques for themselves. Other readers may find interest in the general descriptions of the geology, examples of the data, and sections summarising the main conclusions.*

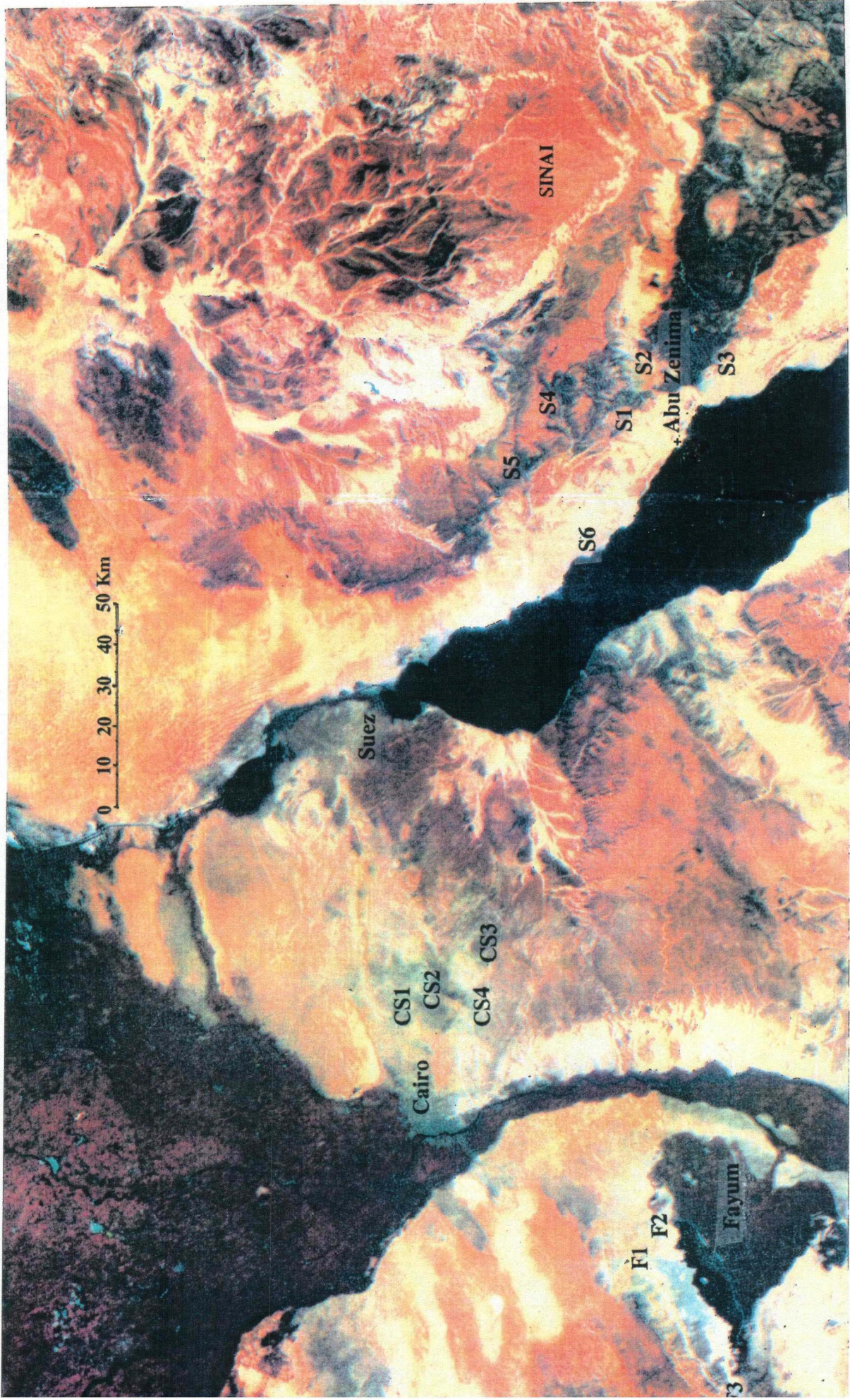
#### 3.1 Introduction

The arid test site of north east Egypt lies between 29° and 30° North and 30° to 33° 30' East. The region is characterised by a warm and almost rainless climate with air temperature rising to 40° in summer and falling to below 10° in winter. Parts of northern Egypt, especially the Mediterranean littoral zone and the high relief areas of western Sinai, have a slightly higher rainfall than the 10 mm/year national average, but still only receive about 20 mm/year. The greater part of the area outside the Nile Valley is thus barren desert.

From a geomorphological perspective, the River Nile divides the region into two distinctive sectors (Figure 3.1). The area to the east of Cairo is a broad dissected plateau, whereas that to the west consists of a series of unconnected depressions flanked by ridges and mesa-plateaux of moderate relief. East of the Gulf of Suez, the Sinai area is a rugged hilly to mountainous terrain ranging from 1600 m on Gebel El Tih to 400 m in the coastal hill range. The strong relief is the consequence of a complex geological history of extensional and epeirogenic activity dating from the Mesozoic to the Tertiary.

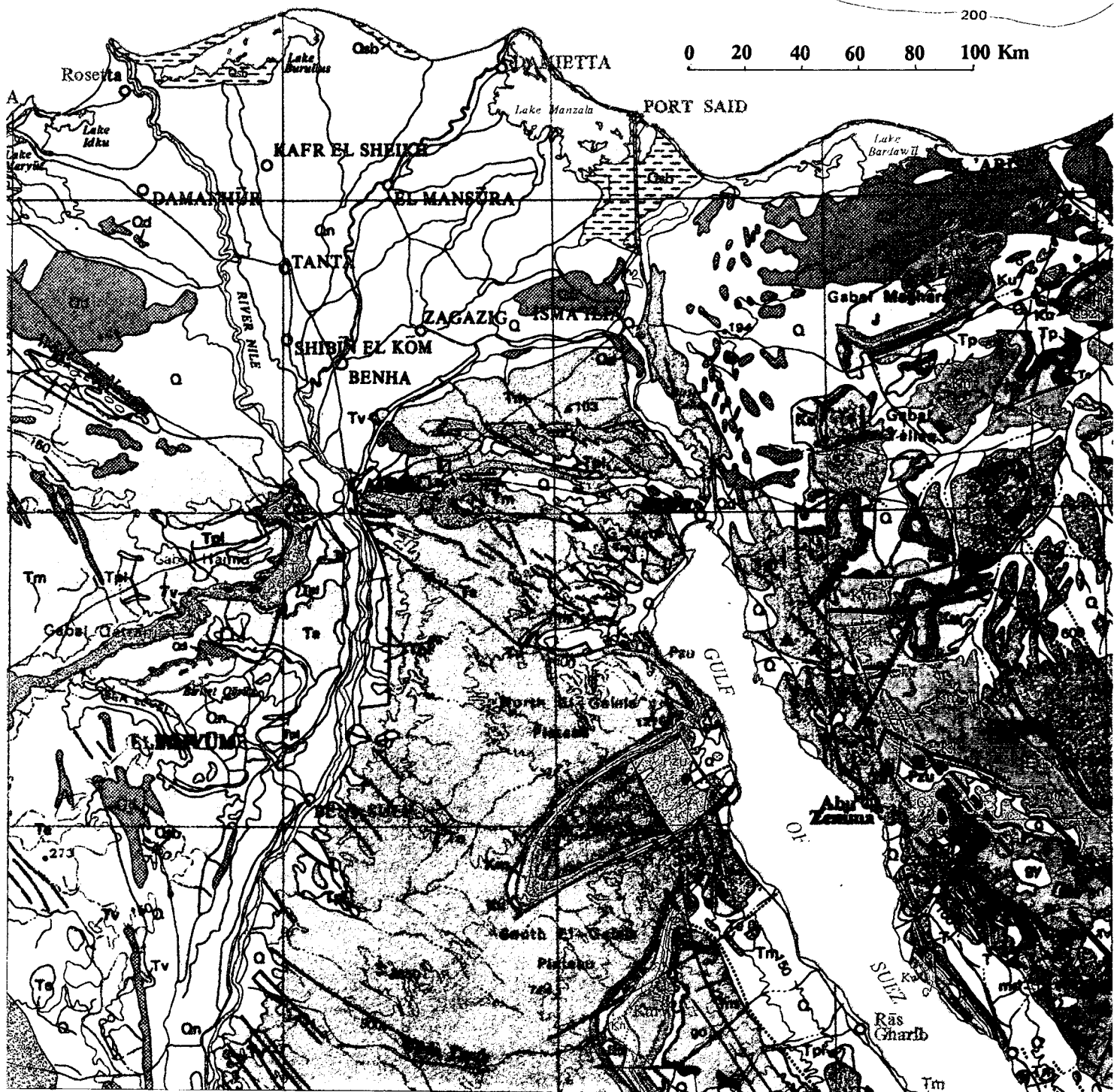
The Egypt study was conducted at three separate sites: Sinai, El Fayum and Cairo-Suez. Their locations are shown on the regional geological map (Figure 3.2). The geology of **western Sinai** is more diverse than the other two sub-areas and spans the Proterozoic-Mesozoic-Tertiary eras. The basement rocks in south Sinai host small base metal deposits while the Palaeozoic sediments are worked for manganese, chrome and titanium sands. The Mesozoic and Tertiary sedimentary sequences are best known for their hydrocarbon reserves, although clays and gypsum deposits are exploited locally on a more modest scale. The **Cairo-Suez** plateau, comprising Upper Cretaceous and Tertiary marls, clays, limestones and local volcanics, is the single most important district in Egypt for the extraction of industrial minerals such as clays, aggregates, limestone and crushed dolerite. The Tertiary marls and clays of the foothills of the **El Fayum** escarpment are a potentially important site for clay mineral extraction, but this activity is not yet fully developed.

The field programme was supported throughout by EGSMa who provided vehicles and drivers, and whose geologists collaborated in the work.



Location of study sites in north Egypt. Sinai: S1 Insaker, S2 Tih, S3 Baba, S4 Gharandal, S5 Wardan, S6 Mreir. Cairo - Suez: CS1 Brick clay and Dolerite quarry works, Cairo-Suez road, CS2 Aggregate quarries, CS3 Clay and marl beds, Qattamia highway, CS4 Limestone quarries, Qattamia highway. Fayum: F1 Qasr El Sagha Formation, clays and marls, F2 clay pits near Kom Oshim village, F3 clays and marls of the Birqet Qarun Formation.

Figure 3.1 Geomorphological map of north Egypt (based on Landsat MSS image provided by EGSMA, Cairo).



Q = Quaternary wadi deposits, Qn = Nile Valley and Delta silts, Qd = sand dunes, Tpl = Pliocene gravels, Tm = Miocene clastics, gypsum, limestone, clays, marls, To = Oligocene, basalt, dolerite sills and dykes, sands, gravels, clay beds (Gebel Ahmar and Anqabia Formations), sandstone, clay/marl interbeds (Gebel Qatrani Formation), Te = Eocene; sandy and white limestones, marls, clays (Maadi and Giushi Formations), clays and marly limestones, sandstone beds (Qasr El Sagha Formation), sandy limestone and clay beds (Birquet Qarun Formation), yellow white limestone (Wadi Rayan and Mokattam Formations, El Tih Limestone formation), Tp = Paleocene (Sudr Chalk Formation), K = Cretaceous, sandstone, clay and marly carbonate, J = Jurassic sandstone and limestone, Pzu = Upper Paleozoic clastics, C = Carboniferous, sandstone, clay, marl and dolomite, gy, go = Late Precambrian granites with enclaves of gneiss (gn) and schist (ms).

**Figure 3.2** Geological map of north Egypt showing occurrences of industrial minerals in the three study sites. Kaolinite beds (■), gypsum (▲), brick clays (□), aggregate (○). Based on Geological Map of Egypt, scale 1: 2,000,000. EGSM, Cairo.

## 3.2 Sinai

### 3.2.1 Geology and setting

The western margin of the Sinai Peninsula is dominated by the high plateau of El Tih built from almost horizontal strata of Tertiary and Cretaceous ages (Figure 3.2). The plateau escarpment is bounded by major faults to the south west in the Abu Zenima area. These faults have dissected the area into several steeply-inclined en échelon cuesta blocks which display lithological detail; these are drained by numerous deep wadis which locally expose the Precambrian basement rocks. The less-faulted western sector is made up of broad low mesa-type tablelands underlain by Tertiary strata. The natural association of tilted fault blocks and dissected mesa plateaux, and the lack of vegetation, render this an ideal sub-area for geological remote sensing.

The geology of western Sinai is summarised below.

TERTIARY	Pliocene	Scree deposits
	Miocene	Clastics, gypsum, carbonate
	Oligocene	Basalt, dolerite dykes and sills, clastics
	Eocene	El Tih limestone Formation
	Palaeocene	Sudr Chalk Formation
	Unconformity	
CRETACEOUS	Upper	Carbonate, marls
	Upper	Nubia sandstone
	Middle	Clastics
	Lower	Clastics with minor clay bands
JURASSIC -CRETACEOUS		Argillaceous sandstones with minor limestones
CARBONIFEROUS		Um Bogma Formation: clastics with clays, marls and dolomites
CAMBRIAN -CARBONIFEROUS		Undifferentiated clastics
LATE PRECAMBRIAN		Arabian-Nubian Shield: granite with gneiss/schist xenoliths

The west central region of Sinai was selected as the primary study area based on mineral occurrence information given in the EGSMA Clay Package (Qusa, 1986) and the non-metallic mineral location map of Egypt (EGSMA, 1980a). The study area is centred on the coastal town of Abu Zenima, contains small-scale industrial mineral mines (manganese, clays), and is the focal point for all access roads servicing the mining and small settlements to the east.

### 3.2.2 Image processing

The west central Sinai region is covered by a cloud-free Landsat TM scene path 175 row 040 acquired 27/7/90. A 1-5-7 FCC was used to assist field location (Figure 3.3A). Other imagery products were subsequently used to help define smaller target areas within the broader region of interest and to maximise local discrimination of various minerals within these areas. As shown in Figure 3.3, these were:

- i) Band ratios (Figure 3.3B) - particularly the ratio of bands TM5 (1.65  $\mu\text{m}$ ) and TM7 (2.22  $\mu\text{m}$ ) which was used to highlight OH-bearing minerals.
- ii) Principal components FCCs (Figure 3.3C).
- iii) Decorrelation stretch FCCs - an extension of the PC method intended to relate the PC data back to the original wavelength bands of the input data.
- iv) Log residuals (Figure 3.3D) - performed following an atmospheric correction using the Gulf of Suez as a dark object, and inverted to display absorptions.

### 3.2.3 Evaluation and field correlation

Sub-areas containing possible industrial mineral occurrences were selected for further processing through examination of a triple-ratio FCC image; they are shown in Figure 3.1 (Marsh and O'Connor, 1992). The principle sub-areas, each measuring 14.6 km x 14.6 km, were:

1. **Insaker:** named after Wadi Abu Insaker. This area contains known kaolin deposits which are being exploited. The area also encompasses a major anomaly in the TM5/TM7 ratio image which is not explained by the existing geological maps.
2. **Tih:** covering the edge of the El Tih Plateau where it meets Wadi El Homur. This area contains an extension of the kaolin deposits mined in Insaker, but they are not exploited at this locality.
3. **Baba:** named after Wadi Baba. This area also contains known deposits of kaolin (both under exploitation and undeveloped), glass sand quarries and a manganese mine.
4. **Gharandal:** named after Wadi Gharandal. This area has no known deposits but contains a gypsum/shale/clastic sequence with diagnostic spectral/lithological features thought to be associated with economic deposits of clay and carbonate rocks.
5. **Wardan:** covering the upper, eastern end of Wadi Wardan and containing a similar sequence to Gharandal.
6. **Mreir:** covering Gebel el Mreir at the western end of Wadi Wardan where significant gypsum deposits are thought to occur.

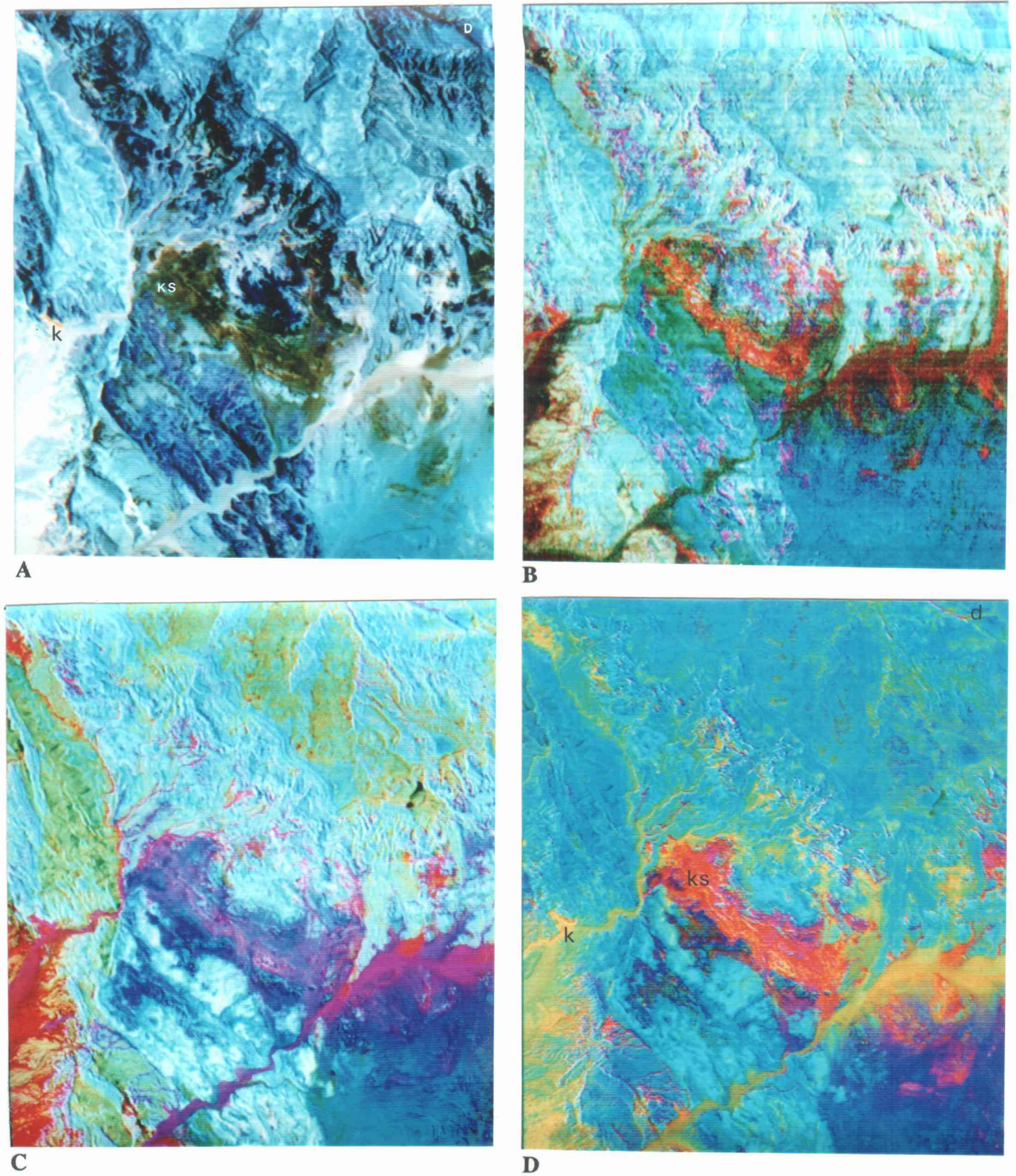


**Figure 3.3** Landsat TM images, Insaker sub-area, Sinai.

- (A) Colour composite, bands 1 5 7 (R G B)
  - (B) Colour ratio composite, bands 5/7, 5/4, 5/1 (R G B)
  - (C) Principal Components 3 2 1 (R G B),
  - (D) Log residuals bands 7 4 1, inverted (R G B)
- Kaolinite (k), kaolinitic sandstone (ks), dolerite dyke (d)

Figure 3.3 shows the TM imagery over the Insaker target area processed in four different ways. (a) A colour composite from three of the original bands. This is shown for comparison with the more complex data products. (b) A ratio FCC image. Here, the mineralogical information content of the TM data is considerably enhanced and the topography/albedo information suppressed. The 5/7 ratio is depicted in red; bright red areas correspond to strong TM7 absorption due to the presence of OH-, CO- or SO-bearing minerals. (c) FCC image based on three PC bands. This image is also highly discriminating but it is difficult to attach physical meaning to the data as each component represents a complex statistical combination of the radiance data at all wavelengths. Although the weightings of each radiance band on each new component can be determined, the PC data cannot easily be used to identify minerals. (d) Mineral identification is better addressed using the log residual data, either in the form of a colour composite image as seen here or by spectral analysis as described in section 3.2.4.

All six sub-areas were processed using the above techniques. Hard copy photographic prints of the data were produced and analyzed, including a FCC for the whole area and the more specialised data sets for the sub-areas.

Investigations focused on three main sub-areas: Insaker, Tih and Baba. Work was also done at the lower priority areas of Gharandal, Wardan and Mreir. Fieldwork consisted of traverses aimed at relating the satellite responses to the minerals of interest. Hard copy TM imagery at a scale of 1:66 000, and aerial photographs at 1:40 000 were used for field location. A comprehensive suite of samples, including fresh rock, weathered outcrop, and loose surficial sand and gravel, was collected in order to investigate the relationship between the solid geology and the surface materials sensed by the satellite.

### 3.2.3.1 Brick clays

Impure clay deposits of Tertiary age, suitable for building materials, are exposed in the region along the Abu Zenima coastal strip. However, the distance to the main market for bricks (Cairo) is probably too great for these deposits to be economically viable. Consequently, this area was not assessed in detail. Other sites closer to Cairo provide much better prospects for economic deposits of brick clays (section 3.4).

### 3.2.3.2 Kaolinite

Kaolinite is being actively extracted by two companies: the Sinai Manganese Company and the Egypt Refractory Company. Initial fieldwork revealed that areas with deep TM7 absorption frequently correlated with kaolinite mine sites. As shown in Figure 3.4, large amounts of high grade kaolinite are often exposed in tips. The kaolinite spectrum, with absorption at  $2.22 \mu\text{m}$ , is shown in Figure 2.2. In the log residuals colour composite for the Insaker sub-area shown in Figure 3.3D, areas of  $2.22 \mu\text{m}$  absorption appear in red. Several mine sites occur in the Insaker sub-area and one of these is labelled *k*. The correspondence of mine sites with areas of TM7 absorption confirms that TM data can be used to locate surface exposures of this mineral. However, to be of practical use in exploration, this success must be repeated for sites not disturbed by mining.



**Figure 3.4** Kaolinite mine (a) and mine tips (b), Wadi Insaker sub-area.



**Figure 3.5** Kaolinitic sandstone outcrop (foreground), Wadi el Homur. Tih sub-area.



**Figure 3.6** Log residuals, bands 7 4 1, inverted (RGB), Wadi Baba (uk) unexploited kaolinite, (d) dolerite dykes, (gy) gypsum.

Subsequent fieldwork concentrated on a large area of TM7 absorption within the Insaker sub-area which could not be explained on the basis of the existing geological maps. TM analysis showed that this anomaly, labelled *ks* in Figure 3.3D, corresponded to an area of ground approximately 5 km x 1 km which in the field proved to be of quite different geological character to the mine sites. Here, the 2.22  $\mu\text{m}$  absorption was due not to a pure kaolinite band but to kaolinite occurring as a minor constituent in the matrix of a quartz sandstone. The kaolinite coats the quartz grains and is concentrated during weathering, forming a disproportionately high percentage of the surface sensed by the satellite.

This finding was important in refining the approach towards the search for economic kaolinite deposits and emphasized the importance of understanding the geological occurrence of the minerals sought. The economic mine deposits form 2-3 m beds within thicker sandstone sequences in the Carboniferous and Lower Cretaceous outcrop (Figure 3.4). The kaolinite is easily eroded compared to the sandstone, so that pure kaolinite bands have a minimal surface exposure. The strong anomaly recorded over the kaolinitic sandstone occurred because kaolinite is concentrated at the surface of the widely-exposed sandstone during weathering (Figure 3.5). Extensive TM7 anomalies such as this one are unlikely to indicate pure kaolinite deposits in this geological environment<sup>1</sup>. Kaolinite beds undisturbed by mining are likely to form smaller, more subtle, TM7 anomalies.

The Baba sub-area contains a number of subtle linear areas of TM7 absorption measuring only one or two pixels wide on the image and extending for up to 1 km. These features, labelled *uk* in the log residual data over the south of the Baba area shown in Figure 3.6, formed further exploration targets. Figure 3.7 shows the field expression of one of these features. The anomalies are caused by undisturbed beds of kaolinite up to 3 m thick. Although the bands themselves are too narrow to be detected by the TM sensor, debris weathered from them extends over a wider area. The resulting anomalies, whilst often no more than one pixel wide on the image, are detectable because they provide a strong spectral contrast with the surrounding sandstone. In some cases these beds, which are the stratigraphic equivalents of those currently being exploited, are of comparable quality.

### 3.2.3.3 Sulphate minerals

The sulphate mineral gypsum is currently exploited in this region for agricultural purposes. Within the spectral range covered by TM7 (2.08-2.35  $\mu\text{m}$ ), gypsum has generally low reflectance and a shallow, centrally positioned, absorption feature (Figure 2.2). It also shows an absorption just within TM5 (1.55-1.75  $\mu\text{m}$ ). Work in the Wardan and Mreir sub-areas showed that the gypsum formations outcrop in wide rounded hills (Figure 3.8). This topographic expression is quite distinct from the interbedded clay deposits. Gypsum formations can thus be mapped using TM7 and TM5 absorption features, topographic expression, high albedo and also a high drainage density in comparison to surrounding clastic and carbonate formations.

---

<sup>1</sup> *Subsequent sampling and mineral processing work carried out by EGSMA (Razek et al., 1993) on these kaolinitic sandstones indicated significant levels of high-grade china clay - a commodity currently imported to Egypt for the ceramics industry. Insufficient work has been carried out to date to assess the economic potential of this deposit.*



**Figure 3.7** Unexploited kaolinite bands, Wadi Baba.



**Figure 3.8** Gypsum outcrop near Gebel Mreir.



**Figure 3.9** Argillaceous chalky clay outcrop, Upper Wadi Wardan.



**Figure 3.10** Dolerite sill (dark band) in Upper Cretaceous strata, Tih escarpment.

### 3.2.3.4 Carbonate minerals

The main absorption feature for carbonate minerals (e.g. calcite shown in Figure 2.2) is around  $2.34 \mu\text{m}$ , near to the edge of TM7 rather than at its centre. In addition, fieldwork suggests that the carbonate-bearing lithologies develop a weathered surface of iron minerals which masks this response. These effects lead to a weaker TM7 absorption which enables carbonates to be discriminated from clay and sulphate minerals. Indeed, in places they are characterised more by TM1 absorption due to the iron minerals in their weathered surfaces. The major exception is the Palaeocene Sudr Chalk; extensive occurrences of this lithology, both along the coast and on the central El Tih Plateau, are characterised by a purple tone on the ratio image (see cover photograph) indicating at least a component of TM7 absorption.

The strongest TM7 absorption related to a carbonate lithology occurs over an argillaceous chalk in the Wardan sub-area (Figure 3.9). Here, however, the absorption is largely due to the clay content of this lithology rather than the carbonate host<sup>2</sup>.

### 3.2.3.5 Other lithologies

The predominant lithology of the Late Precambrian basement in this area is a mica-rich granite containing scattered xenoliths of gneiss. While causing a mica-related TM7 absorption, it has a low overall albedo which makes it distinguishable from other areas of TM7 absorption.

Similar comments apply with regard to the characteristic outcrop form of dolerite dykes (labelled *d* in Figure 3.3). In fact, even where the dolerite forms sills, their low albedo distinguishes them from the clay minerals. These units also possess a shallow  $0.49 \mu\text{m}$  absorption (TM1) due to their iron content, which is not displayed by the clay minerals. The TM7 absorption in the dolerite is attributed to hydrated serpentinite/iddingsite derived from the weathering of olivine. The main olivine dolerite sill, which is up to 50 m thick and extends for at least 30 km eastward and northward along the El Tih Plateau (Figure 3.10), is clearly seen in the TM imagery but is not accurately portrayed on existing geological maps of the area.

## 3.2.4 Spectral analysis

Data for the Sinai study area were also studied using the T-Spectra software described in section 2.1.3. Whilst this study was guided by the knowledge gained during fieldwork, it nevertheless led to a better understanding of the geology of this area. This section first describes the spectral analysis of imagery from the Insaker sub-area, and then shows how this knowledge was applied to the Mreir area.

---

<sup>2</sup> *The clay minerals within the chalk may be palygorskite and attapulgite. If this is the case, the lithology may have economic application in drilling mud for marine platforms, where bentonite cannot be used. This is a commodity Egypt currently imports.*

#### 3.2.4.1 Insaker area

TM7 of the log residuals data for the Insaker area is shown in Figure 3.11. The data are not inverted, so areas of TM7 absorption appear dark. The figure illustrates some of the menu options of T-Spectra, such as scatter plots and spatial filters. The option highlighted is '*spectra*' which, when selected, pulls down a sub-menu containing a number of further options. The specific function selected, '*cursor*', allows the user to view the TM pseudospectrum for the pixel under the cursor or, as in this case, the mean pseudospectrum for a 3 x 3 pixel box centred on the cursor. In Figure 3.11, the cursor is located over the spoil from a known kaolinite mine. The corresponding pseudospectrum appears in the graphics box alongside, and may be further manipulated, compared to other spectra, or saved as desired. It is dominated by TM7 absorption and is typical of the mineral kaolinite in this study area.

In Figure 3.12, the cursor is located over an isolated fault block exposing the Sudr Chalk. It is clear that this pseudospectrum, whilst also displaying TM7 absorption, is quite different in detail from the kaolinite pseudospectrum, particularly in respect to its deeper TM5 absorption. Figure 3.13 shows the pseudospectrum for the kaolinitic sandstone. Whilst the lower reflectance toward TM7 is typical of kaolinite, the sandstone also shows an absorption in TM1, attributed to surface iron oxides. This pseudospectrum is again characteristic of this particular lithology. In Figure 3.14 the pseudospectrum for the dolerite dyke has a strong iron oxide related absorption in TM1 as well as the weaker TM7 absorption. It is clearly different to the previous three examples.

These known pseudospectra now provide a basis for analyzing unknown parts of the image. In Figure 3.15, the cursor has been placed over a TM7 anomaly of unknown origin; based on the shape of the pseudospectrum, it may be concluded that this is a similar occurrence of kaolinitic sandstone, and this was confirmed in the field. Figure 3.16 illustrates the successful use of this approach; here, the cursor is located over another anomaly which gives the typical kaolinite pseudospectrum. Field checking confirmed that this was due to a previously undiscovered kaolinite band.

#### 3.2.4.2 Mreir area

The spectral analysis for the Mreir sub-area, which contains extensive outcrops of gypsum, illustrates the consistency of the approach within a single TM data set. In Figure 3.17, the cursor is placed over an outcrop of the Sudr Chalk Formation. Comparison with the pseudospectrum from the Sudr Chalk of the Insaker area (Figure 3.12), shows that there is a good match between the two examples of this lithology. Figure 3.18 shows the pseudospectrum typical of gypsum outcrops in this area. This mineral also displays a TM7 absorption, but this is accompanied by absorption in TM5 and an iron oxide absorption in TM1. This gypsum pseudospectrum is clearly distinct from the kaolinite pseudospectrum seen in Figure 3.11 (as suggested by the theoretical study of TM's spectral capabilities reported in section 2.3).

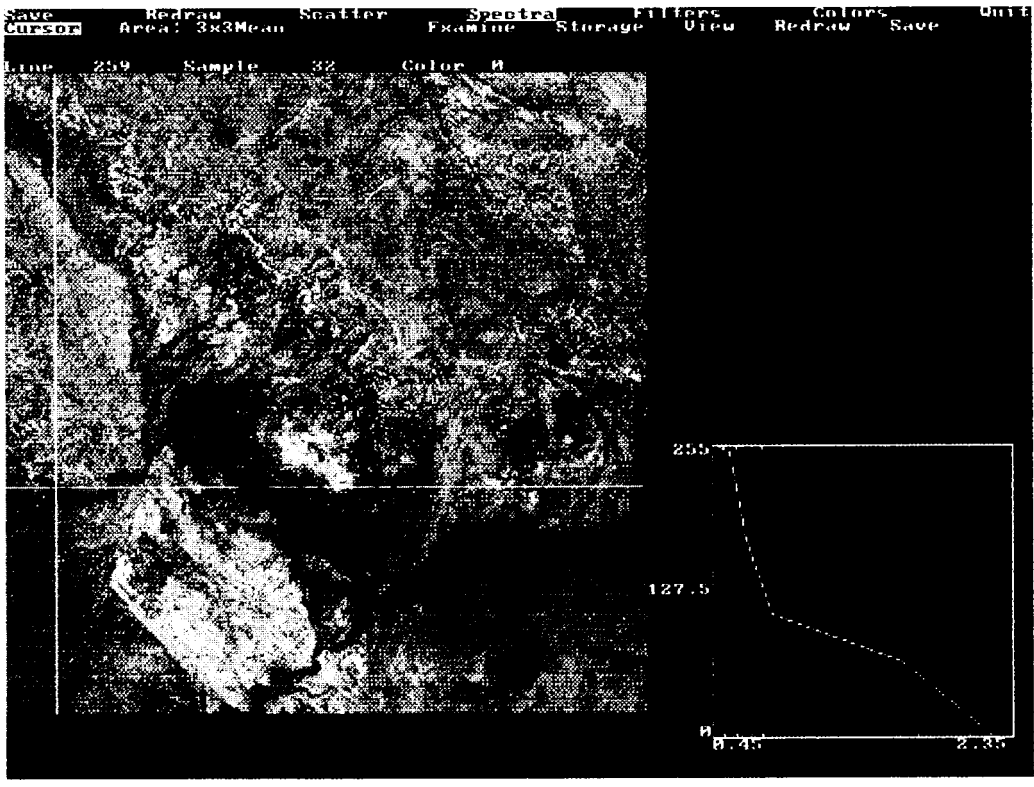


Figure 3.11 T-Spectral analysis, kaolinite mine, Insaker sub-area.

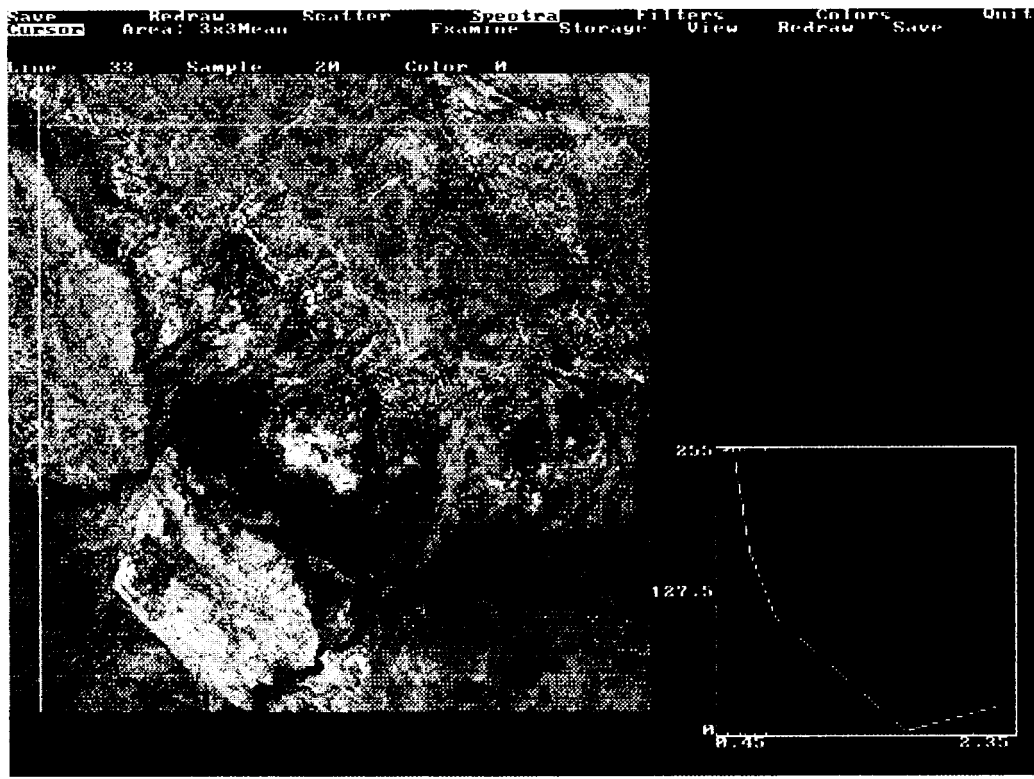


Figure 3.12 T-Spectral analysis, Sudr Chalk fault block, Insaker sub-area.



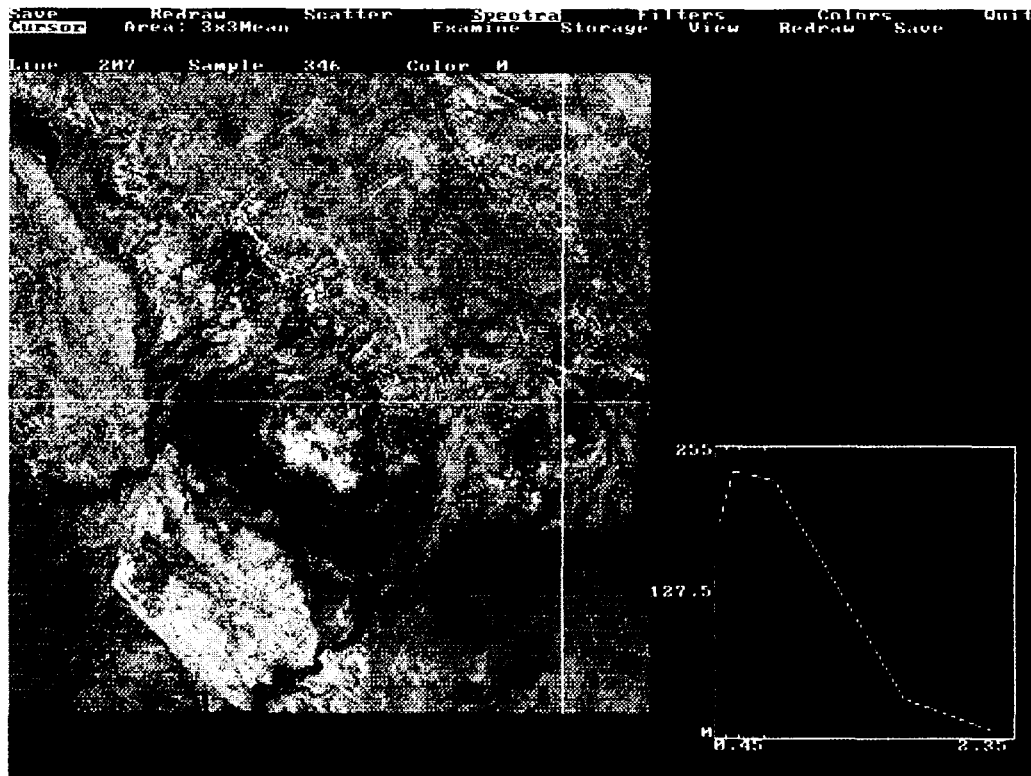


Figure 3.15 T-Spectral analysis, kaolinitic sandstone outcrops, Insaker sub-area.

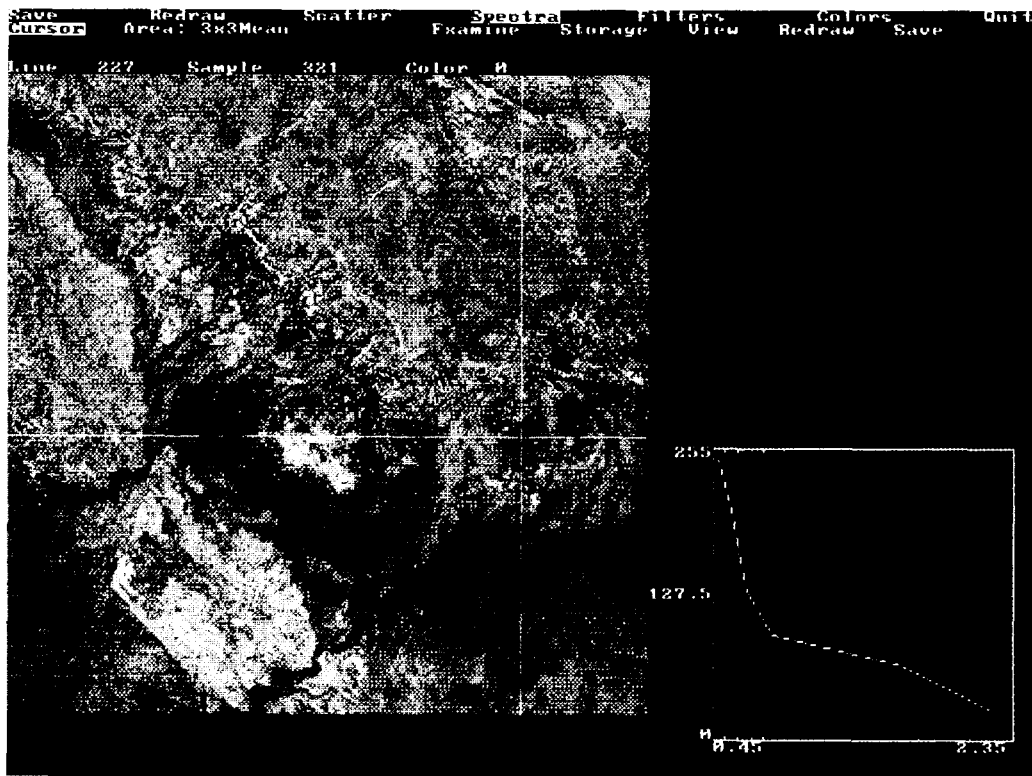


Figure 3.16 T-Spectral analysis, unmined kaolinite band. Insaker sub-area.

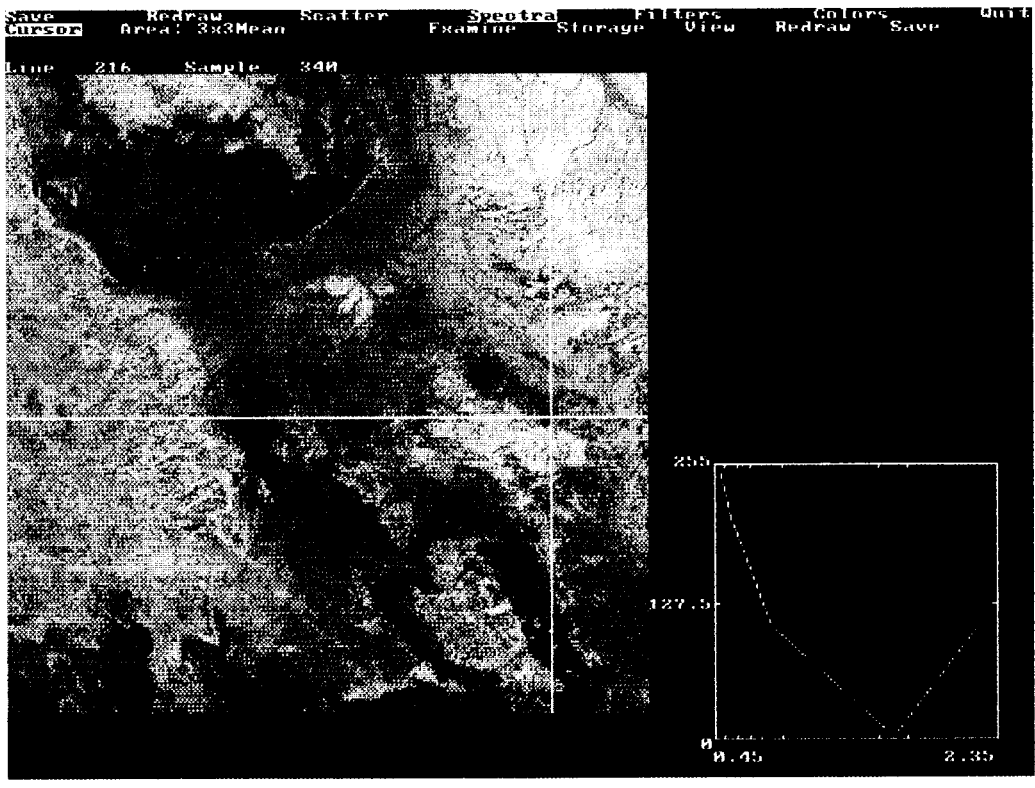


Figure 3.17 T-Spectral analysis, Sudr Chalk Formation, Gebel Mreir.

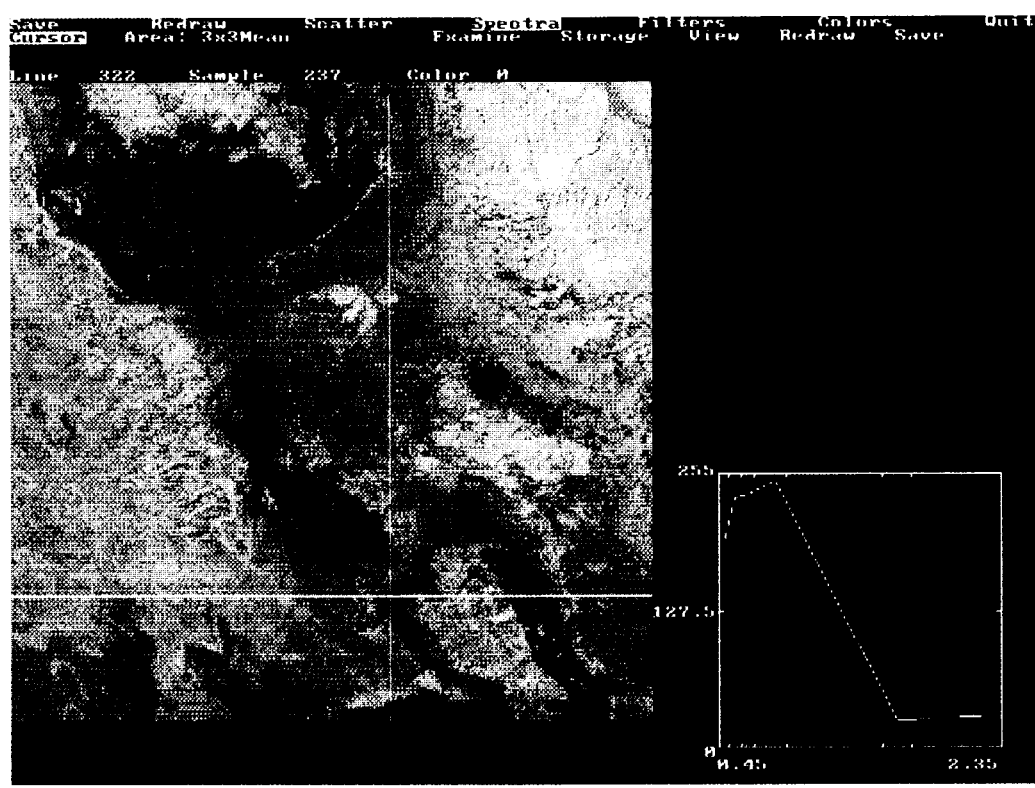


Figure 3.18 T-Spectral analysis, gypsum outcrop, Gebel Mreir.

### 3.2.4.3 Discussion of the spectral analysis work

Spectral ‘interrogation’ of the log residuals data allows various mineral deposits and lithologies which show TM7 absorption to be discriminated. The Sinai example provides a practical demonstration of the potential suggested by the theoretical study described in section 2.3. Conventional visual image interpretation usually confuses the materials here discriminated. Even if ground control were not available, the spectral analysis approach could be used to reliably sub-divide the image into various ‘unknown’ rock types by grouping occurrences of like pseudospectra. Prior knowledge of rock types allows names to be assigned to lithologies but, in either case, the spectral analysis approach represents a significant advance in the analysis of TM data.

The need for prior knowledge about the image can in theory be reduced by using laboratory reflectance spectra of the appropriate minerals, resampled to the TM wavelength bands. These can be compared to the unknown image pseudospectra visually or statistically, and provisional identifications made. For this to be possible, however, the calculated log residual pseudospectra must closely match the resampled laboratory spectra. Comparison of the image-derived kaolinite pseudospectrum in Figure 3.11 with the resampled laboratory spectrum shown in Figure 2.9 shows that, at least for the Sinai TM data, the two are a poor match, particularly in the VNIR wavelengths. Without prior knowledge it would not have been possible to identify kaolinite from the pseudospectrum at the mine site.

It is evident that, whereas the Sinai log residuals data approximate to reflectance, they are not precisely calibrated. This could be due to two main factors: (1) the atmospheric correction of TM data for Sinai may not be sufficiently accurate; (2) each log residual value does not purely represent the reflectance of one pixel at one wavelength<sup>3</sup>. This is discussed further in Chapter 5.

### 3.2.5 Laboratory results

Samples of each of the lithologies causing TM7 absorption were analyzed mineralogically and spectrally in order to further explain the spectral variations observed in the TM data. XRD analyses were carried out at the BGS on crushed and ground portions of 35 samples using a Phillips PW1700 series automatic diffractometer, scanning over the range 2-50 °2θ at a speed of 0.9 °2θ/minute (Prior, 1992). The absolute laboratory reflectance spectra between 0.4 and 2.5 μm for all 80 uncrushed field samples were measured using a GER Mk IV IRIS spectroradiometer. Table 3.1 summarises mineral identifications made using each of these techniques as well as thin section examination.

---

<sup>3</sup> *The log residual values retain contributions from mean reflectances for the whole scene at all wavelengths, sample  $i$  at all wavelengths, and wavelength  $\lambda$  for all samples (refer to section 2.1.2.5). If the means all approximate to unity, the logarithmic residual value will approximate to the reflectance, but the further the mean spectra depart from this ideal, the further the log residual data will deviate from the actual reflectance. The Sinai results suggest that some/all of these means contain spectral features which bias the results.*

Table 3.1. Field and TM observations, and the results of thin section, XRD and laboratory spectral analyses for mined and unmined kaolinite, kaolinitic sandstone, gypsum and dolerite.

Lithology	All kaolinite occurrences	Gypsum	Kaolinitic sandstone	Dolerite dykes/sills
Field observation	kaolinite, some salty	crystalline gypsum	fine grained quartz sandstone	brown/black hard dolerite
	fresh surfaces exposed	fresh surfaces exposed	?kaolinite and Fe-oxide rich weathered surface	altered ?olivine covers weathered surface
XRD analysis	quartz, kaolinite, anhydrite	gypsum, anhydrite, calcite	quartz, calcite, kaolinite	plagioclase, augite quartz, kaolinite ilmenite, smectite
Laboratory spectra	kaolinite	gypsum, ?anhydrite, Fe-oxide	kaolinite, quartz, goethite	olivine (altered), ?augite, ?feldspar
Thin section	n/a	n/a	quartz, mica, chlorite, calcite, ?clay mineral	plagioclase, clinopyroxene, ilmenite, talc iddingsite/olivine

### 3.2.5.1 Kaolinite beds

XRD analyses of 18 samples from both mined and unmined kaolinite bands give kaolinite and quartz as the main mineral species. The composition of the mined bands and the unmined bands is the same. Trace quantities of anhydrite and halite in many samples suggest an evaporitic mode of sedimentation. Figure 3.19 shows laboratory reflectance spectra for weathered mined kaolinite (A) and the debris over an unmined kaolinite bed (B). Absorptions at 1.4, 1.41, 2.17 and 2.21  $\mu\text{m}$ , typical of kaolinite, are equally strong in both spectra (the overall brightness difference is due to the weathered surface being smooth and bright while the debris produces shadows between clasts). Thus, both the XRD and reflectance spectra suggest that the unmined kaolinite beds detected with the TM data are of similar quality to the mined deposits. (However, it would clearly be necessary to carry out tests of physical properties in order to be certain of this). The less intense TM7 absorption noted over unmined kaolinite beds is believed to be due to their reduced exposure.

### 3.2.5.2 Kaolinitic sandstone

Sandstone samples, considered in the field to have a surface coating of up to 10% kaolinite, showed only minor or trace quantities of kaolinite in the XRD results. In thin section quartz, minor mica and chlorite were identified with interstitial carbonate and a ?clay mineral coating the quartz grains. The proportion of kaolinite is near the 3% detection limit of bulk XRD analysis. Figure 3.19 shows the laboratory reflectance spectra for two samples of the rock's

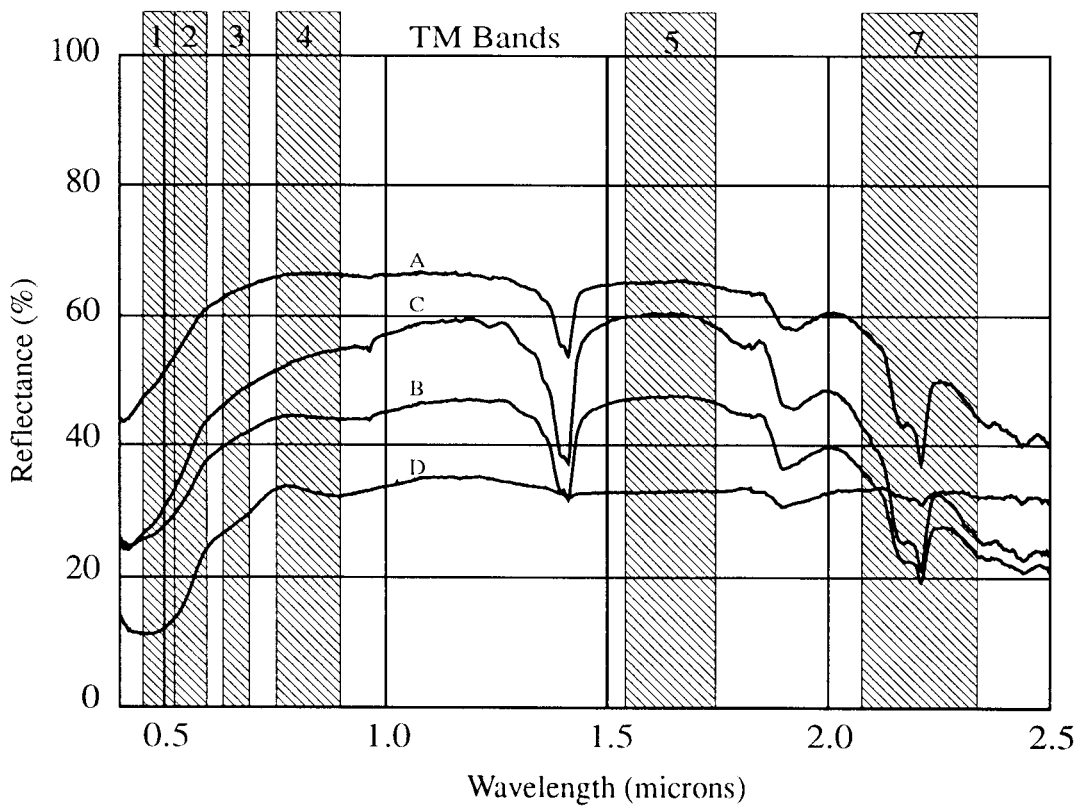


**Figure 3.19** Laboratory spectra, kaolinite mined (A) and unmined (B), and kaolinitic sandstone (C and D).

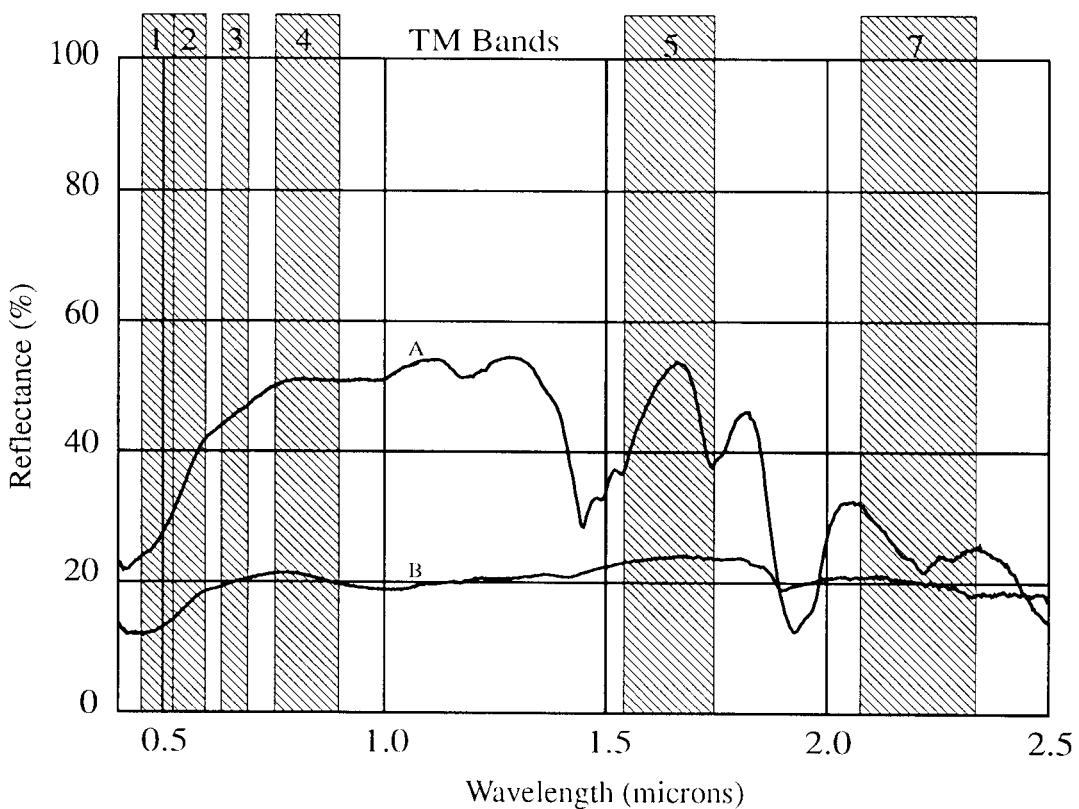


**Figure 3.20** Laboratory spectra, gypsum (A), dolerite (B).

weathered surface. Spectrum C displays kaolinite features of comparable strength to those of the pure kaolinite beds. Spectrum D, which is more typical of the sandstone outcrop, has reduced kaolinite features and only a small 2.2  $\mu\text{m}$  absorption. Additional absorptions occur at 0.47 and 0.89  $\mu\text{m}$  due to an increased iron oxide content. The laboratory spectra confirm that the TM7 absorption over this lithology is due to kaolinite, though somewhat subdued due to its low content and sometimes obscured by the development of iron oxides on the weathered surface.

### **3.2.5.3 Gypsum**

Samples of gypsum give unequivocal gypsum peaks in the XRD data and also show minor anhydrite and trace calcite and quartz. Figure 3.20 shows the laboratory reflectance spectrum of a weathered gypsum sample (A), which displays a broad, shallow absorption around 2.2  $\mu\text{m}$ . XRD and laboratory spectra indicate the same mineralogy and adequately explain the observations made with the TM data.

### **3.2.5.4 Olivine dolerites**

XRD analyses of the dolerite suite predictably show dominant plagioclase and augite together with minor ilmenite, but they also indicate high levels of smectite in fine fraction analysis. The latter is probably derived from the talc component, which is very distinctive in thin section. The olivine dolerite (spectrum B in Figure 3.20) displays no 2.2  $\mu\text{m}$  absorption, but has low reflectance across all wavelengths. Many other rocks in the area have developed iron oxides during weathering giving high reflectance values at longer wavelengths, so the dolerite's low reflectance will appear as a relative absorption by comparison. The talc and iddingsite masking the parental olivine, and the smectite identified in XRD analyses, may all contribute to reduced TM7 reflectance for this lithology.

### **3.2.5.5 Comments on laboratory results**

Overall, the laboratory data provide confirmation of the field studies and of observations made with the TM data. The XRD and laboratory spectra agree very closely for the high grade clay bands and gypsum beds, for which the mineralogy provides a clear explanation for TM7 absorption. In the case of the kaolinitic sandstones and the dolerites, however, the XRD analyses allow only a partial explanation of the remote sensing observations; this is probably due both to the lack of sensitivity of this analytical technique at low concentrations and the fact that it samples the bulk rock composition. In contrast, the laboratory spectral measurements permit the observations made with the TM data to be explained in all cases. The results also confirm the interpretation of the TM log residuals pseudospectra. Spectral differences between economic kaolinite beds and uneconomic kaolinitic sandstone, which are clearly-defined in the laboratory spectra, can still be used to distinguish between them in the imagery. The laboratory spectra correlate more closely with the TM data than do the XRD analyses because they are measurements of the weathered surfaces exposed to the satellite.

### **3.2.6 Summary of main Sinai results and conclusions**

The following main conclusions may be drawn from the Sinai work:

1. The band ratio technique applied to atmospherically corrected Landsat TM data successfully highlighted areas of TM7 absorption caused by gypsum or kaolinite in this arid, well-exposed area. Kaolinite and gypsum could be distinguished by differences in albedo and outcrop pattern. However, the method also highlighted TM7 absorption due to lithologies of no economic significance such as kaolinitic sandstone or weathered/altered dolerite.
2. Spectral interrogation of the logarithmic residuals TM data using T-Spectra made possible the separation of similar lithologies such as economic kaolinite and uneconomic kaolinite-bearing sandstones, based on differences in their TM pseudospectra. Using the knowledge gained at known mineral sites and field evidence, previously-undiscovered, high-quality kaolinite beds were located by targeting subtle, linear TM7 absorptions up to 1 km long and 1-2 pixels wide. The remote sensing analysis was confirmed and supported by laboratory mineralogical and spectral measurements on samples.
3. Various factors prevented the TM pseudospectra being properly compared with laboratory mineral spectra resampled to TM wavelengths. These difficulties are thought to include the lack of a precise atmospheric correction for the TM data, and the failure of the data to meet the assumptions behind the log residuals transform.

## **3.3 El Fayum**

### **3.3.1 Geology and setting**

The El Fayum area is one of a series of natural depressions in the Western Desert located about 80 km south west of Cairo (Figure 3.1). The deepest part of the depression is filled by Lake Birket Qarun and attains a depth of 45 m below sea level. A subsidiary, smaller depression, Wadi Rayan, lies to the south west. These depressions are flanked by prominent escarpments on the west (180 m asl) and Gebel Qatrani in the north reaches 350 m asl. The Qatrani escarpment is built out of a Tertiary lava suite overlying a set of scarp and sub-horizontal dip slopes conformable on the underlying Tertiary marl and clay strata (Figure 3.2).

The geology of the region (adapted from Beadnell, 1905 and EGSMA, 1983) comprises four stratigraphic units as follows:

QUATERNARY		Aeolian sands and eluvial gravel fans.
	Oligocene	Olivine basalt and dolerite sheets: ca 15 m
	Oligocene	Qatrani Formation: sands and sandstone with clay and marl intercalations: ca 20 m
TERTIARY	U. Eocene	Qasr El Sagha Formation: clay with sands and sandstone interbeds: ca 25 m
	U. Eocene	Birket Qarun Formation: fossiliferous sands and sandy limestone with clay bands: ca 40 m
	M. Eocene	Wadi Rayan Formation: yellowish-white limestone with <i>Nummulites gizehensis</i> : ca 120 m

The Wadi Rayan Formation, exposed to the south west of the Fayum depression, comprises pale limestones, marls and clays with abundant *Nummulites* fossils. The Birket Qarun Formation forms the lower escarpment zone north of Lake Qarun and is made up of alternating clays, sandy clays, limestone bands, sandy marls and friable sandstone. These are conformably succeeded by a similar alternating sequence of gypsiferous clays, thin highly fossiliferous limestones, and sandy clays of the Qasr El Sagha Formation, which underlies the middle and higher relief escarpment zone. This escarpment zone dominates the topography of the region bordering the northern sector of Lake Qarun, and is extensively veneered by sand drifts and lobate gravel fans. Broad terraces built on hard limestone beds are mantled by eluvial chert and pebble gravels.

The selection of areas for studying clay formations was helped by a clay and shale occurrence map in Qusa (1986). A possible bentonite clay occurrence near the Qasr El Sagha Roman temple site was visited by members of the BGS Mineralogy and Petrology Group (Morgan and Inglethorpe, 1990) and was briefly revisited by the project team in 1992 (O'Connor and Marsh, 1992).

### 3.3.2 Image processing

The image processing strategy adopted for this work followed closely that of the western Sinai study (Marsh and O'Connor, 1992). A Landsat TM (moving) quarter scene 177/039-040 acquired on 28 July 1985 was examined and sub-scenes covering the sites illustrated in the Qusa report selected for detailed digital processing (Figure 3.1). Following an atmospheric correction, using the Qarun Lake as a dark object, the data were processed by various methods and the following screen prints produced:

- i) FCC: bands 7 (red), 4 (green), 1 (blue)
- ii) Colour ratio composite: bands 5/7 (red), 5/4 (green), 5/1 (blue)
- iii) Principal components: PC1 (inverted)

- iv) PC composite: PC4 (red), PC2 (green), PC1 (blue)
- v) Inverted log residuals: band 7 (red), band 4 (green), band 1 (blue)

### **3.3.3 Evaluation and field correlation**

The field base was located at the village of Kom Oshim in the north east sector from where several defined tracks across the escarpment area were known. An initial reconnaissance visit showed that access in this desert terrain was more difficult than in Sinai, due mainly to the presence of sand drifts and poorly defined wadi systems. Tracks beyond the Ptolemaic temple of Qasr El Sagha to the west diminish in number and it was deemed necessary to have two vehicles, using one as back up on the main track for emergency. Difficult terrain limited the scope of field investigations to the lower escarpment zones encompassing the Birket Qarun and Qasr El Sagha Formations.

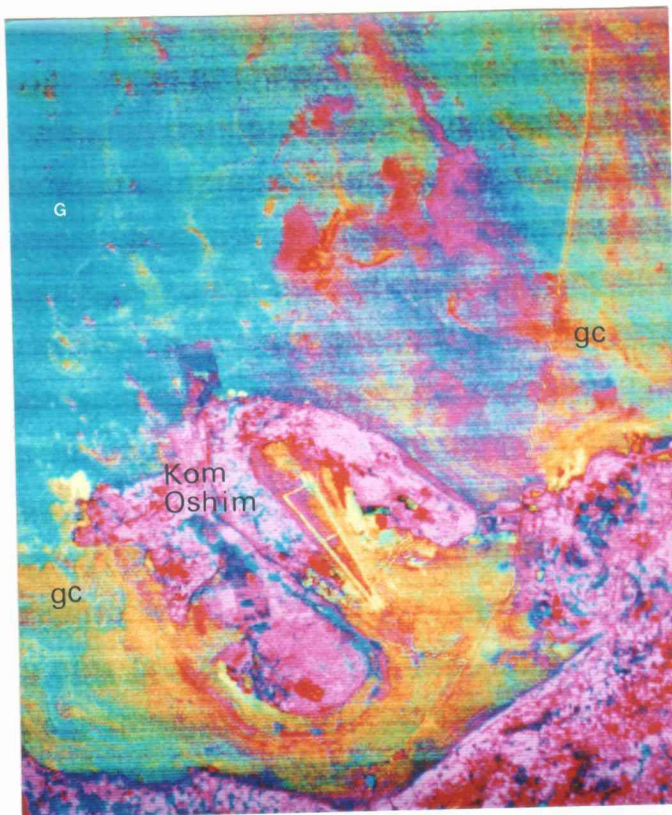
Landsat imagery, 1:40 000 scale aerial photographs and a topographic map to were used to locate sample sites. The most useful imagery products proved to be the 7-4-1 band composites for location, 5/7, 5/4, 5/1 ratio composites for general lithological separation, and log residuals composites (bands 7-4-1 inverted) for the more precise identification of units showing TM7 absorption.

#### **3.3.3.1 Brick clays**

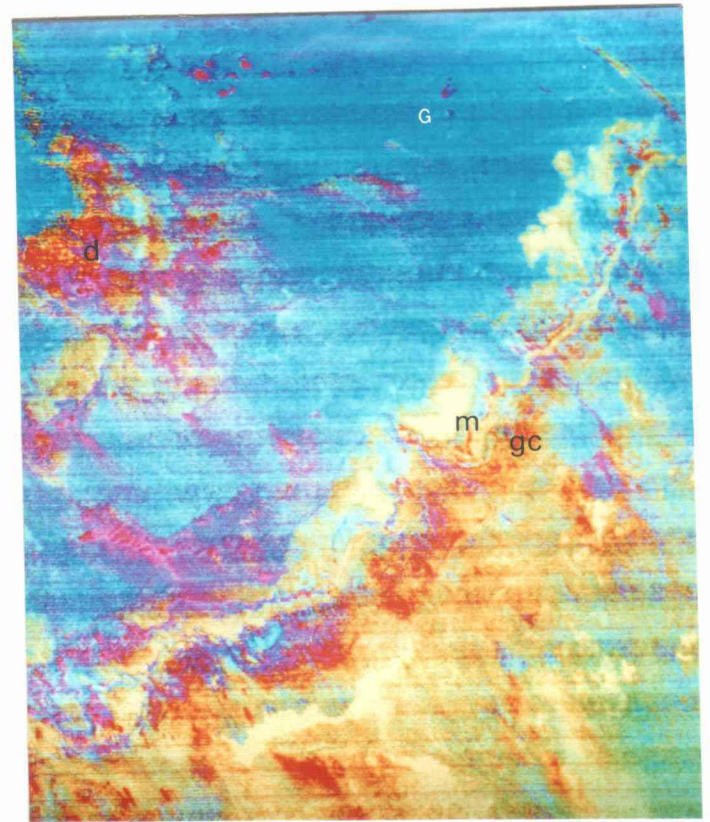
The city of Medinet El Fayum and the surrounding agricultural district within the Fayum oasis is highly populated and there is a large demand for building bricks. The clays of the Birket Qarun Formation, exposed in the sloping ground above Qarun lake shore and the sand-covered lowlands to the east near the main highway, were previously investigated as a source of brick-clays (Qusa, 1986). These clays are less sulphate-rich than the Qasr El Sagha Formation and have been extensively trenched in the area immediately west of Kom Oshim village in the eastern sector. These slightly-gypsiferous clay surfaces give a characteristic yellow-orange-red mottled colouration on a log residuals 7-4-1 inverted image (Figure 3.21A). Undisturbed gypsiferous clay surfaces to the north of the village, both east and west of the main highway into the oasis, produce a distinctive crimson red colour caused by strong TM7 absorption. There has been some exploitation of clays and sand deposits exposed in the footslopes of the main escarpment at the western end of Qarun Lake near the villages of Dar Es Salaam and 'second' village. These are seen in the log residuals data for the area (Figure 3.21C) as a discontinuous band of yellow, caused by TM7 and TM4 absorption, which corresponds to bedding. The imagery thus indicates the greater geographical extent of this poorly investigated clay resource surrounding this expanding agricultural settlement.

#### **3.3.3.2 Gypsiferous clays**

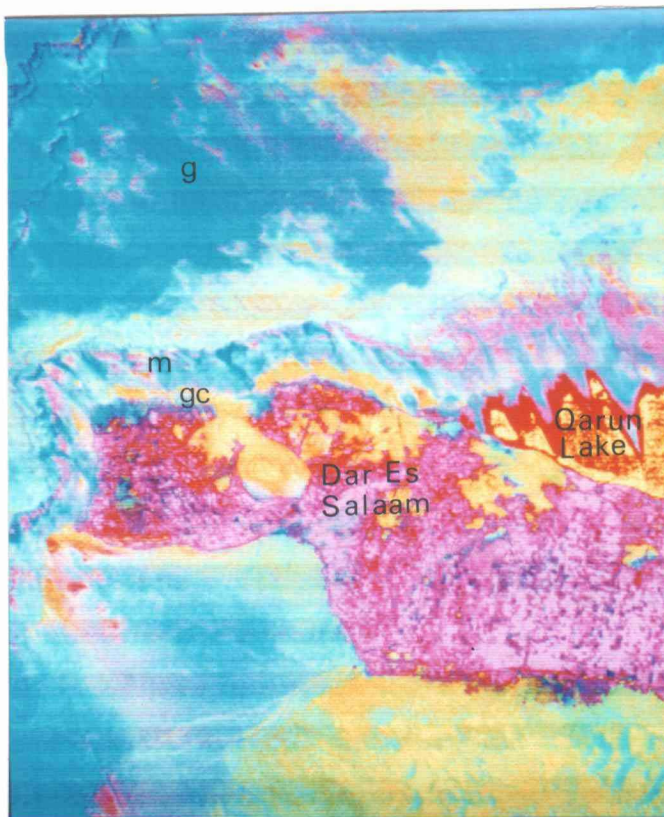
The lithologies of both the Birket El Qarun and Qasr El Sagha Formations are characterised by alternations of sandy limestones, gypsiferous clays, and hard marl beds (Figure 3.22). The limestone and marl beds give rise to prominent benches or terrace edges whereas the softer clay beds produce moderately sloping scree surfaces (Figure 3.23). In parts of the area, the



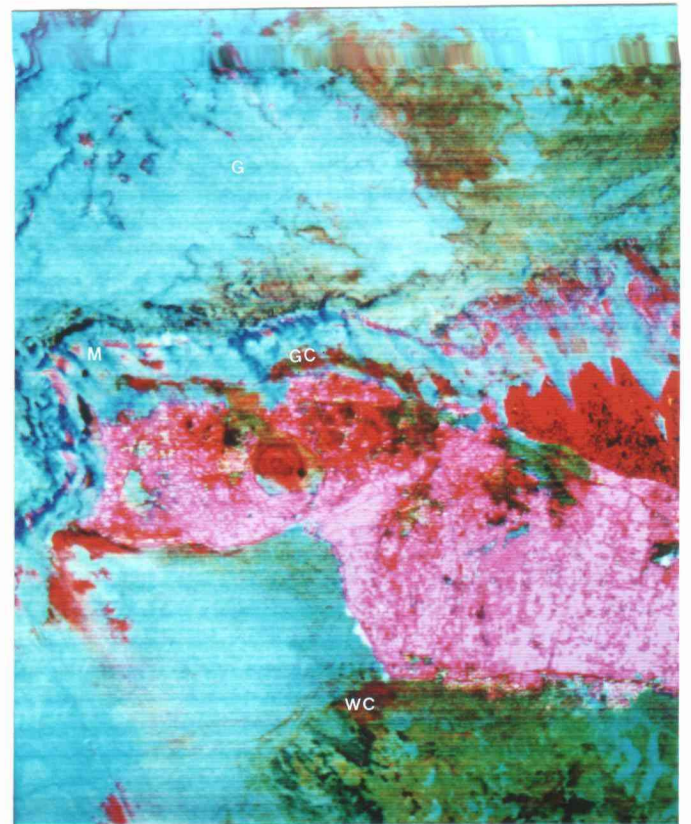
A



B



C



D

**Figure 3.21** Log residuals bands 7 4 1, inverted (R G B), (A), Kom Oshim sub-area, (B), Qasr El Sagha, (C), Dar Es Salaam village, West Qarun Lake, (D) Colour ratio composite, bands 5/7, 5/4, 5/1 (R G B), West Qarun Lake. Gypsiferous clays (gc), marls (m), gravels (g), weathered carbonate (wc).

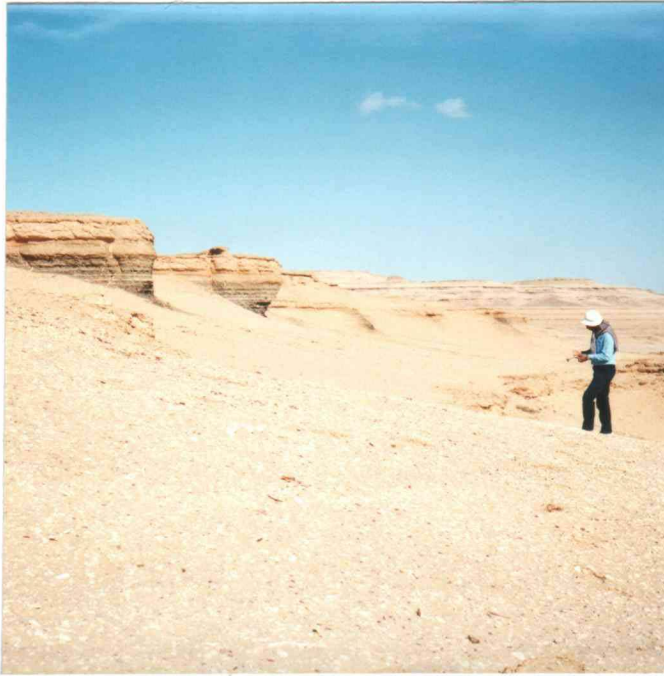


**Figure 3.22** Outcrop of marl terrace and gypsiferous clay scree slope, Qasr El Sagha, Fayum.

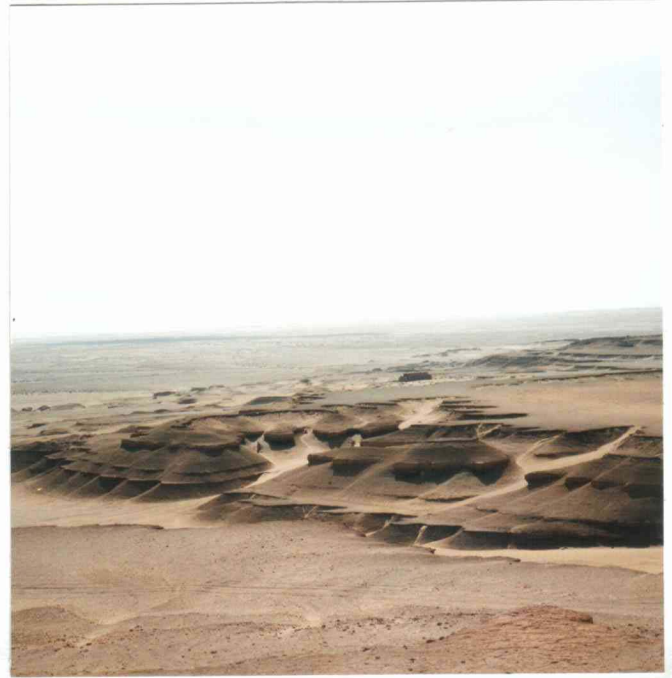


**Figure 3.23** Landscape expression of alternating marl bands and gypsiferous clays, Qasr El Sagha, Fayum.

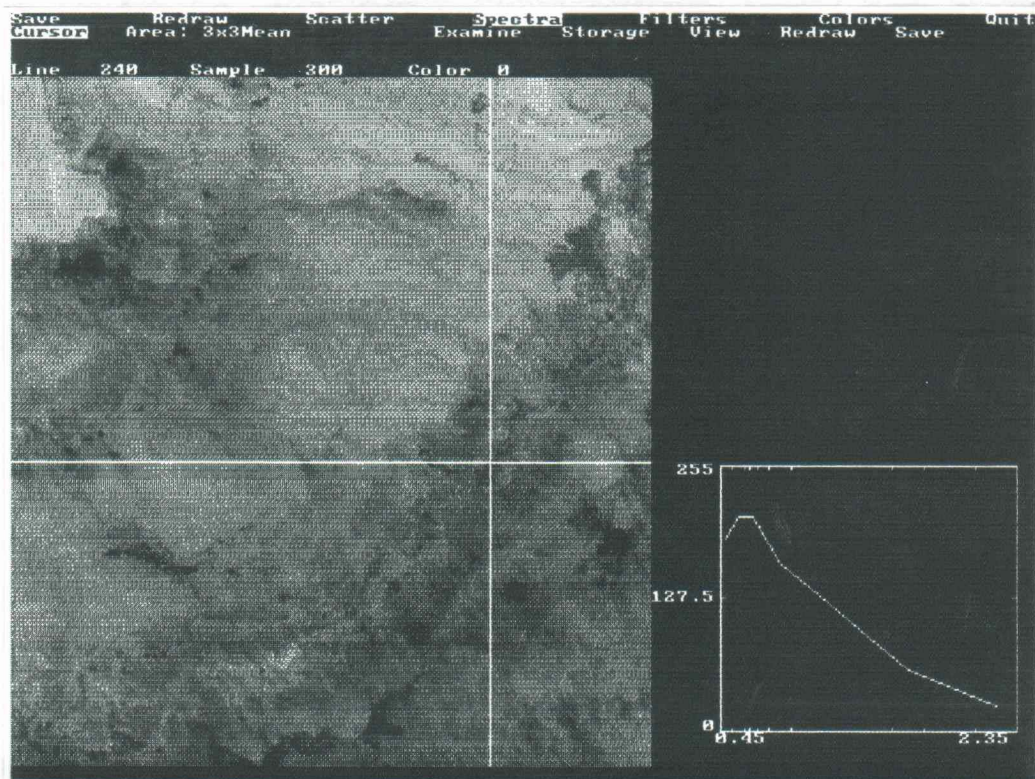


**Figure 3.24** T-Spectral analysis, marl bands, Qasr El Sagha, Fayum.

stratigraphic boundary between the two formations is an extensive hard sandy limestone bench, or mesa, which is strewn with desert-varnished chert and ironstone pebbles.

The gypsum-rich clay beds account for the strongest TM7 absorption corresponding to red/violet on the log residuals image, whereas the less sulphate-rich clays, and interbedded calcareous and sandy clays and marls, appear in yellow and mottled red. In the eastern escarpment zone around the Roman Temple of Qasr El Sagha, the alternating gypsiferous clays and marl/limestone beds give characteristic absorption patterns in log residuals imagery (Figure 3.21B). Wind-blown talus dunes are seen as thin 1 to 3 pixel wide trails south of the main escarpment.

A deep red to violet colour characterises the dark clay soils of the reclaimed agricultural area of Dar Es Salaam and 'second' village at the western extremity of the lake. Log residuals 7-4-1 composite imagery concisely maps TM7 absorption (in red) and discriminates between calcareous clays (yellow) and gypsiferous clays (pink-red) within the Birket Qarun Formation (Figure 3.21C). A pronounced TM7 absorption with a scarlet hue fringes the lake shore east of Dar Es Salaam village and is thought to be due to reed growth as it has the same scarlet hue as the crop cultivation. The triple ratio image (5/7 red, 5/4 green, 5/1 blue) provides good overall discrimination between OH-bearing clay, carbonate, iron oxide- and hydroxide-altered lithological units, as well as vegetation patterns in the oasis area (Figure 3.21D). The 5/7 component in pinkish-red confirms the presence of two major clay interbands within the Birket Qarun Formation which crop out as discontinuous bands or benches in the lower escarpment zone. The stratigraphically lower of these two bands has been referred to above under brick-clay resources.

Clays of the Birket Qarun Formation and the lower levels of the Qasr El Sagha were previously analyzed and trenched as potential bentonite-clay deposits (Qusa, 1986). The sandy clays with lower sulphate content clearly form the natural base of the agricultural soils, and demonstrate that bedrock clays of this type and at this stratigraphic level could be quarried and applied directly to the sandy soil areas designated for irrigation elsewhere in the Nile valley.

### **3.3.3.3 Carbonates**

The clay/marl succession in west Fayum is underlain to the south of the cultivation area by pale-yellow sandy limestones of the Wadi Rayan Formation which give a mottled red-brown 5/7 signature, probably related to clay or altered carbonate (south edge of Figure 3.21D). A greenish-yellowish and mottled blue tone probably signifies the presence of iron oxides and hydroxides, possibly as a desert varnish. Similarly, a sandy limestone unit overlying the clay/marl sequence is mottled red-brown-green implying the presence of clay/carbonate and iron hydroxides. Limestones and marls of the Qasr El Sagha Formation in the Roman Temple district are coloured yellow in the log residuals 7-4-1 image (Figure 3.21B).

### **3.3.3.4 Other lithologies**

The Qasr El Sagha site provides a second example of TM7 absorption related to magnesium hydroxyl minerals of the olivine group. A strong red-yellow zone in both the ratio and log residuals images (e.g. Figure 3.21B) is caused by the Oligocene basalt/dolerite sheets. These

non-clay targets can be readily distinguished from their clay counterparts by their low albedo in the 7-4-1 FCC.

Large areas of colluvial desert-varnished sand/gravel fans derived from Qatrani Formation sandstones give a dark blue tone on the 7-4-1 log residual composite owing to iron oxide coatings (Figure 3.21) which result in strong TM1 absorption.

#### **3.3.4 Spectral analysis**

The spectral analysis approach can be successfully applied to the El Fayum data allowing many lithologies producing TM7 absorption, such as dolerite and limestone, to be separated. However, some of the lithologies of economic interest have very mixed mineralogy. For example, the TM pseudospectra for the gypsiferous clay and the marl bands represent mixed surfaces containing carbonate, gypsum, clays and various iron minerals; deciphering these mixed signal responses is difficult. The El Fayum sub-area thus provides a challenge to the spectral analysis technique not seen in Sinai.

Figures 3.24 and 3.25 show pseudospectra from a single marl band in the Qasr El Sagha area. Figure 3.24 looks similar to a kaolinite pseudospectrum from Sinai and is typical of areas within the marl band appearing red in the log residuals colour composite (Figure 3.21B). Figure 3.25, which is similar to the carbonate pseudospectrum of the Sudr Chalk in Sinai, occurs in parts of the marl band appearing yellow. Figures 3.26 and 3.27 depict pseudospectra from a gypsiferous clay band lower down the escarpment; both types of pseudospectra are also found in this second unit. The marl band and gypsiferous clay band clearly have highly mixed mineralogy in their exposed surfaces and it is therefore difficult to distinguish between them on the basis of isolated pseudospectra. They can, however, be discriminated visually in the log residuals FCC image shown in Figure 3.21B. This is because the colour composite provides a synoptic view of the distribution of the two spectral signatures; overall in the log residuals image, the marl band appears predominantly yellow whereas the gypsiferous clay band is more often red.

The El Fayum data thus illustrates the problems of separating mixed materials, particularly using data with fairly coarse spectral resolution such as Landsat TM. The example from Qasr El Sagha demonstrates the continuing importance of conventional interpretation techniques. The spectral analysis approach complements, rather than replaces, visual analysis methods in which outcrop pattern and albedo remain important discriminating factors for geological materials.

#### **3.3.5 Laboratory results**

Samples collected by the BGS Mineralogy and Petrology Group from pits excavated near the Qasr El Sagha Roman Temple site (where Qusa (1986) cited bentonite occurrences) were subjected to mineralogical and physical tests to evaluate their potential as industrial bentonites. This work was carried out at the BGS earlier as part of a training exercise for one of the EGSMA counterparts involved in industrial mineral investigations (Inglethorpe, Bloodworth and Razek, 1990). The results suggested that these bentonites were unsuitable for foundry clay and drilling fluid applications. The presence of gypsum and calcite would also make them unsuitable for certain industrial applications.

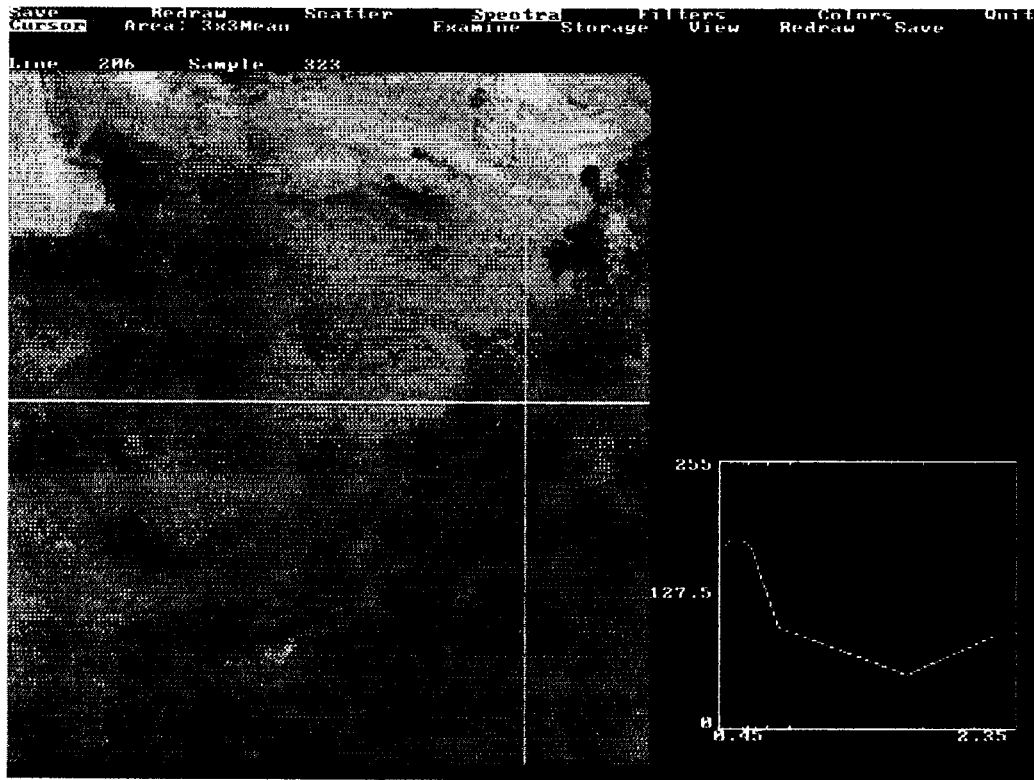


Figure 3.25 T-Spectral analysis, marl bands, Qasr El Sagha, Fayum.

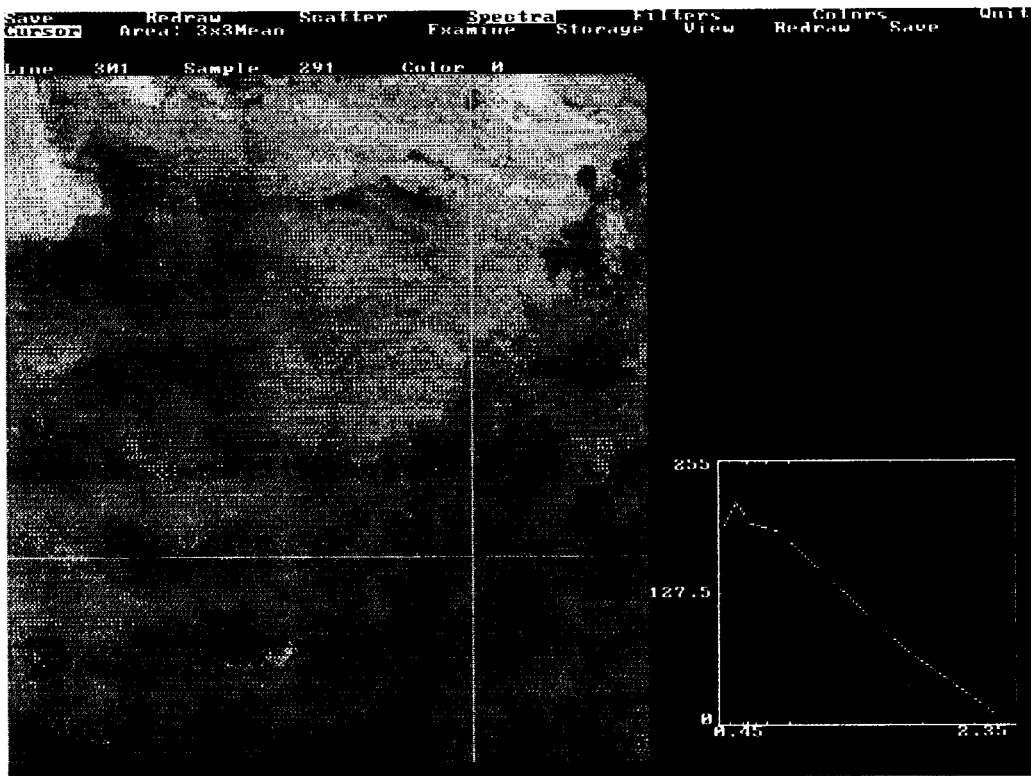
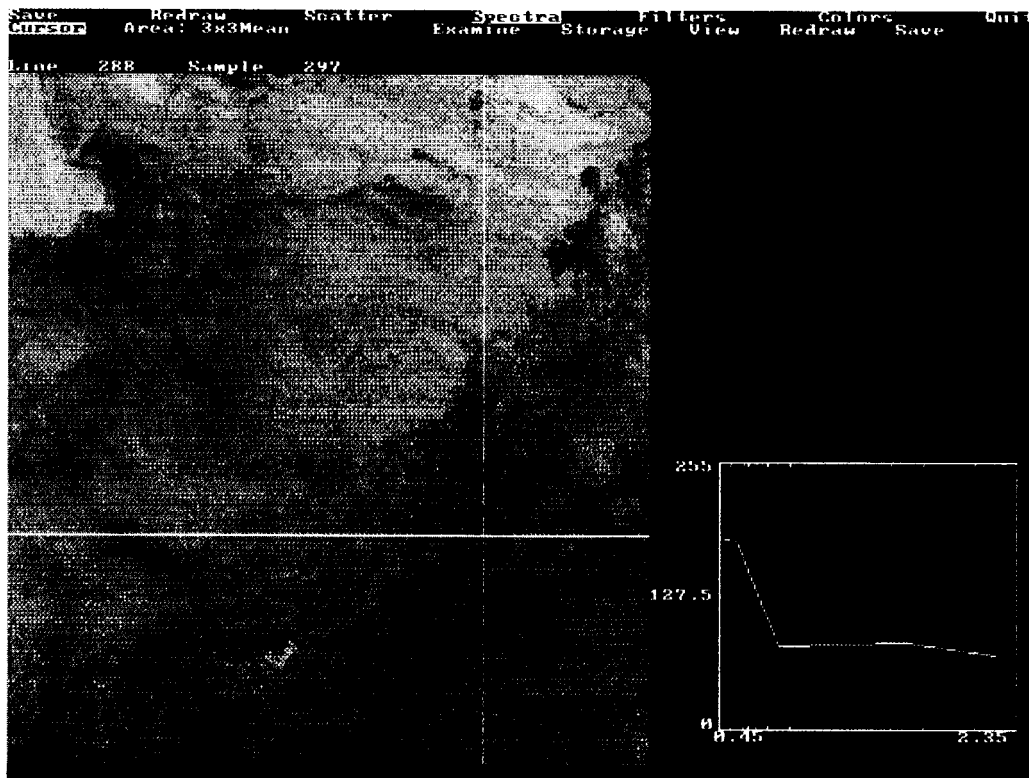
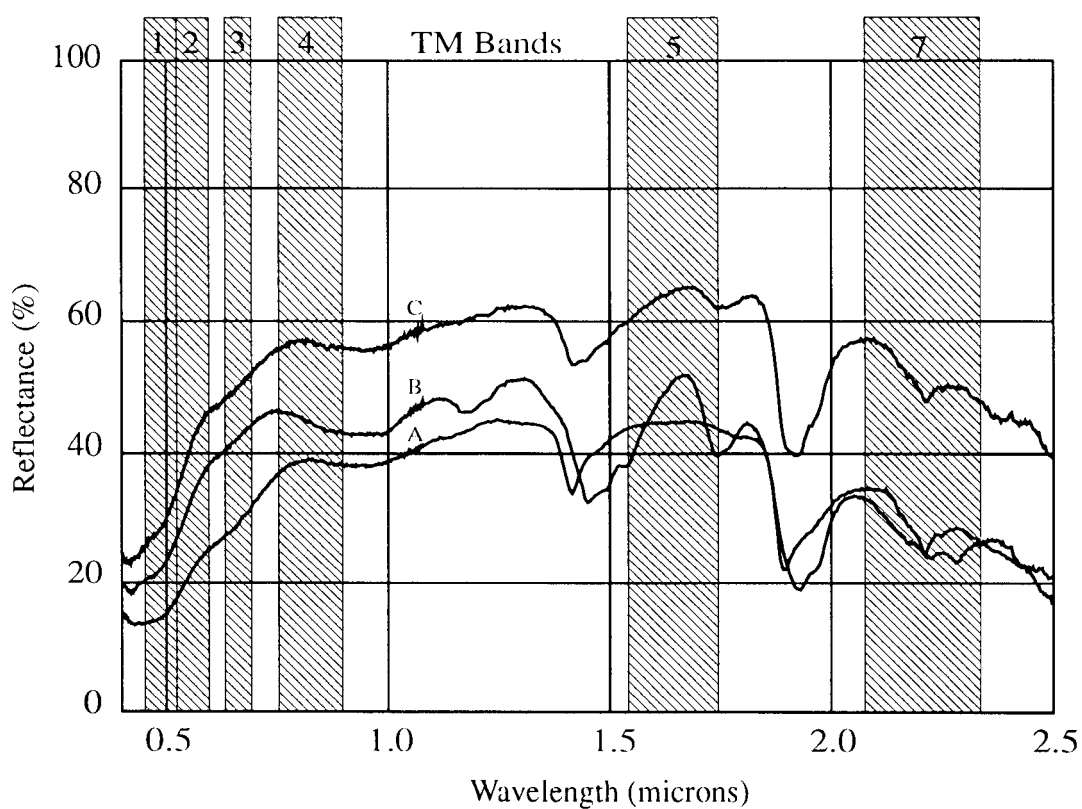


Figure 3.26 T-Spectral analysis, gypsiferous clays, Qasr El Sagha, Fayum.



**Figure 3.27** T-Spectral analysis, gypsiferous clays, Qasr El Sagha, Fayum.



**Figure 3.28** Laboratory spectra, montmorillonite (A), gypsum and iron-oxide/hydroxide gravel (B), and mixed clay-limestone-gypsum scree (C), Qasr El Sagha Formation, Fayum.

XRD work was also carried out at BGS on samples collected in the Fayum area during this project (Prior, 1992). A range of non-clay minerals were detected from whole-rock fractions in which quartz, feldspar, calcite and gypsum were the main constituents. Despite the apparent abundance of gypsum in the field, its concentration in the whole rock fraction was anomalously low, possibly due to only partial dissolution of the soluble phases by the cold water extraction method used. Clay family minerals detected from a  $<2 \mu\text{m}$  fraction were smectite, kaolinite/chlorite and illite. Smectite clay was in the range 22-49%, kaolinite/chlorite contents were recorded as medium to weak, and illite as weak to trace.

Laboratory reflectance spectra of 46 samples of fresh and weathered rock from the El Fayum site were measured (Marsh and Tragheim, 1995) and compared with library mineral spectra. Samples of the Qasr El Sagha and Birket Qarun clay beds yielded diagnostic spectral curves for montmorillonite (A) and also showed spectral characteristics of iron oxide and hydroxide between 0.4 and  $1.24 \mu\text{m}$  (Figure 3.28). In contrast, surficial colluvial gravels derived from scree slopes gave spectra diagnostic of both gypsum and iron oxides/hydroxides (B). These spectra show distinctive minor absorption features around both  $1.5 \mu\text{m}$  and  $1.9 \mu\text{m}$  (Figure 3.28). Scree slope samples, comprising a heterogeneous assemblage of clay, limestone and gypsum fragments, produced similarly mixed spectra with weak iron oxide absorption in the 0.4 to  $0.82 \mu\text{m}$  wavelength range, minor features attributable to gypsum at  $1.5 \mu\text{m}$ , and an asymmetric curve at  $1.8 \mu\text{m}$  followed by a negative slope towards  $2.5 \mu\text{m}$  probably attributable to an unspecified clay mineral.

Spectra of surficial limestone gravels from the Wadi Rayan Formation gave characteristic calcite absorption features at about  $2.3 \mu\text{m}$  but also showed gypsum absorption features (Figure 3.29A). The spectrum of an olivine dolerite sample is distinguished by its flat shape and overall low reflectance (Figure 3.29B). There are minor absorption features at  $0.4 \mu\text{m}$  due to iron oxide and at  $2.3 \mu\text{m}$  attributed to MgOH minerals and/or chlorite alteration.

The XRD and IRIS data show good correspondence with the field observations. Clay samples of both the Birket Qarun and Qasr El Sagha formations, interpreted as smectites in the XRD data, correlate with montmorillonite diagnosed from the IRIS spectra. The spectroradiometer data are more sensitive to small amounts of gypsum. IRIS spectra also confirmed that the weathered surficial materials overlying these clay/marl units vary in their concentrations of either gypsum or iron oxides/hydroxides relative to the clay fraction. IRIS spectra of the olivine dolerite and limestone material confirm the 2.2 to  $2.3 \mu\text{m}$  absorption which is evident on TM log residuals and ratio images for these lithologies.

### 3.3.6 Summary of El Fayum results and conclusions

Work in the El Fayum area showed the following.

1. Many of TM7 absorptions detected were due to mixtures of materials (weathered clay and surface gypsum debris, calcite in weathered limestones and magnesian minerals in altered olivine-dolerite). Consequently, the area is much more difficult for remote sensing. Notwithstanding these problems, logarithmic residuals is probably the most effective tool for minerals mapping in this environment. Again, some separation of lithologies causing TM7 absorption was achieved using a combination of outcrop pattern, albedo and absorption features at other wavelengths.

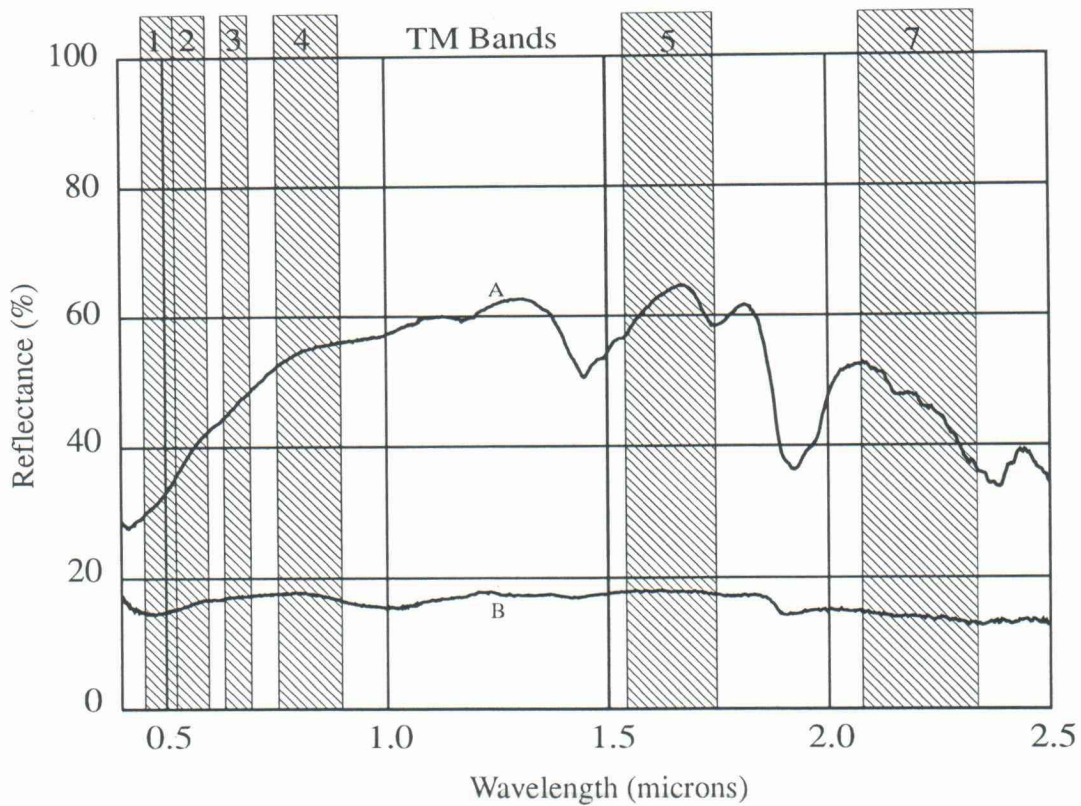


**Figure 3.29** Laboratory spectra, carbonate/limestone gravel, Wadi Rayan Formation (A) and dolerite (B), Fayum.

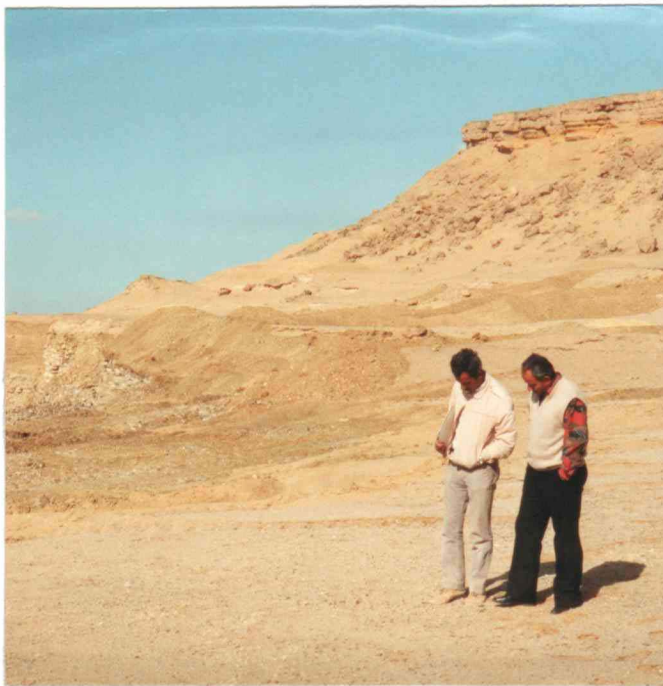


**Figure 3.30** Marl terrace and marly sand scree slope covering gypsiferous clays with excavation pits for brick-clays, Km 30 Cairo-Suez road.

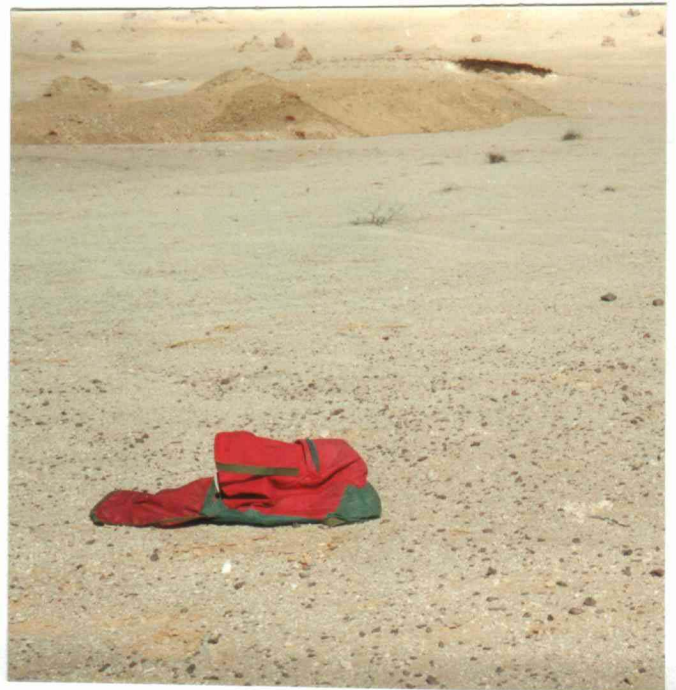


**Figure 3.31** Surface gravel composed of carbonate, marly sand, gypsum and iron-oxide debris. Brick factory site, Km 30 Cairo-Suez road.

2. Spectral analysis using T-Spectra was less successful in this mixed-lithology environment. Here, the separation of minerals and lithologies carrying a broad TM7 absorption ultimately depended on a combination of applied photogeology, prior geological information, spectral analysis and/or fieldwork. Results from this site illustrate the limitations of the broadband TM sensor in detecting subtle spectral absorption differences.

### 3.4 Cairo-Suez area

#### 3.4.1 Geology and setting

The region between the metropolis of greater Cairo and the town of Suez at the south end of the Suez canal is a broad undulating plateau some 100 m asl rising to elongate ridges and peaks in the central and eastern sector such as Gebel Iweibid at 520 m asl. A number of escarpments in the southern sector are related to resistant Miocene limestones and Oligocene basalt/dolerite sills. The plateau is dissected by several north-flowing wadi systems which funnel into a main wadi channel of Wadi El Gafra in the central sector (Figure 3.1).

The geology of the region (Figure 3.2) modified from Said (1962) and EGSM (1983) comprises seven stratigraphic units as follows:

QUATERNARY		Aeolian sands and eluvial gravels
	Pliocene	Gravels and thin limestone
	Upper Miocene	Grits and gravels
	Lower Miocene	Shelly limestones, clays and marls
TERTIARY	Oligocene	Basalt/dolerite flows: c 20 m Gebel Ahmar Formation; sands, gravels with petrified wood
	Upper Eocene	Anqabia Formation; sands and sandstones with clay intercalations: c 60 m Maadi Formation; sandy limestones, marls and clays: c 60 m Giushi Formation; white limestone: c 50 m
	Middle Eocene	Mokattam Formation; hard, crystalline dark-weathering limestones: c 120 m

The sand and gravel units within the Gebel Ahmar Formation are extensively quarried for aggregate especially in the vicinity of Gebel Nasuri and Anqabia; pits up to 60 m deep were

found in the thicker parts of the succession. The basalt/dolerite sills are also worked and crushed as an additive for brick manufacture. Most of the clays for the brick-manufacturing industry are won from the lower Miocene units exposed north of Gebel Nasuri on either side of the Cairo-Suez road, whilst dolomitic limestones from the same Miocene sections are used in concrete block production. White sandy limestones from the Miocene are used as ornamental stones.

### **3.4.2 Image processing**

The image processing strategy was similar to that used for Sinai and El Fayum. A Landsat TM scene 176/039 acquired 9 August 1989 was processed for most of quadrants 2, 3 and 4. The outputs comprised:

- i) A 1-5-7 FCC.
- ii) A 5/7, 5/4, 5/1 ratio composite.
- iii) An inverted log residuals 7-4-1 image.

The log residuals transformation was carried out on the full quarter scenes rather than on small sub-areas. The statistics were collected so as to avoid areas of vegetation and the cultivation zones of the Nile Valley.

### **3.4.3 Evaluation and field correlation**

The Cairo-Suez area has become the major source of construction materials for three new cities. The area has several asphalt highways and older roads, as well as gravel-surfaced tracks. The terrain is flattish to undulating with a predominant sandy cover, making navigation difficult. The presence of military training bases in this district meant that access was restricted to areas of industrial mineral quarrying and other non-military zones.

Once again, TM imagery, 1:40 000 scale aerial photographs and a 1947 topographic map were used to assist the location of sample sites. FCCs of bands 1-5-7 provided good contrast for navigational purposes in this monotonous and generally sand-covered terrain. 5/7, 5/4, 5/1 ratio composites were used for geological discrimination and 7-4-1 inverted log residuals composites for the more precise identification of units showing TM7 absorption.

#### **3.4.3.1 Brick clays**

The brick manufacturing zone which serves the rapidly growing building industry of greater Cairo and three new cities near the Cairo-Ismalia road is located at kilometre 30 along the Cairo-Suez road. Beds of clay and sandy marls of the Upper Eocene Anqabia Formation are patchily exposed in the vicinity and are exploited by two brick-making companies. Clay bands from a similar Lower Miocene sequence of sandstones, limestones and marls occurring north of the old Cairo-Suez road are also exploited for brick production. The clay bands are invariably obscured by colluvial carbonate-sand derived from the overlying sandy marl beds (Figure 3.30). The clay bands, which are the stratigraphic equivalents of the Eocene successions in El Fayum, are similarly strongly dissected by gypsum veins; in quarry

cuttings, the clays are green-buff in colour. Surface gravels consist of an intimate mixture of carbonate, gypsum and marly sand (Figure 3.31).

Thin clay bands interbedded with marls and shelly limestones, common in both Eocene and Miocene successions, are discriminated from surrounding carbonate units using the log residual imagery. The inverted log residuals 7-4-1 image (Figure 3.32) depicts the gypsiferous clays and carbonate veneer as a mottled mixture of pink-red and yellow. Gypsum debris contributes a certain proportion of the scree slope which gives a weak TM7 absorption response. The mixed surface gravels of carbonate, gypsum and marly sand include some iron hydroxides in the weathering product and give a yellow colour due to a mixture of TM7 and TM4 absorption, the latter caused by the iron hydroxides.

### **3.4.3.2 Carbonates**

Miocene limestones appear in yellow/white on the inverted log residual images signifying TM7 absorption plus variable TM4 and TM1 absorption due to iron hydroxides and iron oxides respectively. The limestone beds are characterised by altered carbonate, shelly material and sand surfaces; the altered carbonate outcrop generally produces a diagnostic TM7 absorption on the ratio and log residuals images. Fresh limestones exposed in large quarries appear dark on the inverted log residuals image owing to high albedo and lack of absorption features. Limestones of the Middle Eocene Mokattam Formation are extensively quarried for the cement industry, whilst white Lower Miocene sandy limestones in the north east are worked for dimension stone.

### **3.4.3.3 Other lithologies and vegetation**

Basalt and dolerite sills and plugs of Oligocene age are common within the Oligocene sand and gravel formations. The weathered surfaces of these mafic rocks are encrusted with both iron minerals and a brown/red-coloured iddingsite - a hydroxyl derivative of olivine or pyroxene. This produces a strong TM7 absorption and gives them a distinctive red and crimson appearance on the inverted log residuals imagery (Figure 3.32). Outcrops, contiguous quarry workings and drainage traces are all highlighted. The hydroxyl-related absorption in TM7, and low albedo of the dolerite, give an equally strong dark brown-red colouration to these units on 1-5-7 FCCs; this readily distinguishes them from clay or carbonate TM7 features (Figure 3.33), which are a distinctive white colour in the 1-5-7 FCC image due to high albedo.

The Oligocene sand and gravel deposits of the Gebel Ahmar Formation are mantled by a veneer of desert-varnished chert gravel (Figure 3.34). Undisturbed surfaces are distinguished in the field by their iron oxide coatings; absorption of these oxides in TM1 gives a marked blue tone on 7-4-1 imagery (Figure 3.32). All freshly-disturbed ground, including pits and quarries, appear yellow-orange on the 7-4-1 log residuals data, ascribed to TM7 absorption from exposed clays underlying the surficial gravels mixed with TM4 absorption from iron hydroxide minerals. Old gravel spoil heaps have a mixed spectral response, combining typical iron oxide related TM1 absorption in blue and iron hydroxide TM4 absorption in green with absorption in TM7 caused by disturbed clay and gypsum; the latter is strongest along tracks leading away from the workings. These spoil heaps have a dark tone in 1-5-7 FCCs due to their low albedo.

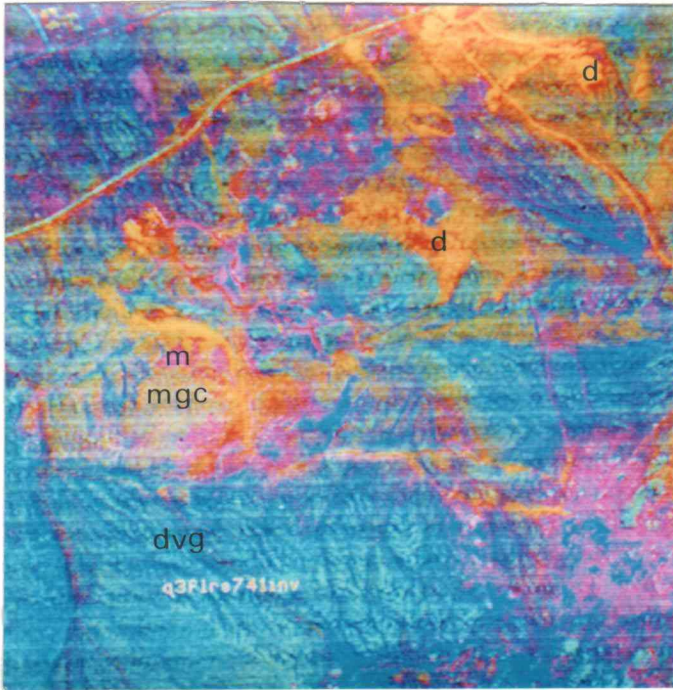


**Figure 3.32** Log residuals, bands 7 4 1, inverted (R G B), marly gypsiferous clays (mgc), desert-varnished surface gravel (dvg), dolerite quarries (d), Km 30 Cairo-Suez road.



**Figure 3.33** Colour composite, bands 1 5 7 (R G B), dolerite quarries (d), Km 34 Cairo-Suez road.



**Figure 3.34** Desert varnished surface quartz/chert gravel overlying the Anqabia sand/gravel Formation, Old Cairo-Suez road.

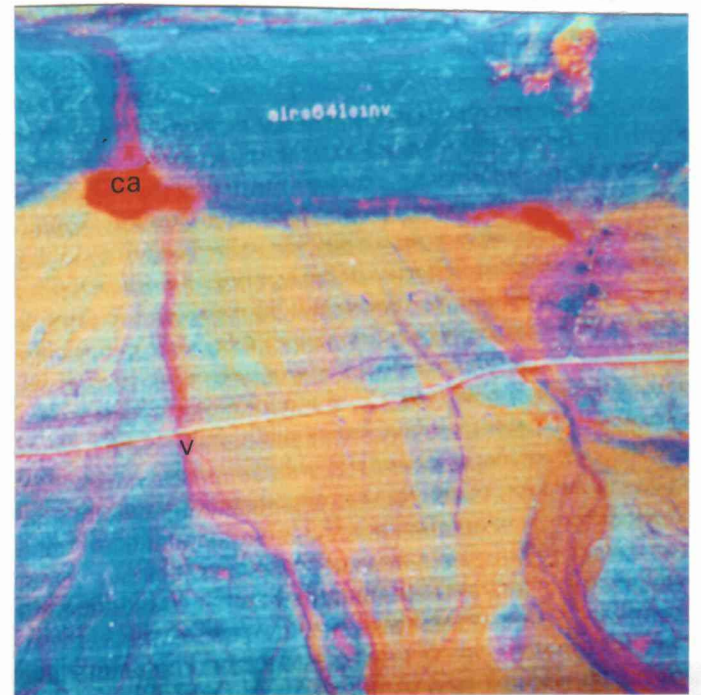


**Figure 3.35** Log residuals, bands 7 4 1, inverted (R G B). Drainage pattern with scrub vegetation (v) and silty clay alluvium (ca), Wadi El Gafra, Cairo-Suez road.

A surprising discovery was the abundance of low scrub vegetation in the predominantly north-draining wadis of this area. This together with concentrations of clay-rich sediment produces the characteristic TM7 signal. It can, however, be distinguished from other TM7 absorption by the geomorphic patterns of the wadi systems. Scrub vegetation along Wadi El Gafra is displayed as varying hues of red (clay dominant) and purple (vegetation dominant) on the log residuals 7-4-1 image shown in Figure 3.35. Note that clay beds exposed at the top of the image also display TM7 absorption; the clear outcrop form of these deposits allows them to be discriminated from the vegetation anomalies in the wadis.

#### **3.4.4 Spectral analysis**

Mixed-mineralogy surfaces, similar to those occurring at El Fayum, are common in the Cairo-Suez area. Again T-Spectra can be used to make general distinctions between lithologies such as dolerite and carbonate. Many of the sedimentary lithologies, however, have an intimate mixture of clay, carbonate and sulphate minerals in their weathered surfaces which makes spectral analysis particularly challenging.

Despite these mixing problems, interesting information can be extracted from the log residuals data. Figures 3.36 and 3.37 show TM pseudospectra from two sedimentary units which are each mantled by gypsum, calcite, quartz and clay debris and which appear similar in the field. The pseudospectrum of the first unit (Figure 3.36) is similar to the Sinai gypsum pseudospectrum, whereas the other (Figure 3.37) displays no clear gypsum features but only a general TM7 absorption. Although gypsum is present in both lithologies, its concentration is much lower in the second unit, which is more clay and carbonate rich.

Figure 3.38 shows the pseudospectrum typical of the Oligocene sand and gravel deposits of the Gebel Ahmar Formation. These aggregate resources are mantled by an extensive veneer of desert-varnished chert gravel rich in iron oxides, which accounts for the strong TM1 absorption in their pseudospectra (compare with the laboratory spectra of hematite and goethite resampled to TM wavelengths seen in Figure 2.9).

In the few areas where it occurs, vegetation has clear characteristics which enable it to be distinguished using T-Spectra. Figure 3.39 shows one such pseudospectrum from a wadi. The major features characteristic of vegetation are the dual reflectance peaks in TM2 and TM4.

#### **3.4.5 Laboratory results**

XRD analysis was carried out on 18 assorted samples from the Cairo-Suez study site in the Mineralogy and Geochemistry department of EGSMA (El-Saiy and Salama, 1993). A Phillips XRD system model PW/1710 was used with Cu-radiation of  $\lambda = 1.542\text{\AA}$  at 40 KV, 30 MA and a Ni filter, running a scanning speed of  $1.2^\circ 2\theta/\text{minute}$ . Reflection peaks between  $2\theta = 2^\circ$  and  $60^\circ$  were obtained. The corresponding spacing ( $d$ ,  $\text{\AA}$ ) and relative intensities ( $I/I^\circ$ ) were obtained and compared to the standard A.S.T.M cards.

The samples fall into two categories: (1) fresh clays and (2) surficial mixed clay, carbonate sand and gravel. The XRD results demonstrate differences in mineralogy as shown in Table 3.2.

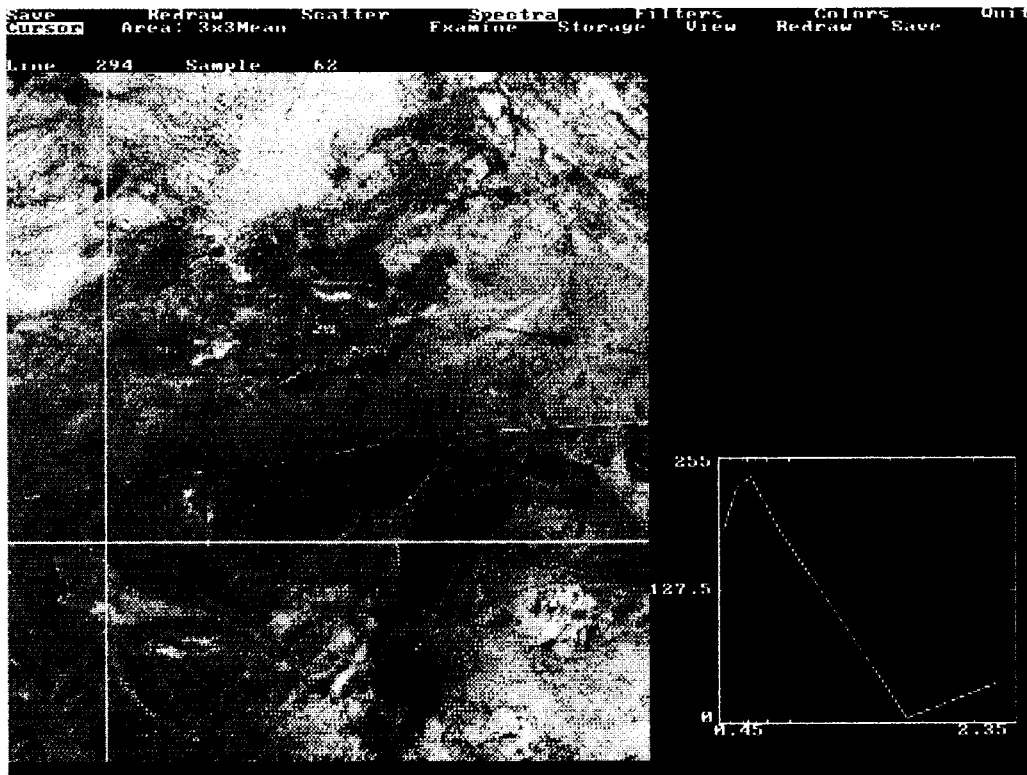


Figure 3.36 T-Spectral analysis gypsiferous clay and marl beds, Qattamia highway, Cairo-Suez.

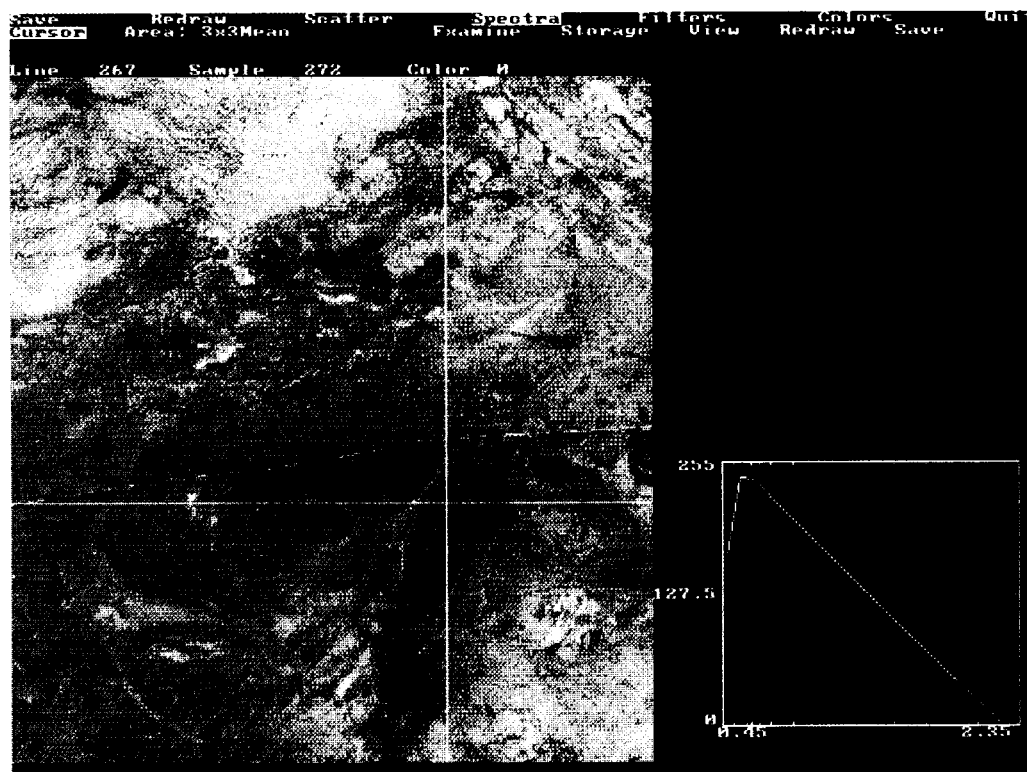


Figure 3.37 T-Spectral analysis, calcareous surface gravel, Qattamia highway, Cairo-Suez.

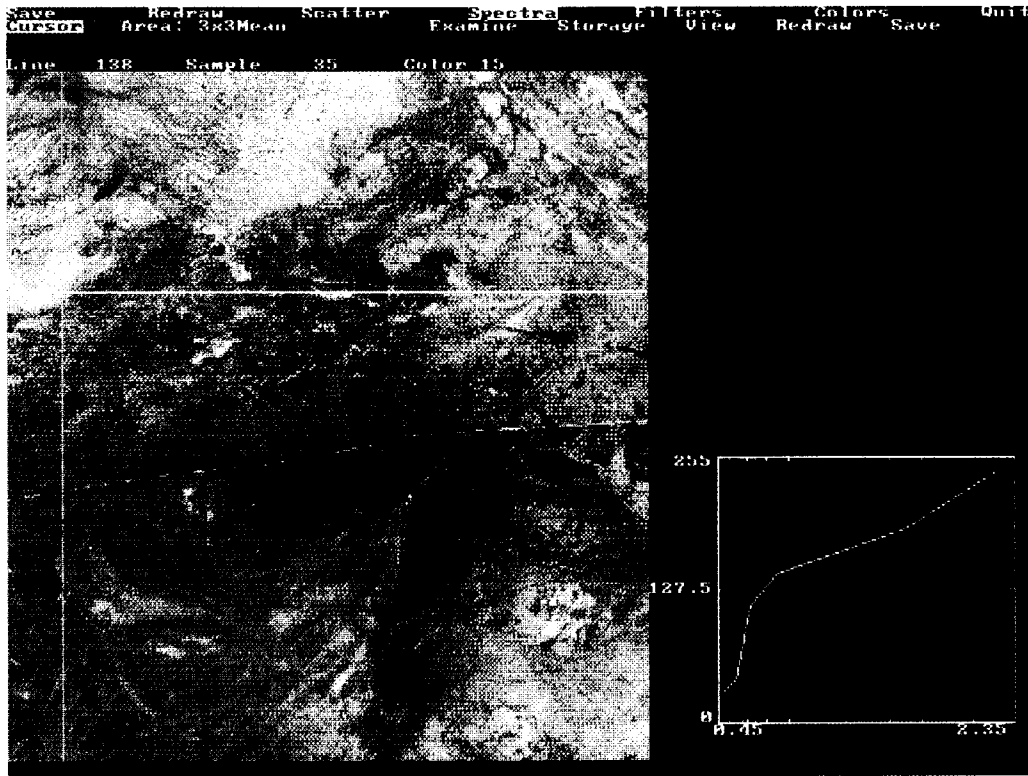


Figure 3.38 T-Spectral analysis, iron oxide-coated cherty gravel near Qattamia highway, Cairo-Suez.

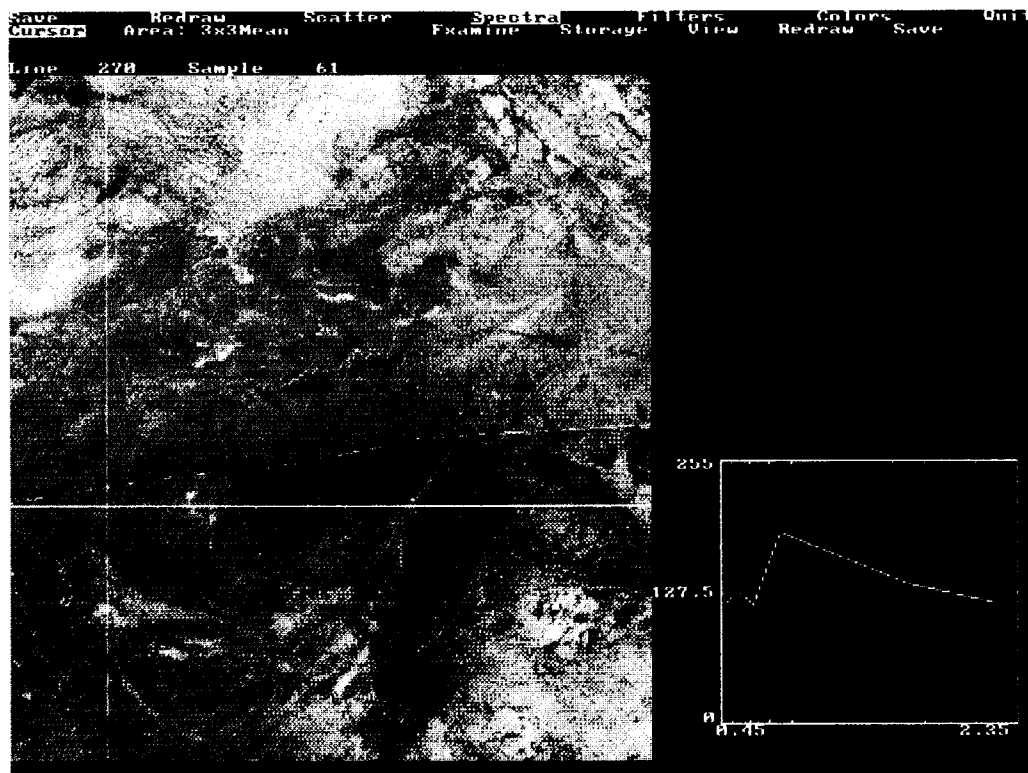


Figure 3.39 T-Spectral analysis, vegetation in wadi near Qattamia highway, Cairo-Suez.

Table 3.2: Summary of XRD analyses from the Cairo-Suez area

Sample type	XRD mineral determinations (in decreasing abundance)
Fresh clay or shale from pit or outcrop	Quartz, montmorillonite, halite, kaolinite, calcite. Trace illite
Surficial clayey, marly, carbonate shell sand/gravel	Calcite, gypsum, quartz. Trace montmorillonite

The XRD analyses generally support the field observations. Most of the green-buff clays and shales of the Maadi and Anqabia Formations are composed of montmorillonitic (bentonitic) members of the clay family. Halite, commonly reported in the results, is probably a by-product of alteration or weathering. The mineral identifications in the surficial material are probably more significant from the standpoint of remote sensing; the carbonate shell sand/gravel is the dominant surface material on all the clay/marl outcrops and has the strongest influence on the TM data. The inference from the XRD data is that calcite and possibly gypsum debris in the surficial gravels of the clay/marl sequences are the main sources of TM7 absorption. In areas of moderate relief where clay and marl beds are exposed, the absorption features of TM7 for calcite and gypsum, and TM7 and TM4 for marl and limestone beds, produce distinctive red, pink and yellow tones in the log residuals 7-4-1 image (Figures 3.32 and 3.35).

### 3.4.6 Summary of Cairo-Suez results and conclusions

General conclusions from the Cairo-Suez area are:

1. Like El Fayum, this area also shows mixed TM7 responses which makes precise mineral identification difficult. Here again, spectral analysis of log residuals pseudospectra complements, rather than replaces, conventional image interpretation.
2. Logarithmic residuals and band ratio FCC images proved to be the most useful for mapping occurrences of clay-carbonate on clay/marl units, iron oxide coatings on sand/gravel units and hydrated magnesian minerals associated with mafic intrusions. Topographic features and outcrop patterns again helped the discrimination of lithologies.

### 3.5 General conclusions: arid areas

The work carried out in Egypt has shown that Landsat TM imagery can be successfully used in a well-exposed arid region to discriminate, and in some cases provisionally identify, rocks and minerals of industrial significance. The methods worked better in the Sinai region than in El Fayum or Cairo-Suez probably because: (1) the region is less disturbed by development, (2) fewer mixed-composition surfaces with a TM7 absorption occur, and (3) the tectonic style and greater relief result in the better exposure of lithologies.

Conventional image processing and interpretation can serve to highlight areas of TM7 absorption caused by minerals such as gypsum or kaolinite. False colour band composites and ratio composites provide basic discrimination, but the logarithmic residuals images are overall the most useful for mapping spectral responses in reflectance-related terms. However, 'false anomalies', associated with lithologies having no economic interest such as kaolinitic sandstone or weathered/altered dolerite, occur with all image types. Some separation of materials is often possible based on differences in albedo, absorptions in other TM bands, outcrop pattern and prior field knowledge. The main difficulty is in recognizing and interpreting mixed lithologies comprising several materials that cause TM7 absorption (such as mixed clay, sulphate and limestone materials).

A new approach developed during this project involves the spectral interrogation of the logarithmic residuals TM data using a program called T-Spectra. This software can be implemented on any PC running DOS and is therefore potentially field-portable. In this spectral approach, less reliance is placed on the subjective interpretation of image colours and more on the semi-quantitative examination of image pseudospectra. Individual locations in the image can be examined and comparisons made with both known sites and other responses in the image. This makes possible the separation and recognition of lithologies based not only on their TM7 response but on overall differences in the shape of their TM pseudospectra.

In this study, little use was made of library mineral spectra resampled to TM wavelengths. Potentially, such data could be compared with the TM pseudospectra to allow direct interpretation of TM imagery in gross mineralogical terms. In its present implementation, however, the log residuals transform shows significant differences in the shape of the resulting pseudospectra which preclude such comparisons. (However, despite this, the pseudospectra within an individual log residuals image are internally consistent). More precise atmospheric correction of TM data, and a revised implementation of the log residuals transform which better meets the assumptions behind the equations, are needed before this approach can be properly tested.

## 4. SEMI-ARID TEST SITE: NAMIBIA

*Synopsis: A detailed account is given of attempts to apply the techniques developed in Egypt to more difficult, vegetated, semi-arid terrain in Namibia. It provides a full description of the study sites, image processing and interpretation, field evaluations and laboratory analyses. In common with Chapter 3, it is intended primarily for the specialist remote sensing geologist.*

### 4.1 Introduction

Namibia was chosen as a second test area since (1) it provides suitable example of a semi-arid environment in which to test the techniques developed in Egypt, and (2) clays for local brick-making are of very limited occurrence in the country. The presence of increased vegetation can be expected to cause complications as a result of both its spectral response and the masking effect it has on the ground surface. A publication by the Geological Survey (Schneider and Diehl, 1991) describes the known deposits of clays and other industrial minerals in the country, and this provided a basis for selecting study sites.

The climatic regions of Namibia, classified according to the Köppen system, are given in the National Atlas of South West Africa (Namibia) (Van der Merwe, 1983). The north and north east of Namibia are classified under the coding BShgw. This indicates a dry region with a deficiency in rainfall (B); semi-desert or steppe (S); an annual mean temperature above 18°C (h); a monthly maximum temperature in the early summer (g); and rainfall during the summer (w). Most of the region to the north and east of the capital Windhoek, is classified as BShw: i.e. as above but with no early summer monthly temperature maximum. The area immediately to the east and south east around Windhoek is classified as BSkw indicating a cool semi-desert area with an annual mean temperature below 18°C (k).

Two study areas were investigated. The first was located along the southern bank of the Okavango River, which forms Namibia's northern border with Angola (Figure 4.1). In this area, more than 90% of the annual rainfall (500-600 mm at Rundu) occurs between October and March. Away from the river flood-plains, the natural vegetation in the northern study area is forest savanna and woodland.

The second area lies to the east of Windhoek on the margins of the Kalahari Desert. The natural vegetation in the Windhoek area is typically highland savanna, passing eastwards into camelthorn savanna. Here, the annual average rainfall varies from 200 to 400 mm, with 80-90% occurring between October and March.

### 4.2 Okavango River Area

#### 4.2.1 Geological setting

The plateau through which the Okavango River cuts consists of Tertiary to Quaternary deposits, including Kalahari Sands between 120 m and 130 m thick (Geological Survey of Namibia, 1980). In contrast to Sinai, the Okavango clay deposits are of modern origin and

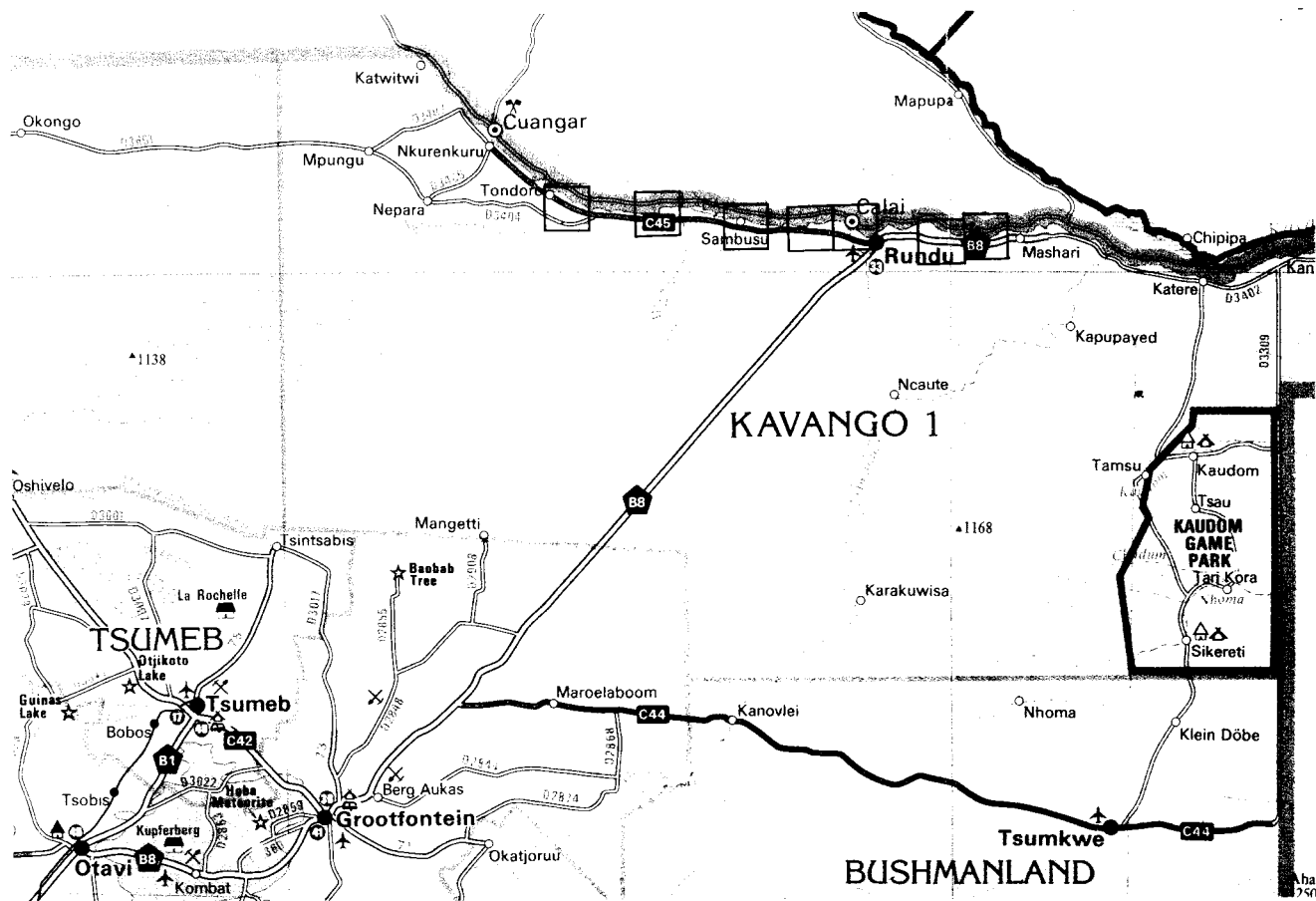


**Figure 4.1** Location of the study area in north east Namibia, showing the seven areas chosen for field checking.

do not occur within a well-defined stratigraphic sequence. They are more variable in distribution and composition, and consideration needs to be given more to the physiographic controls that govern their development than to geological setting.

The Okavango is a mature, meandering river which flows southeastward into the interior of the African continent and discharges into the Okavango Delta in northwestern Botswana. The river transports coarse and fine-grained sands, silts and clays, depositing these materials across a complex braided meander system during an annual inundation of its flood plain. Schneider and Diehl (1991), referring to earlier work by Schreuder (1980), describe sporadic occurrences of clay along the whole length of the flood plain. Typical clay deposits vary in thickness from 0.5 to 1.0 m, have surface areas of 0.42 km<sup>2</sup> to 2.7 km<sup>2</sup> and consist of kaolinite, montmorillonite, minor illite, 18% to 26% quartz, and occasional trace feldspar.

The thickest clay deposits accumulate within abandoned channels and oxbow lakes, which are often rich in organic material produced from the decay of vegetation. Clays are also deposited in the uppermost part of point bars, forming thin irregular sub-horizontal sheets. Point bar successions consist of sandy or silty ridges and clay-filled hollows, formed of repeated lateral accretion sets during meander migration. During times of rising flood, the hollows may become enlarged and form chutes. The chutes in turn become narrow elongate lakes as the flood wanes, and can also become infilled with clay. Finally, clays are found away from the braided channels as extensive thin mudsheets covering the main flood plain.

Thus, a variety of clay deposits occurs along the Okavango River margins. Locating the most extensive of these requires the meander system to be mapped in some detail and its development understood. Remote sensing can potentially provide information about the surface extent of deposits but not about their thickness or compositional variability in depth. Of particular importance from a remote sensing viewpoint is the presence of vegetation. Although northern Namibia is generally semi-arid, regular inundation along the Okavango River margins results in a complex and variable vegetation pattern that is atypical of this climatic setting. Because of this, the Okavango proved to be less than representative of semi-arid areas in general.

#### **4.2.2 Data processing**

##### **4.2.2.1 Conventional image analysis**

A moveable Landsat TM scene, path 177 row 072-073, acquired 23 June 1984, covers this region. The June acquisition date in the middle of the dry season time represents a midway stage in the flood plain drying-out process. Atmospheric correction used a variant of the dark object subtraction method. Due to the absence of deep, dark still water with a presumed DN value of zero in all TM bands, a value of 1 was assumed. Statistics were collected from a mask using TM7 with a DN range of 0 to 3, over a large relict meander bend and an ox-bow lake from a small sub-scene near Sinsogoro. The atmospheric scattering component for each wavelength band was estimated by subtracting from each band their mode minus 1. Any negative values were set to a value of 1.

The subsequent processing was similar to that used in Sinai (section 3.2.2):

1. Ratio FCC: 7/5, 4/3, 5/1 (RGB). This image was not found to be very informative within the river flood-plain probably due to the masking effects of vegetation and reeds.
2. Principal components: The combination PC 4-2-5 was found to show the best overall discrimination, although PC 3-2-1 was also found useful.
3. Log residuals: Inverted logarithmic residuals 7-4-1 images for selected sub-areas of interest.

Computer screen photographs were taken of various images, and prints at approximately 1:75 000 scale used during fieldwork for ground truthing. A comparison of the different Landsat TM imagery products for the Sambusu sub-area is shown in Figure 4.2A-D.

#### 4.2.2.2 Integration of satellite imagery and aerial photography

The spectral range covered by multispectral imagery such as Landsat TM is an obvious advantage in discriminating ground materials. However, in complex environments such as the Okavango flood plain, where the occurrence of materials of interest (here clays) is intimately linked to modern day processes, the poor spatial resolution of the TM (30 m) is a major limitation. On the other hand, the high spatial resolution, and stereoscopy, of conventional black-and-white aerial photography provides much information on the geomorphology. In order to combine these benefits, an experiment was carried out to digitally merge the two data types. One of the more discriminating false colour sub-scenes, the PC 4-2-5 image, was selected covering the Sambusu area and integrated with a black-and-white 1:50 000 scale aerial photograph (No. 692/3811 dated 21 July 1971) for the same area.

Digital merging involved the following processing steps:

- (1) The aerial photograph was scanned at an appropriate resolution (254 dpi or 100  $\mu\text{m}$ ) to convert it to a digital image.
- (2) The satellite image was resampled to the same spatial resolution as the photograph (5 m at the scanned resolution of 254 dpi).
- (3) The scanned photograph was digitally warped to the TM image using a series of common control points and cubic convolution. (NB It is also possible to warp the TM image to the geometry of the aerial photograph, thus retaining the relief-related distortions that produce parallax, and thus potentially provide stereoscopy, if both photographs of a stereo pair are used).
- (4) The RGB principal components image was transformed to intensity-saturation-hue colour space, the intensity component was replaced by the single band aerial photographic image, and the new image was converted back into RGB colour space.

A part of the merged image is shown in Figure 4.3.

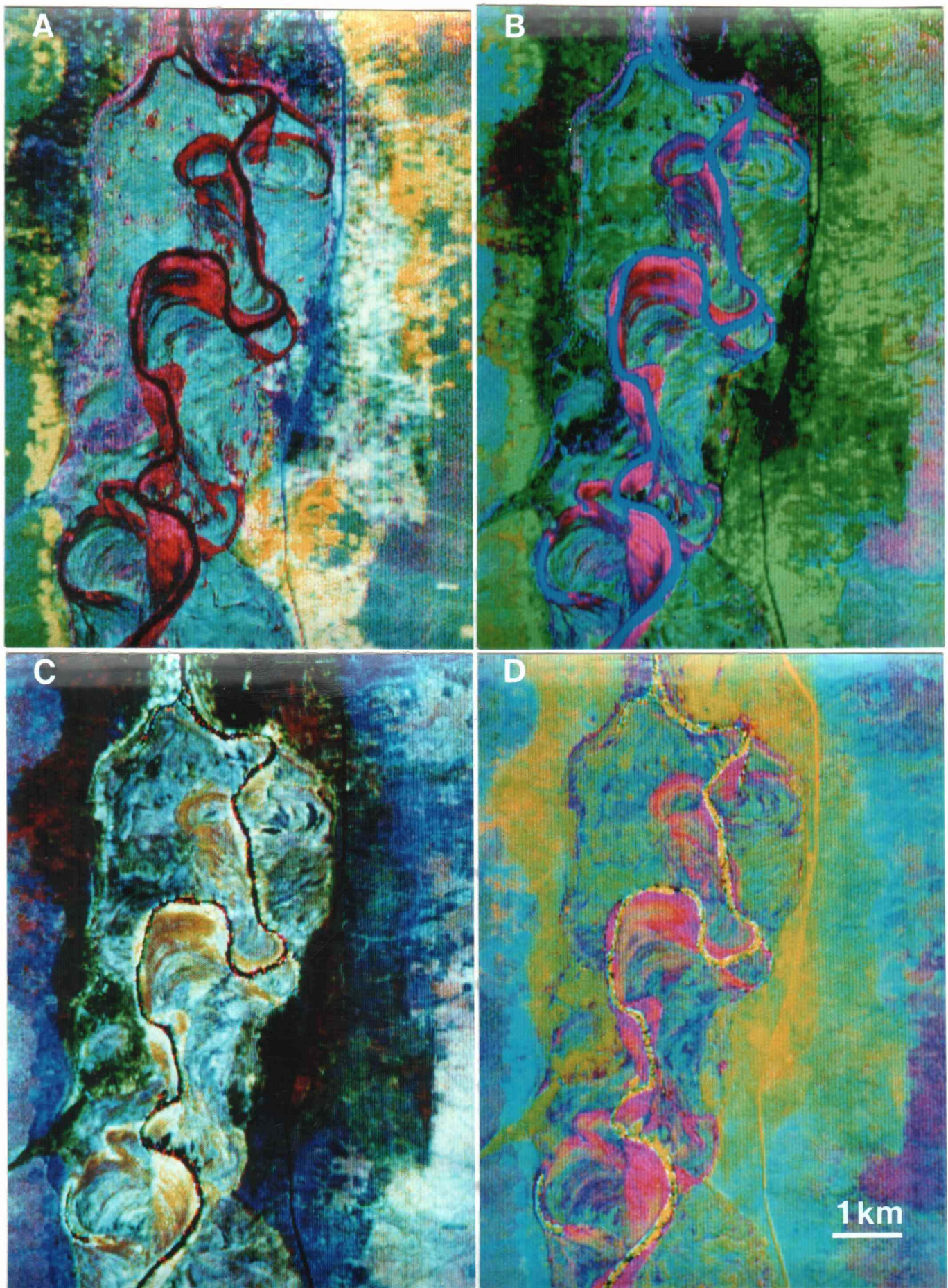


**Figure 4.2** Comparison of image-processing methods for the flood-plain at Sambusu Mission (A) PC 4-2-5; (B) PC 3-2-1; (C) Ratios 5/7-4/3-5/1; (D) Inverted log residuals 7-4-1.

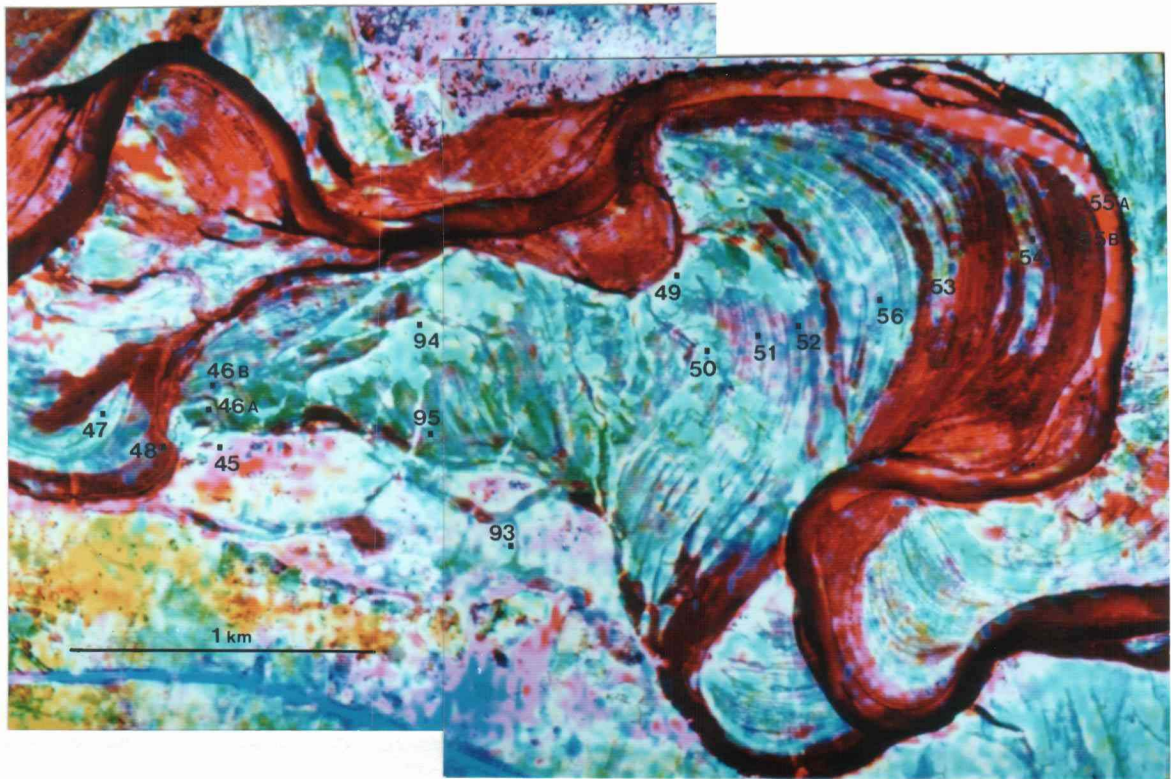


**Figure 4.3** PC 4-2-5 enhanced Landsat image merged with an aerial photograph of the Sambusu region, showing sample localities of specimens collected for XRD and spectral analysis. Scale approximately 1:25 000.

### 4.2.3 Evaluation and field correlation

Fieldwork was undertaken (August 1992) along a 145 km section bordering the Okavango River from approximately 105 km west of Rundu to 40 km east. The main objective was to establish ground, soil and vegetation correlations with the 1:75 000 Landsat images and 1:50 000 aerial photographs. The ground reconnaissance was concentrated mainly along the river flood-plain and older, higher terraces. Seven sub-areas were examined in the field (Figure 4.1), five of which had been previously identified as clay deposits by Schreuder (1980), and tabulated in Table 4.1.

Table 4.1 List of potential clay deposits along the Okavango River (Schreuder, 1980)

Locality	Code	Deposit size	Estimated tonnage	Field-check	Map
Tondoro	A	750000 m <sup>2</sup> x 1.0 m	1350000	Yes	Tondoro
Rupara	B	675000 m <sup>2</sup> x 0.5 m	607500	Yes	Rupara
Sambusu	C	1325000 m <sup>2</sup> x 1.0 m	2385000	Yes	Sambusu
Halili	D	425000 m <sup>2</sup> x 0.1 m	765000	No	Sambusu
Sinsogoro	E	2050000 m <sup>2</sup> x 0.8 m	2952000	No	Mupini
Ebenezer	F	875000 m <sup>2</sup> x 0.75 m	1181250	Yes	Mupini
Nakazaza	G	2700000 m <sup>2</sup> x 1.0 m	4860000	Yes	Mupini

The two additional localities were field-checked. The first was located from 18 to 23 km east of Rundu on the Rundu 1:50 000 sheet (Figure A1.6), and the second from 1 to 5 km east of Shambyu on the Mashari 1:50 000 sheet (Figure A1.7).

A total of 59 clay-rich samples were collected for XRD analysis, including some from the deposits identified by Schreuder (1980). Three samples were also collected from the Otavi Brickworks, approximately 325 km to the south west of Rundu (the nearest commercial brickworks to the Okavango River area). The samples were analysed by Dr G. Schneider of the Namibia Geological Survey. A total of 108 samples were also collected for laboratory spectral measurement in BGS (Marsh and Tragheim, 1995). Maps showing field and sample localities are provided in Figures A1.1 to A1.7 in the appendix.

In the following sections the Sambusu locality is described in detail as it demonstrates the main characteristics found all along the Okavango River flood-plain. Other localities are discussed only where they illustrate additional features.

#### 4.2.3.1 Vegetation

The vegetation in the Okavango River flood-plain varies in relation to the time of season, topography, proximity to water, and soil type. These are all intimately related to the dynamic, sedimentological and geomorphological evolution of the river meander system.

Lush reeds grow at times of flooding but diminish in extent through the rest of the year as the flood waters recede. Thus, depending on the season, different zones within the flood plain are covered by different types and amounts of living and dead vegetation. At the time of acquisition of the Landsat image (23 June 1984) and the aerial photographs (21 July 1971), the flood-plain was about halfway through its drying-out process following the main October-March rains. At this time of year, the region experiences its lowest average monthly temperature (16°C) and its longest daily sunshine (10 hours).

In low lying areas, near the main river or in flooded relict meander bends or oxbows, there is generally an abundant covering of healthy growing reeds. These appear in reddish or magenta hues on the PC 4-2-5 image (Figure 4.2A), and in red to violet on the 7-4-1 (Figure 4.2D) inverted log residuals image. Occasional large trees near the river's edge and on raised sandy overbank deposits may also contribute to the vegetation signal. Figures 4.4 and 4.5 show the type and variations of vegetational growth on the Okavango River flood-plain to the west of Rundu.

Elsewhere, large trees and scrub thorn bushes grow on slightly higher and older sandy terrace deposits and are easily recognised by their violet/magenta to purplish colours on the PC 4-2-5 image. Figure 4.6 shows one such site at Tondoro (locality 12). The clay filled depressions behind these upper terraces tend to be devoid of vegetation, apart from a very sparse covering of grass (Figure 4.7).

On the main arcuate, meander scroll deposits, there is an abundant mixed covering of flattened dried reeds, and upstanding clumpy, straw-yellow reeds. Figures 4.8 to 4.11 from the Sambusu region show the variations which occur. The reeds are sometimes less extensive on the mud-flats near the main back-terrace edge of the flood-plain e.g. east of Rundu, near Shambyu (Figure 4.12). As before, red colours predominate on the PC 4-2-5 image.

#### **4.2.3.2 Clays**

Despite the relative abundance of clay on the flood-plain, little apparent use is made of it locally for building. An exception was seen at Shambyu (Figure 4.13), where it was used to infill the walls of a hut. Most of the dwellings away from Rundu are made of wood and reeds. There appears to be no local brick-making industry.

Field observations provided an explanation for many of the features seen on the aerial photographs and enhanced TM imagery. Unlike Sinai, the best discrimination between surface materials was found in the principal components images rather than the log residuals or ratio images.

Table 4.2 lists the weightings of the original bands in each of the principal components.

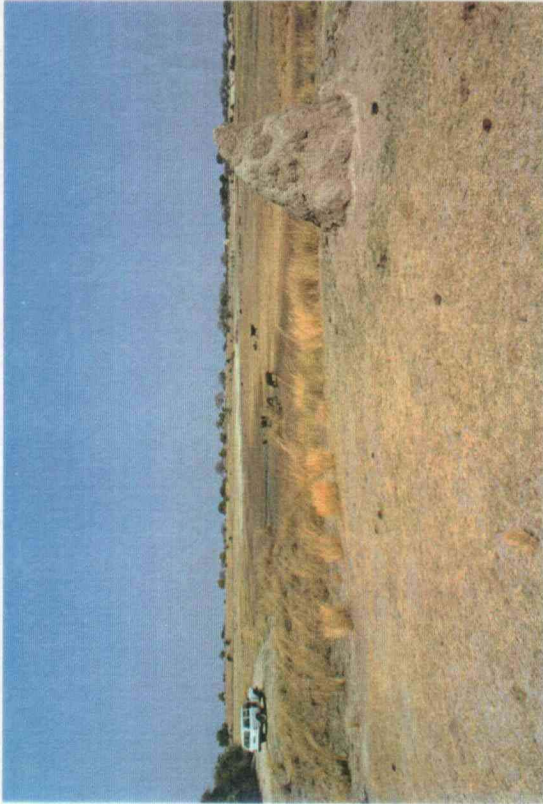


**Figure 4.8** View looking SW of a clay-rich old meander bend in the Sambusu area (locality 48). The foreground consists of overbank sands and silts with a thin covering of grass and scattered reeds.

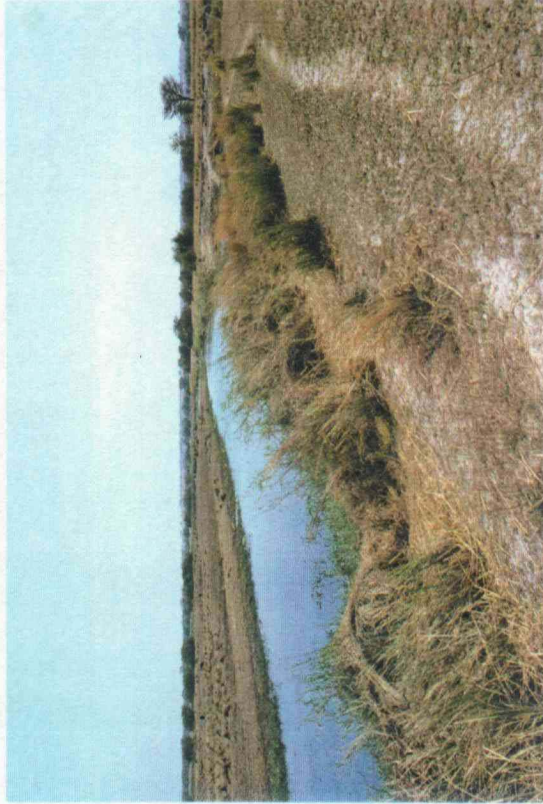


**Figure 4.9** View looking NE of a flooded meander bend rimmed with healthy reeds in the Sambusu area (locality 49). The low-lying, reed covered ground overlies a clay deposit (Schreuder 1980, locality C).



**Figure 4.10** View looking north of a waterlogged, clay-rich, depression of the lateral accretion sets in the Sambusu region (locality 52).



**Figure 4.11** Typical appearance of clumpy reeds and green grasses growing in a clay-rich depression of the lateral accretion sets in the Sambusu region (locality 54).

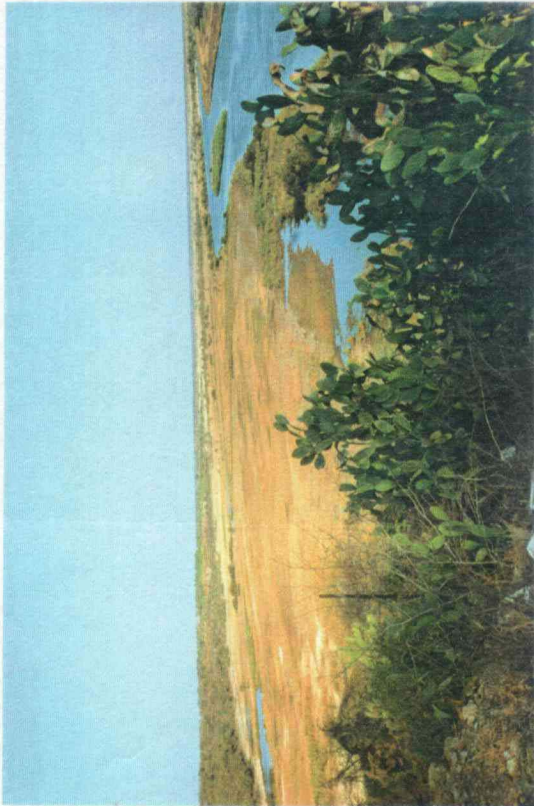


**Figure 4.4** View of Okavango River flood-plain looking west from Kavango Lodge, Rundu.

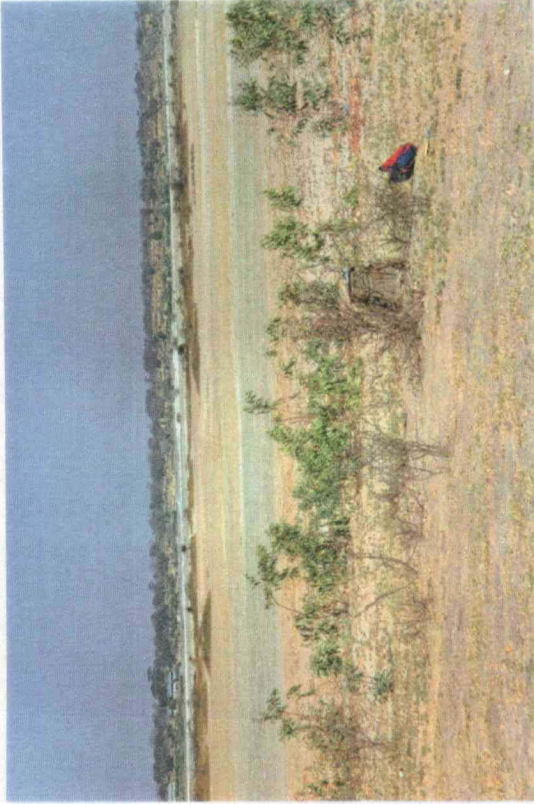


**Figure 4.5** View of west Rundu flood-plain showing vegetated sandy rises and darker coloured clay flats.

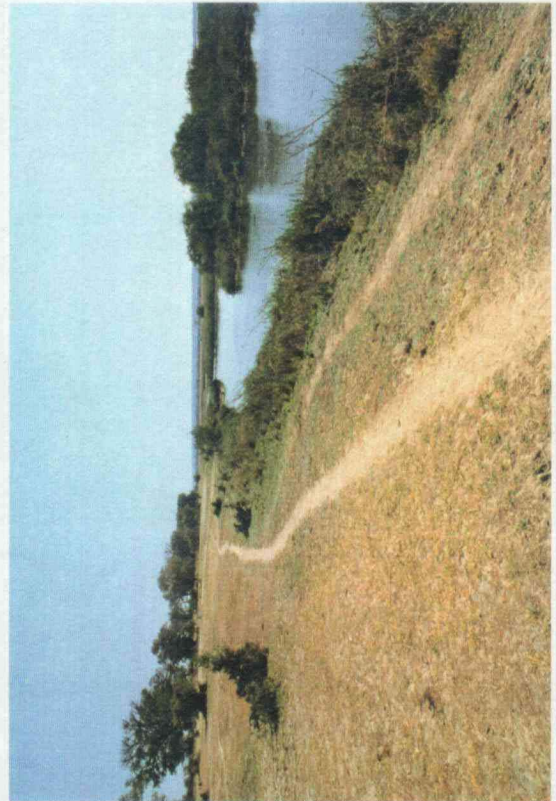


**Figure 4.6** Different types of vegetation are related to compositional and topographic variations in the flood-plain terraces near Tondoro (locality 12).

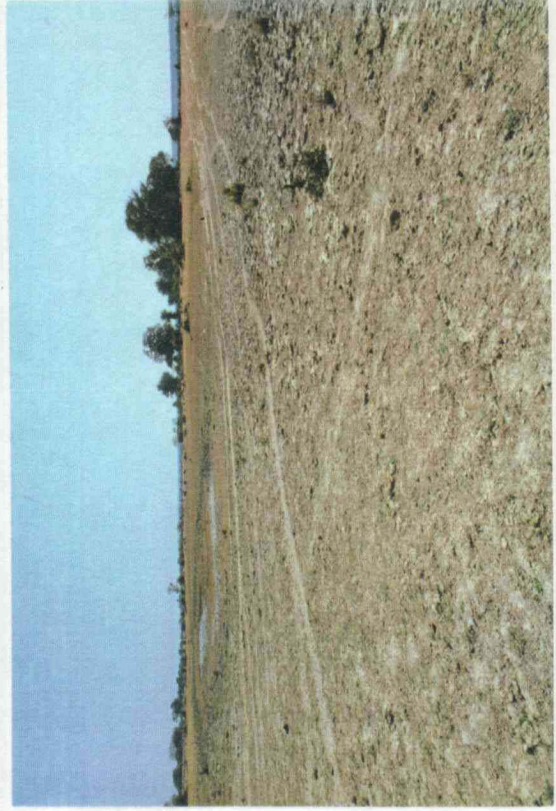


**Figure 4.7** Typical appearance of a clay-rich arcuate depression, which occurs on the landward side of the sandy ridge shown in Figure 4.6 near Tondoro (locality 18).



**Figure 4.12** Less extensive reed growth overlying clays near the main back-terrace edge of the Okavango River flood-plain, 5 km east of Shambyu (locality 72).

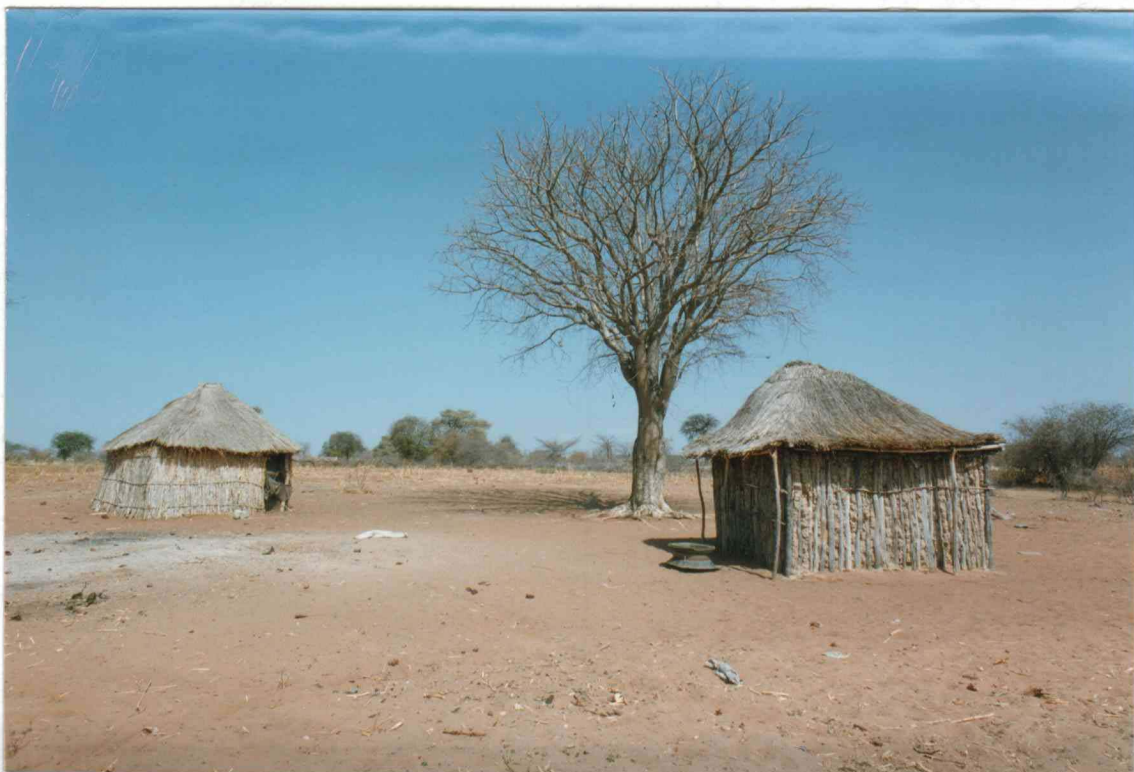


**Figure 4.13** Example of local clays used for building materials in the walls of a hut, 1.5 km east of Shambyu (locality 63). The foreground consists of orange/brown limonitic sands, which occur above the flood plain.

Table 4.2 Eigenvalues and eigenvectors for the principal components analysis of the Okavango sub-scenes

Principal components	Eigenvalues	Eigenvectors					
		TM1	TM2	TM3	TM4	TM5	TM7
PC1	0.906	-0.235	-0.165	-0.290	-0.326	-0.736	-0.431
PC2	0.052	-0.579	-0.336	-0.343	-0.422	0.464	0.200
PC3	0.029	-0.361	-0.201	-0.127	0.723	0.187	-0.506
PC4	0.008	-0.221	-0.034	-0.283	0.436	-0.419	0.710
PC5	0.005	0.621	-0.202	-0.740	0.048	0.148	-0.053
PC6	0.001	-0.213	0.882	-0.394	-0.030	0.100	-0.105

Principal components are, as always, difficult to interpret in physical (spectral) terms. Generally speaking, a high eigenvector value indicates a strong contribution from that band; positive and negative eigenvectors in the same component represent contrasts. PC1 accounts for 90% of the variance and describes the albedo. PC4, although it only accounts for 0.8% of the variance, has high positive eigenvector loadings for TM7 and TM4, and moderate loadings for TM5 and TM3: it probably relates to both vegetation and clays.

Field checking provided an empirical explanation of the ground conditions represented by different colours in the PC and other FCC images shown in Figure 4.2A-D. These field correlations are summarised in Table 4.3. Low lying areas near the river, consisting mainly of clays with an abundant covering of reeds, appear reddish in the PC 4-2-5 image (Figure 4.2A). Elsewhere, the clays within the shallow topographic depressions of the laterally accreted meander scroll deposits tend to appear blue, dark blue or cyan. Silty or sandy clays tend to appear greenish cyan. All of the clays are variably covered with living and dried flattened reeds. It was also observed that the flattened reeds sometimes had a thin coating of clay, probably as the result of a recent flooding event.

A detailed aerial photograph interpretation of the Sambusu region, carried out in conjunction with the enhanced Landsat imagery, is shown in Figure 4.14. This provides a graphic illustration of the evolution of the meander system in this part of the river. The thickest clay deposits are likely to be found in the low-lying relict meander bends. However, extracting these clays presents a somewhat difficult problem due to the high risk of regular flooding.

The above interpretation (Figure 4.14) illustrates the individual advantages and limitations of aerial photographs and satellite images. The merged aerial photograph/PC 4-2-5 image (Figure 4.3), which combines the spatial resolution of the former with the spectral discrimination of the latter, greatly assists in deciphering the complex sedimentological and geomorphological history of the meander systems and deposits. On this, the darker bluish cyan and greenish cyan colours of the PC 4-2-5 image correlate with the clays occurring in the striped and arcuate depressions of the lateral accretion sets.

Table 4.3 Summary of image and ground correlations for clay-rich areas from the Okavango River flood-plain.

		Air photograph characteristics	PC's 4-2-5	PC's 3-2-1	Ratios 5/7-4/3-5/1	Log Residual 7-4-1	Ground Correlations	Sample Sites
<b>C</b>	<b>L</b>	(1) Streaky textured mid-grey tones, and both continuous pale and medium grey areas on lower terraces. Topographically low areas often including old meanders and ox-bow "lakes", which bound areas between them and the present river.	red to fuchsia	fuchsia pink	white (± yellowish tones)	magenta/violet	Areas of thick vegetation, usually tall reeds, some trees, in areas of low ground which are flooded for considerable periods each year. The image tones mostly correspond to the vegetation content, since the clays are seldom exposed.	53, 55b
			(2a) Mid grey tones, smooth, untextured ground.	dark blue/cyan	-----	reddish/mauve mottled (+ white)	-----	Clay areas covered by 100% long grass which is straw coloured in August.
<b>A</b>	<b>Y</b>	(2b) Streaky mid grey, crescent shaped depressions.	blue	red	pale lilac/brown	pale yellow/buff	Clay rich areas in depressions of meander lateral accretion sets, with clumpy reeds.	52, 54
		(3a) Smooth, dark grey tones, sometimes alternating with medium/light grey tones.	pale cyan	greenish cyan	mottled dark/pale blue and white	mottled bluish cyan	Clay and sand. In general, low relief, low-lying areas composed of low rises and depressions. Clay-rich in hollows, and sand/silt on highs. Moderate vegetation cover of reeds.	39, 46, 47, 56
<b>S</b>		(3b) Smooth lenticular, dark grey tones.	greenish cyan	bluish cyan	pale blue & white	mottled bluish cyan/purple		95
		(4a) Very dark grey tones in old meanders.	blue	-----	mottled greenish brown	-----	Clay in wet, annually flooded depressions. Associated with thin grassy vegetation. Moderate ground exposure over dried-up pools, surrounded by green grass.	43
		(4b) Streaky mid/dark grey tones in old meanders.	red (especially when covered by vegetation)	dark blue & violet	white	medium violet		48

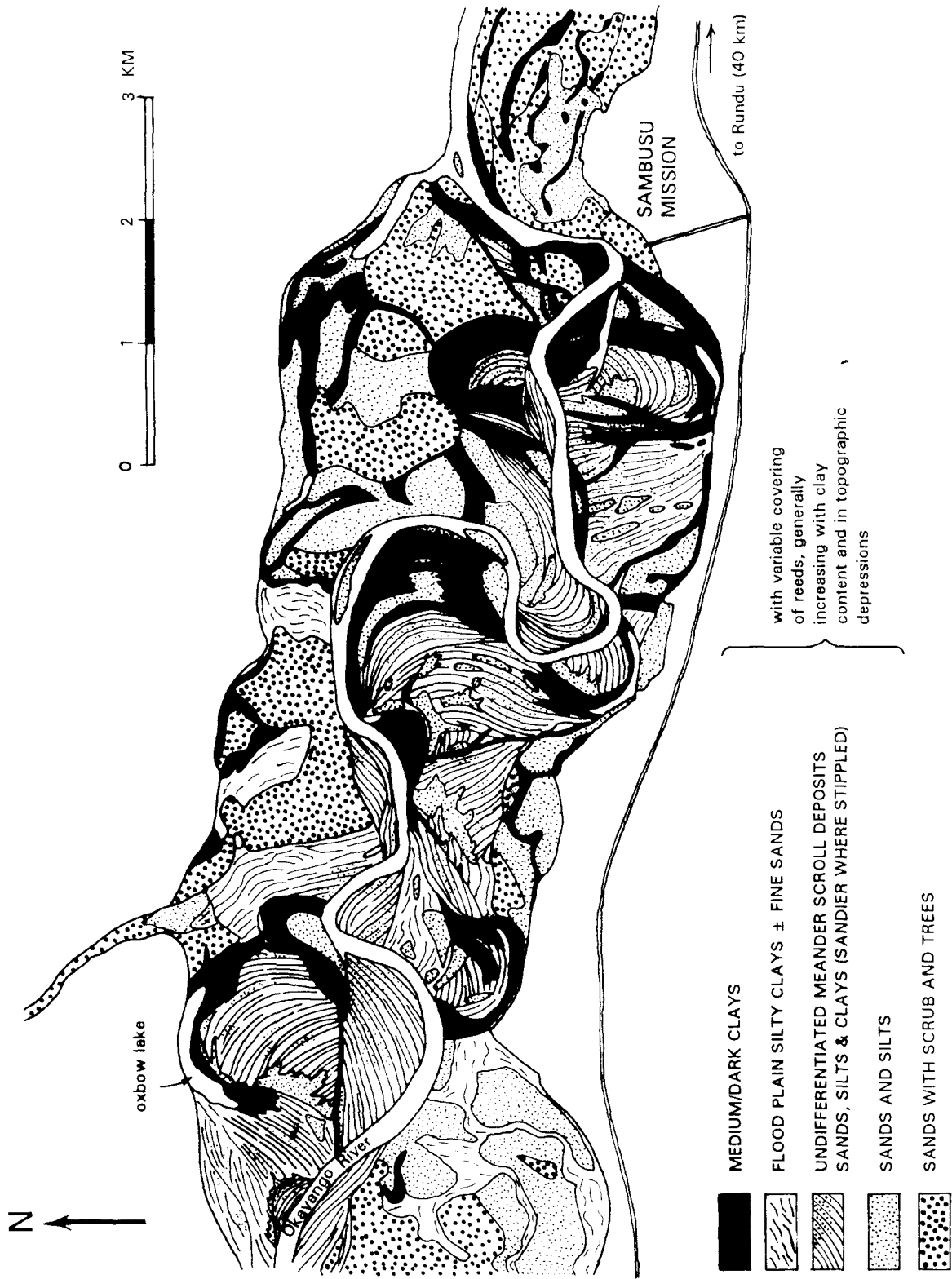


Figure 4.14 Detailed interpretation of stereo aerial photographs of the Okavango River floodplain at Sambusu, aided by field observations and the enhanced Landsat images shown in Figure 4.2A-D.

The XRD results of clays from this and other areas along the Okavango River flood-plain are summarised in Table A1.1 in the appendix. XRD analyses provide, at best, semi-quantitative data but indicate that 59% (32 samples) are clayey sands; 15% (8 samples) are clayey silts; 24% (14 samples) are silty or sandy clays; and only 2% (1 sample) was kaolinite dominant. From west to east, the samples from Tondoro, Rupara, Sambusu and Mupini generally had kaolinite present together with trace amounts of montmorillonite. The specimens from Sambusu were mostly silty clays with approximately equal amounts of kaolinite and quartz. The Rundu samples showed minor montmorillonite but no kaolinite. Further east, the samples from Mashari had a variable montmorillonite content generally exceeding kaolinite, if present at all.

Figure 4.15 shows IRIS spectral measurements for the silty clays from the Sambusu region; their locations are plotted on Figure 4.3. These spectra show an apparent systematic variation with location on the flood-plain; this may be described according to three groups of samples.

The first group, consisting of samples 46a, 46b (and 56b - not plotted), show the highest and most varied reflectance, matched overall by the reference spectrum 'kaolinite-2' from the Jet Propulsion Laboratory (JPL) spectral library. Samples 46a and 46b were obtained from two adjacent terraces in the western part of the Sambusu area. On the aerial photograph they belong to characteristic type 3a (Table 4.3). On the combined aerial photograph/PC 4-2-5 image (Figure 4.3) they are seen to correlate with a greenish cyan colour. They also have a similar greenish cyan colour on the inverted log residual image (Figure 4.2D). Sample 56b occupies a midway position spectrally within this group, but was obtained some distance away from a topographic depression near the current river channel in the north east of this area.

The second group, comprising samples 48 and 53, come from reed covered, clay-rich depressions which correlate with old channels. Both samples have a lower reflectance than the first group, and are approximated by the reference spectrum 'kaolinite-1', also from the JPL library. On the PC 4-2-5 image, the spectral responses of these samples are dominated by red or magenta colours due to vegetation. On the inverted log residuals image (Figure 4.2D), they tend to have a violet colour.

The third group consists of samples 52, 54 (and 55b - not plotted), and show the lowest albedo. In Figure 4.3 they are seen to occur within narrow topographic depressions of the clay infilled hollows of the lateral accretion sets. On the inverted log residuals image they correlate with pale yellow/buff areas.

Figure 4.16 shows a T-Spectra display with log residuals pseudospectra plotted from heavily vegetated locations in the Sambusu region. These sites are known to have clay but the characteristic TM2-TM3-TM4 v-shaped triplet suggests that the response here is dominated by vegetation.

#### **4.2.3.3 Other lithologies**

The soils of the Okavango River flood plain are predominantly sands and silts. The spectral responses of different surface materials in the various images are summarised in Table 4.4. As seen in Figure 4.2A, the dominant colour in the meander scrolls on the PC 4-2-5 image

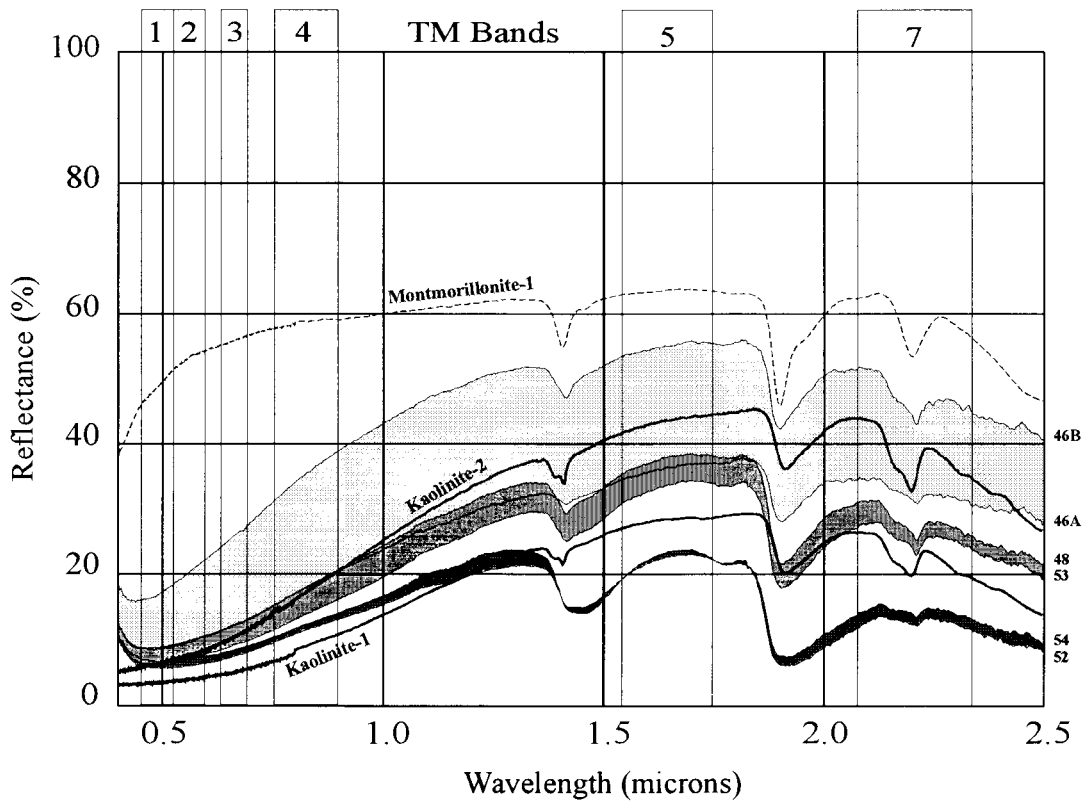


**Figure 4.15** Laboratory reflectance spectra of clay samples from the Sambusu region showing three main groups. Also plotted for reference, are the kaolinite-1 & 2, and montmorillonite-1 spectral profiles from the JPL library.

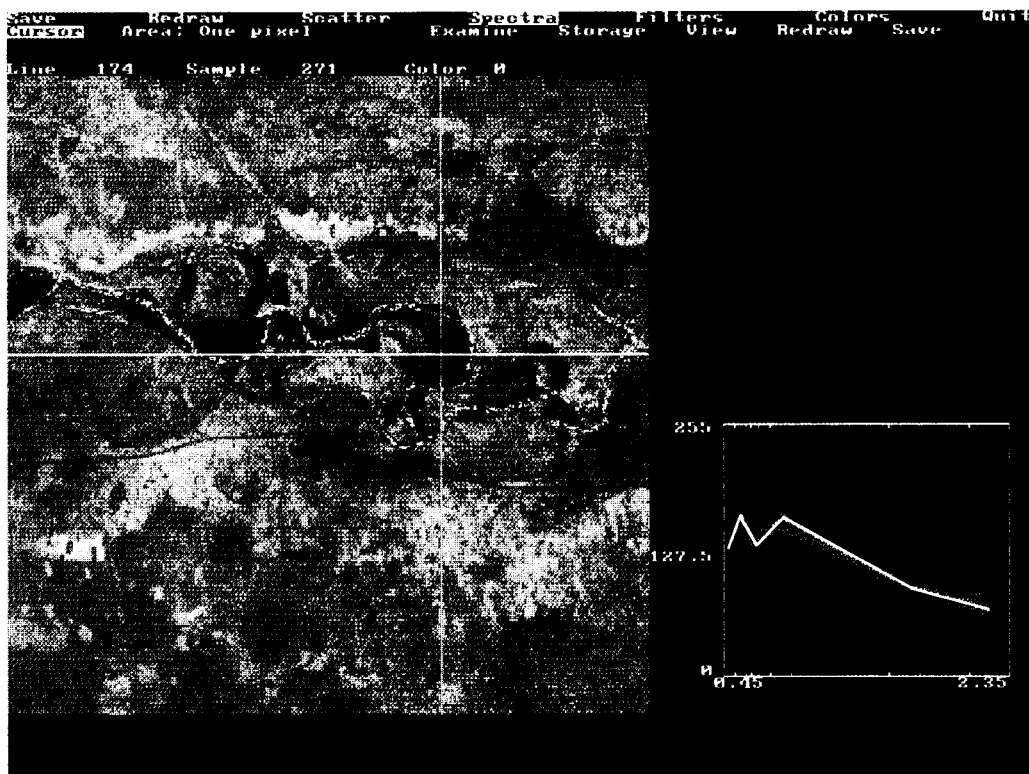


**Figure 4.16** T-spectra display with log residuals pseudospectra, from reed covered, clay-rich areas of the meander deposits in the Sambusu region. The v-shaped triplet of TM2-TM3-TM4 is a characteristic vegetational response.

Table 4.4 Summary of image and ground correlations for sands/other materials from the Okavango River flood-plain and environs.

<b>S A N D S</b>	moderately vegetated	<b>Air photograph characteristics</b>	<b>PC's 4-2-5</b>	<b>PC's 3-2-1</b>	<b>Ratios 5/7-4/3-5/1</b>	<b>Inverted Log-Residual 7-4-1</b>	<b>Ground Correlations</b>	<b>Sample Sites</b>				
		(5) Very light coloured areas of clear ground with varying amounts of scrub and tree vegetation, thus ranging to mid grey. Morphology is as "islands" and banks surrounded by darker tones, which nearly always occupies the relatively high ground on terraces.	violet/magenta varying to red.  magenta-purplish blue	nearly black (eg. #45), but green where same unit is more covered by vegetation.  -----	very dark grey (almost black).  black	yellow  -----	Sand banks composed of quartz, mostly clear but 5-10% yellowish. Possibly with some feldspar. Very thin grass cover (5-20%) ?  Very white sand with <5% grassy vegetation. Sand is mostly clear, pure quartz, although some are yellowish.	2A, 10A, 45  37				
		(6) Light open areas, similar to above, but slightly greyer in tone. Very open ground, probably with thin grassy cover, or isolated trees.	pale bluish cyan	slightly mottled mid/light green	mottled, darkish blue	bluish cyan	Fine, pale brown silty sand covered by 50-70% low cropped grass (eg. #49). Probably an overbank sand deposit. Also coarser brownish sand with 35% vegetation.	49, 50, 81 94				
		(7) Upper terrace, mid-grey, scattered discrete trees and thorn bushes.	yellow	-----	violet/very dark blue	-----	Open areas of dark sand with some feldspar (still 90% quartz). Evenly scattered vegetation (bushes and low trees)	5				
		(8) Mid-grey area in zone of stabilised sand "dunes" between "islands" of darker grey, more vegetated ground.	purple	-----	black (indistinguishable from surrounds)	-----	Hard, sandy area; grey in part and of variable composition.	7				
		(9) Black, grey and white tones (± sun glint)	black	mid-blue	black (speckled)	yellow (speckled)	Water					
		(10) White (linear)	darkish blue	black	black	yellow	Roads (and paths ?)					
<b>O T H E R</b>												

is mottled cyan. The pale greenish cyan mainly corresponds to the sandier ground where there are fewer reeds, including crevasse splay sands. The slightly darker blue to cyan areas are mostly alternating clayey silts and sands of the laterally accreted meander scroll deposits, which are variably covered by flattened dried reeds. On the merged aerial photograph/PC 4-2-5 image (Figure 4.3), the overbank and crevasse-splay sands are clearly delimited as white or pale bluish cyan.

Figure 4.17 shows the limited variability of laboratory spectra of the sands from the Sambusu region. Although not individually identified, the samples are from localities 45 (uppermost terrace sand), 49 (overbank sand), 50 (crevasse splay sand), 55a (modern point bar sand) and 56a (sandy ridge in lateral accretion lobe sheet), which are plotted in Figure 4.3. Their spectral profiles correlate well with 'kaolinite-3' from the JPL library, suggesting that these sands are kaolinite bearing. A comparison reference spectrum, 'quartz sand-1' is also shown in Figure 4.17, but has a flatter shape and higher average albedo.

Pseudospectra of various sands from the Sambusu region are shown in Figure 4.18. The large cursor cross on the TM band 7 log-residuals image (not inverted) indicates where the highlighted white pseudo-spectrum comes from. Most of the spectra are either sub-horizontal or slope towards the shorter wavelengths in the region between TM4 and TM7. This is typical of quartz sands from the JPL spectral library. The sharp break in slope between TM3 and TM4 probably indicates a vegetational response.

Calcrete, which is extensively used for road construction, generally appears dark blue on the PC 4-2-5 image (Figure 4.2A). Mottled dark blue areas adjacent to the road are calcrete quarries. Excavations visited show that the calcrete is typically buried to a depth of 0.6-1.5 m. The overlying surface soils are generally grey weathering, brown, medium to fine grained sandy loams, containing calcrete debris. At Sauyemwa, near Rundu, (locality 1) white calcrete has been used for low-quality brick making (Figure 4.19). The calcrete at this location appears turquoise blue on the PC 4-2-5 image. However, not all the dark blue areas on the PC 4-2-5 image are calcrete; brightly reflecting quartz-rich sands often have the same appearance (e.g. localities 6b and 8 near Sauyemwa, and near locality 80, 2.5 km east of Rupara Mission). Another material which appears dark blue on this image is a white powdery efflorescence occurring in a valley bottom, some 2 km south of Nakazaza (not identified). Yellow on the PC 4-2-5 image in the uppermost terrace corresponds to quartz-rich Kalahari Sands. or pale bluish cyan.

#### **4.2.4 Summary of NE Namibia results and conclusions**

A reasonable correspondence was found between the enhanced TM imagery and the surface materials. Unlike Sinai, the best discrimination was found in principal components images, rather than logarithmic residuals or ratio images. This is probably due to the increased difficulty of detecting mineralogical differences in the presence of a significant vegetation component. However, understanding the spectral significance of the PCs is difficult.

When used in conjunction with high-resolution stereo aerial photographs and limited fieldwork, the PC imagery allows the distribution of various surface materials and vegetation to be rapidly 'mapped' over wide areas. In the areas studied, potential sources of clay have been effectively delimited, at least at the reconnaissance level.

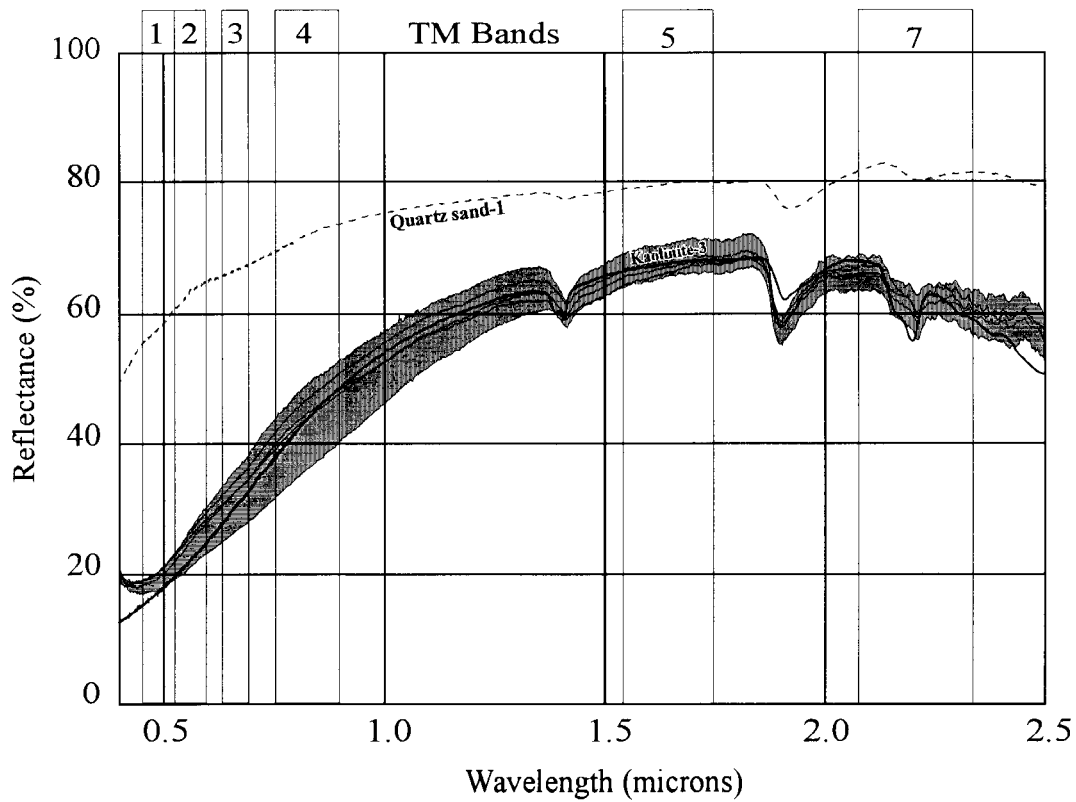


**Figure 4.17** Laboratory reflectance spectra of kaolinitic sands from the Sambusu region showing spectral reflectances which closely match the kaolinite-3 reflectance spectrum from the JPL library. Also shown for reference is quartz sand-1, from the same spectral library.

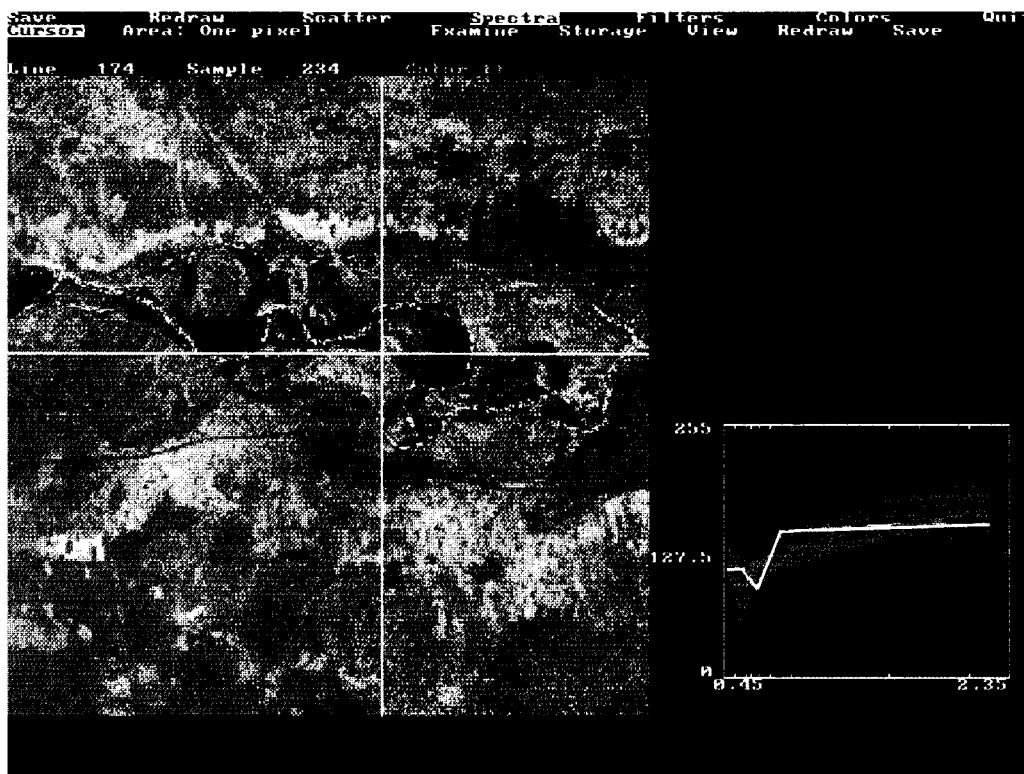


**Figure 4.18** T-spectra display with log residuals pseudospectra of various sands from the Sambusu region. The sub-horizontal to gently inclined spectra towards shorter wavelengths between TM4 and TM7 is typical of sands.

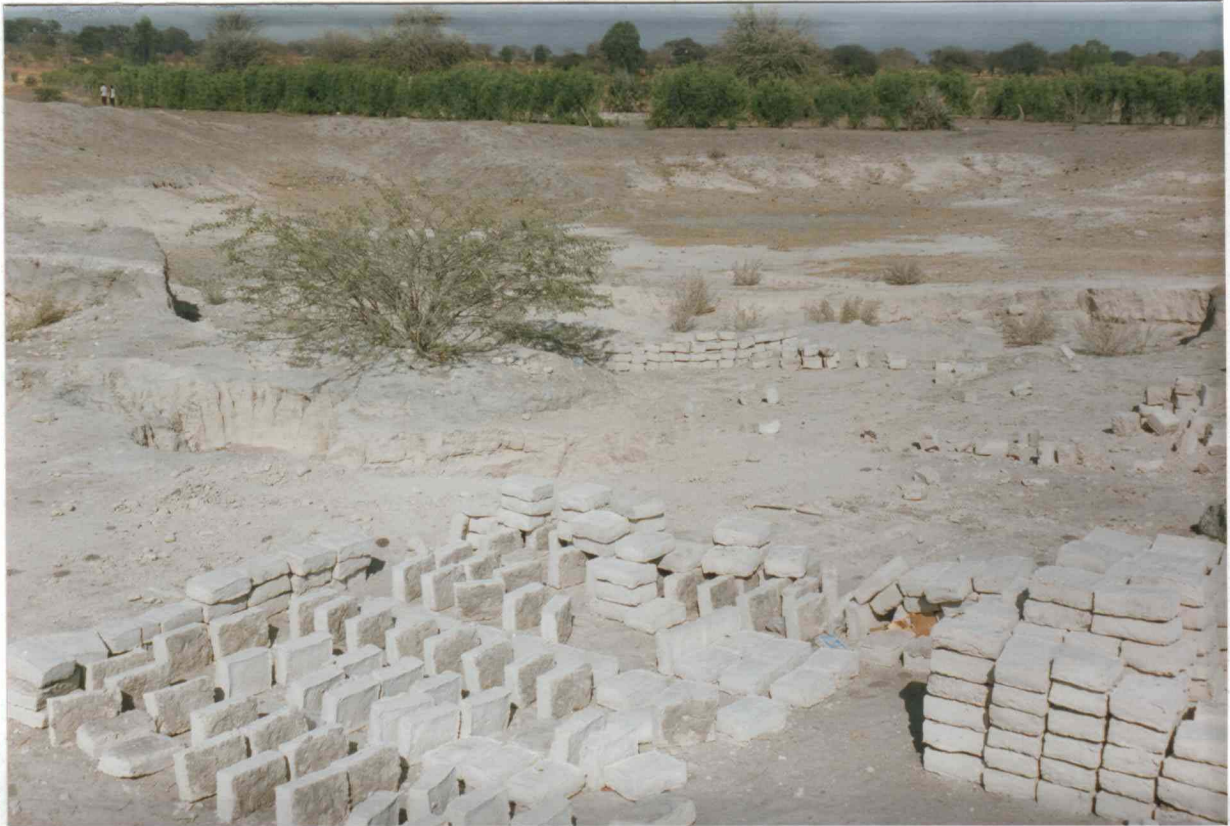


**Figure 4.19** Calcrete is locally used for making bricks at Sauyemwa, west Rundu.

A more detailed understanding of the TM data would require spectral unmixing models to be applied over those areas with low to moderate vegetation cover. This might allow the preliminary interpretations to be refined.

Both XRD and laboratory spectral analysis showed that the clays and sands contained kaolinite. Montmorillonite was generally a trace component, but was found to increase in abundance over kaolinite to the east of Rundu. The high quartz content of nearly all the samples, suggested by the XRD results, was unexpected; however, this analytical technique may not be a reliable indicator.

### **4.3 Windhoek area**

A second test site in Namibia was chosen in order to test the methods in an area more typically semi-arid than the Okavango flood plain. Based on the report *Industrial Rocks* by Schneider & Diehl (1991) and information provided by the Geological Survey, an area lying some 60 to 80 km to the east of Windhoek near to Otjivero was selected for further examination (Figure 1.2). Within this region, the report cites a number of small clay-rich occurrences mainly along the course of the White Nossob River. Most of the work was carried out in this area.

In addition, a road reconnaissance was undertaken to the north and west of Windhoek, between Okahandja and Karibib. This is not within an area covered by the Landsat image but appears to contain interesting clay occurrences. To judge from preliminary field evidence, it is an area that might reward some further investigation.

#### **4.3.1 Geological setting**

The Otjivero area to the east of Windhoek lies within the Damara Orogen. The bedrock in this region consists of a strongly deformed nappe sequences of metasedimentary and metavolcanic rocks consisting of various quartz-mica ( $\pm$  graphite) schists, quartzites, marbles, quartzites, amphibolites, arkose, conglomerate and granite. The geology is described by Kasch (1983). Exposure is generally poor but where the sand cover is thin, sub-outcropping bedrock can be seen. Though not covered by thick Kalahari Sand deposits, aeolian sands nevertheless make up a significant component of the surface over virtually all of the area. Beneath the wind-blown sand cover, the soil would appear to be generally residual and autochthonous.

Although the geological map shows a variety of lithologies in this area, the mineralogical composition of the erosional sandy soils does not vary greatly. Quartz silt/sand in one form or another is by far the most common mineral and, together with feldspar, probably makes up more than 90% of the surface materials over much of the area. Small amounts of mafic minerals are also present, varying in type and amount according to the bedrock.

#### **4.3.2 Image processing**

The area of main interest to the east of Windhoek lies along the northern margin of Landsat TM scene (177-076); a cloud-free scene acquired 23 January 1987 was obtained. The January acquisition date corresponds to the middle of the rainy season.

The image data were corrected for atmospheric path radiance effects using a histogram minimum method. Band combinations and processing were determined on the basis of past experience in similar terrain and visual comparisons. Two FCCs were prepared: the first of bands 4-5-3 and the second of bands 1-5-7. These were enhanced using a piecewise linear stretch to obtain the best visual image with maximum overall image discrimination.

A log-residuals transformation was carried out. The values were inverted so as to highlight areas of TM7 absorption. An FCC image of inverted log-residual bands 741 was produced. In this colour combination, areas of strong TM7 absorption appear in reddish tones. Screen photographs were taken of all three image composites for field evaluation and comparison.

### **4.3.3 Evaluation and field correlation**

#### **4.3.3.1 Area description**

The field visit was planned for the same season as the image was acquired. However, at the time of fieldwork (late January/early February 1994) the area experienced extremely heavy rainfall ending a long drought. As a result, exceptional vegetation growth occurred which masked much of the ground and made correlations with the image difficult. Local opinion indicated that the vegetation cover was almost certainly more than in January 1987. This was confirmed by inspection of the 453 FCC image (Figure 4.20A) in which vegetation, highlighted in red, is not a dominant feature except along the tree-lined banks of the White Nossob River. The inverted log residuals 7-4-1 image for the same area is also shown in Figure 4.20B.

The study area along the White Nossob River is a peneplained erosion surface with occasional small hills and some larger 'kopjes'. The area is wholly ranchland and supports a low density of cattle. The natural vegetation of this area is open savanna scrubland supporting a variable cover of low thorn bushes and small thorn trees. Large *Acacia* and other trees grow along the margins of the White Nossob flood plain and sporadically elsewhere. Vegetation patterns only locally correspond to bedrock geology. Local opinion was that the vegetation was largely natural and that distribution patterns persisted for long periods. However, there were indications that clearing had played a part, perhaps through burning - either natural or planned. Based on borehole results, opinion was further that scrub vegetation distribution was not generally related to groundwater. The effects of grazing and variable land use have had a significant effect on overall image responses. These are obvious along man-made boundaries, but elsewhere are only suspected.

Despite the generally thin vegetation cover, there appears to be a significant spectral contribution from vegetation in the January 1987 image. Plant materials includes healthy green-leaved trees, scrub and grass, as well as senescent and dead plant litter, all of which contribute to the spectral response.

#### **4.3.3.2 Field evaluation**

The report by Schneider & Diehl (1991) described several small deposits of clay used in the past for local brick-making. The deposits occur in the vicinity of the White Nossob flood

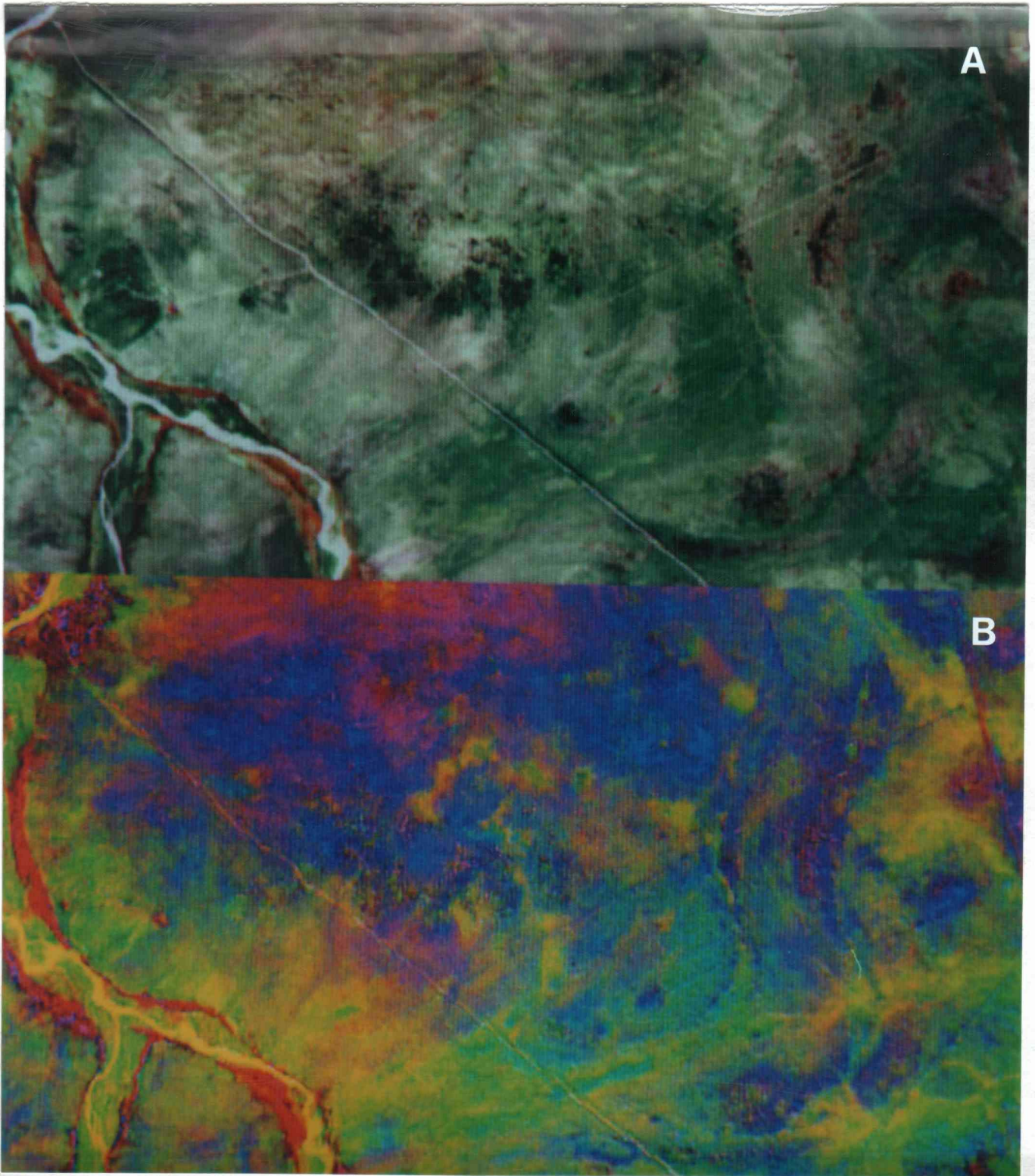


**Figure 4.20** A: FCC of band 4-5-3. Red colours mainly bordering the white Nossob River, indicate healthy green vegetation. B: inverted log residuals 7-4-1 image of the same data. In this image, red, orange and yellow indicate absorption in TM7.

plain. The present visit confirmed that no extraction had occurred for many years, to the extent that it was often difficult to locate the sites with certainty.

Most of the deposits appear to be quite restricted in size and buried under a half-metre or more of sand. Many are also masked by shrub and/or tree vegetation; this results partly from their closeness to the river but possibly also the water-retaining properties of the clay-rich soils. Schneider & Diehl (*op. cit.*) note that alluvial clay occurrences along the larger dry river courses in Namibia are without exception overgrown with *Acacia karoo* (White Thorn tree); at one of the localities near the White Nossob they note that a growth of *Acacia horrida* over a clay deposit. These factors combine to make the detection of these deposits by remote sensing extremely difficult.

Prior to fieldwork, a T-Spectra analysis was carried out in order to characterise the pseudospectral responses on the inverted log residuals 7-4-1 image. This examination revealed the same general features in different part of the image suggesting similar ground materials. The analysis focused particularly on areas within the image showing apparent TM7 absorption. Comparisons with the kaolinite-related pseudospectra from Sinai suggested the possibility of clays in some instances. It was anticipated that any clay spectra would be modified by quartz-rich sand and vegetation, but it was uncertain exactly what spectral characteristics to expect.

On the 7-4-1 image (Figure 4.20B) areas of TM7 absorption generally appear in yellow or orange depending on the contribution from other bands. Other image responses were also examined under T-Spectra in order to build up an understanding of the log residuals image as a whole. Areas containing obvious green vegetation were analyzed in order that minor contributions from vegetation might be recognized elsewhere. Green vegetation is easily identified by the distinctive TM2-3-4 triplet in its pseudospectrum.

Subsequent fieldwork involved an examination of sites where 'anomalous' spectral signatures or other features of interest were noted, and included the collection of samples for laboratory spectral analysis. It was clear from the outset of fieldwork that the masking effects of sand and vegetation, and the small size of the deposits, made it unlikely that clay minerals could be detected by the TM sensor. Many of the anomalous pseudospectra appeared to correlate with slightly increased vegetation, although this was difficult to prove due to the abundant new vegetation. Such areas appeared to have more scrub bush and some small trees, but clay was not obviously present. By contrast, areas which appeared dark blue on the inverted log-residuals image, were found to be more thinly vegetated and/or were over-grazed.

The laboratory reflectance spectra were measured of samples where clays had originally been suspected from the image pseudospectra. Figure 4.21 shows the spectra of samples from four such sites (lower curves), together with JPL library spectra for a pure quartz sand and a kaolinite, all reduced to the 6 band passes of the TM sensor. Apart from the overall lower albedo, similarity to the quartz spectrum is apparent but the drop in reflectance values from TM5 to TM7 is more typical of the kaolinite. Although far from conclusive, the results suggest that the field samples are clay-bearing sands.

Laboratory spectral measurements of dead vegetation (dead grass, thorn bush and wood) are shown in Figure 4.22, together with reference spectra representing typical healthy green

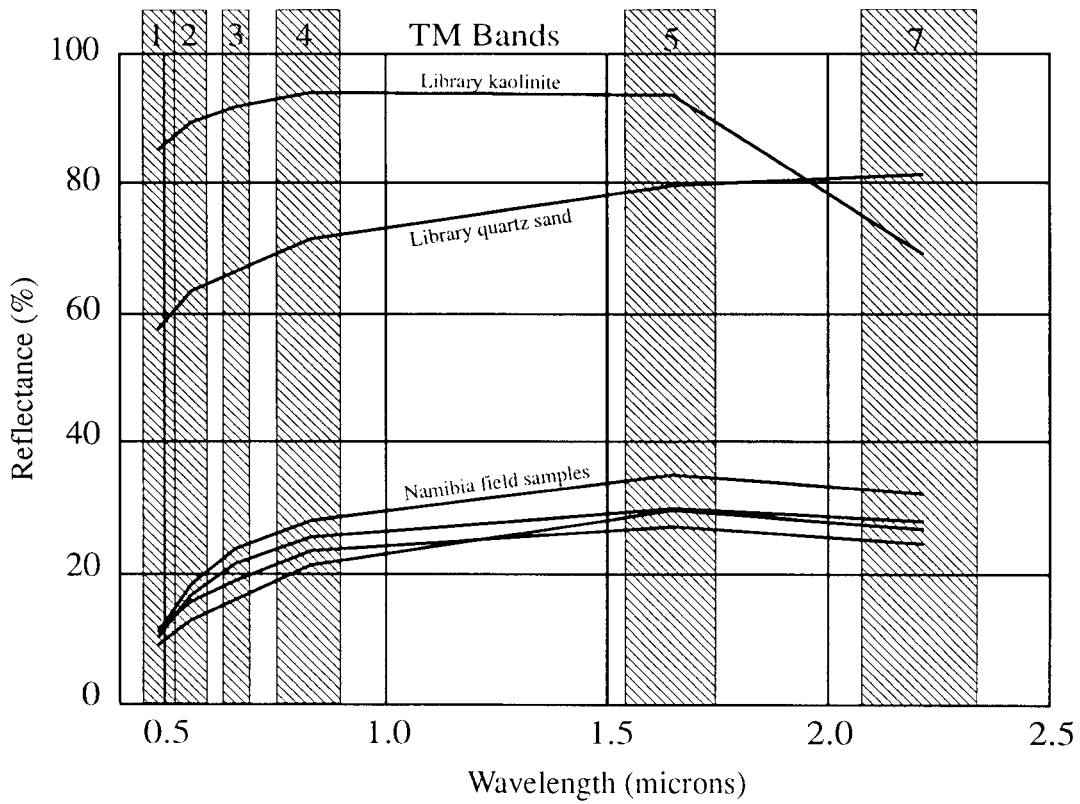


**Figure 4.21** Comparison between JPL library spectra resampled to TM band widths and similarly resampled IRIS spectra of 4 samples from central Namibia.

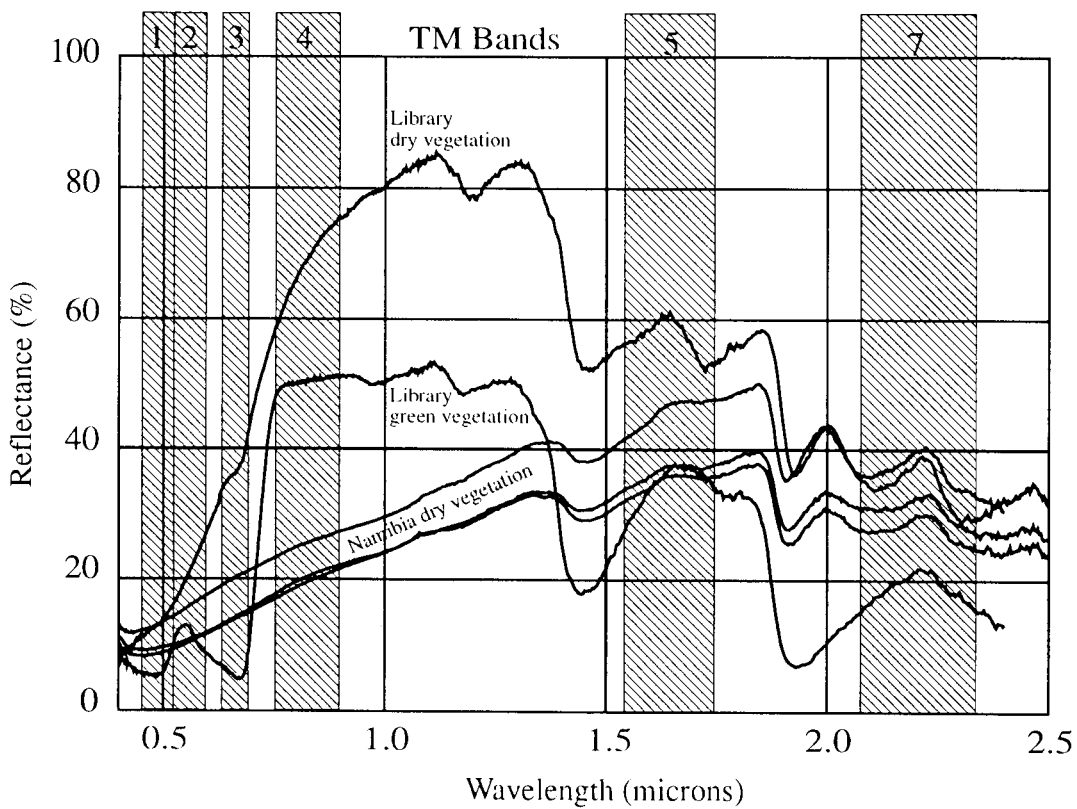


**Figure 4.22** Comparison of JPL library spectra of green and dry vegetation with IRIS spectra of dead vegetation from central Namibia.

vegetation (grass) and dead vegetation (dry *Calluna* leaves). The three Namibia spectra are all similar; they lack the high near-infrared reflectance characteristic of green vegetation but show similarities with the dry vegetation reference spectrum, especially in the shortwave infrared region beyond about 1.8  $\mu\text{m}$ . These spectra will provide useful data for follow-up work on spectral mixture modelling in semi-arid terrains.

Despite the lack of progress towards the main objective - detecting clays - the study provided a further opportunity to assess the value of the T-Spectra approach to general lithological interpretation. The inverted log residuals allows colours to be analyzed and classified in terms of simple pseudospectral curves. However, because the processing effectively removes topographic shadowing, it is less easy to visualise as a map and it subdues structural features which are partly expressed by relief. This can be seen in Figures 4.23A and B which show a 4-5-3 FCC and an inverted log residuals 7-4-1 image respectively (compare also Figures 4.20A & B).

#### **4.3.4 Karibib-Okahandja reconnaissance**

Schneider & Diehl (1991), referring to Hälbich (1964), noted various occurrences of clay in the Okahandja District. Although no imagery was available for this area, a brief road reconnaissance was made along a 70 km stretch of the B2 highway from west of Karibib to Okahandja, continuing on the B1 towards Windhoek (Figure 1.2).

Compared with the previous field area to the east of Windhoek, the region is generally less thickly covered by aeolian sand and the vegetation is far denser, making it perhaps still less suitable for detecting clays by remote sensing. However, throughout this region (i.e. the entire stretch of the B2 and the B1 extending some 10 km south of Okahandja) are to be seen tall chimney-like termite mounds which are well-cemented and appear to have a moderate clay content. The ground typically shows a very thin ( $\approx 1$  cm) covering of loose sand rapidly passing into grey/brown silt and, beneath this clay-rich material at shallow depth.

Several samples of the material composing the termite chimneys and the sub-surface soil were spectrally analyzed. Three such samples (collected from different sites over a distance of 14 km adjacent to the main road) are shown in Figure 4.24, together with JPL library spectra of a quartz sand and a pure kaolinite for comparison. The field samples are all similar, and have the gross features of quartz whilst showing the diagnostic absorption of kaolinite with a shoulder at around 2.17  $\mu\text{m}$  in the main 2.2  $\mu\text{m}$  absorption. No chemical analyses of the materials were carried out but on spectral grounds they are concluded to be clay-rich silts/sandstones (or sandy clays). Although no firm conclusions can be reached, the reconnaissance suggests that clay-rich soils may be present over much of this area.

#### **4.3.5 Summary of Windhoek results and conclusions**

The area east of Windhoek proved somewhat atypical of the semi-arid environment in many respects. The small size and very restricted geological occurrence of individual clay deposits, their burial beneath a substantial sand cover, and the obscuring effect of vegetation made their detection extremely difficult. However, advances were made towards the goal of more objective image interpretation techniques and provided further encouragement that the spectral interrogation techniques can be applied to general lithological discrimination.

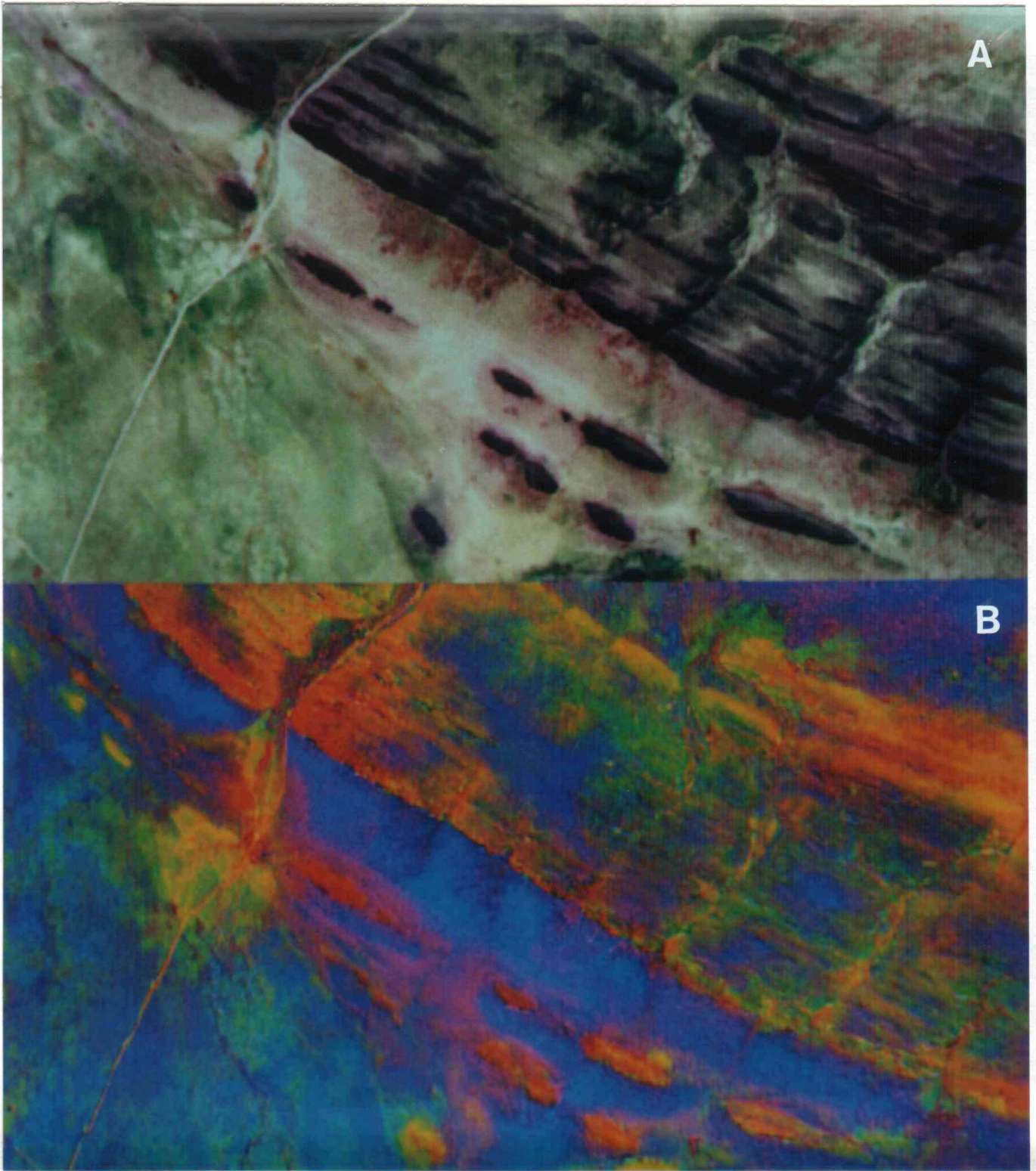


**Figure 4.23** A: FCC of bands 4-5-3. Topographic shadowing gives the perception of relief. B: inverted log residuals 7-4-1 image of the same area. This image appears 'flat' by comparison.

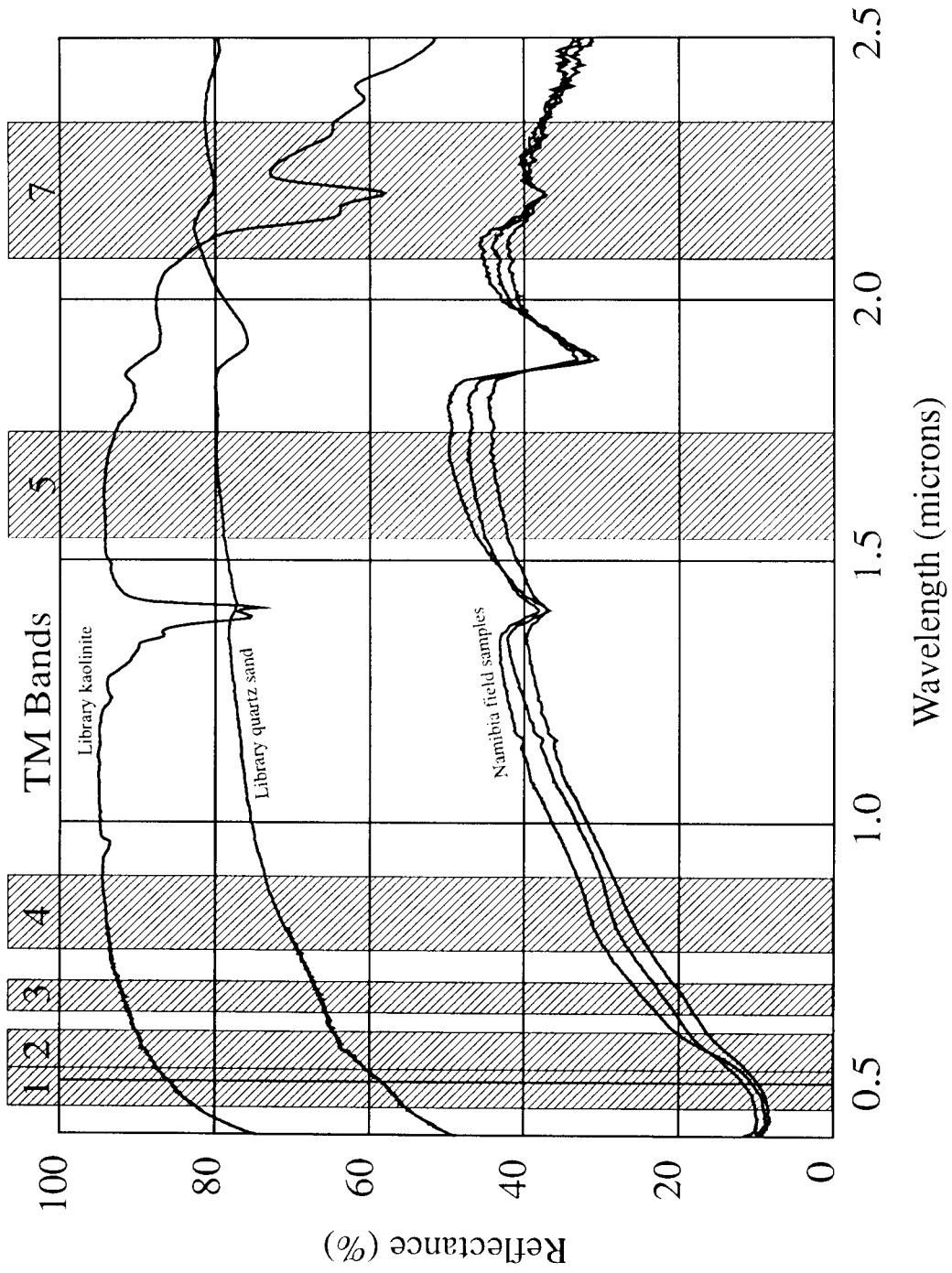


**Figure 4.24** Comparison between IRIS spectra of clay-bearing samples from the Karibib-Okahandja area, central Namibia with JPL library spectra of kaolinite and a pure quartz sand.

Clearly, the remote identification of such deposits will always be difficult in the presence of vegetation using a coarse resolution, broadband sensor such as Landsat TM.

#### **4.4 General conclusions: semi-arid area**

Namibia was chosen to test the earlier developed methods (here applied to the reconnaissance for clays for local brick-making) in a more vegetated, semi-arid environment. However, both the Okavango River and the White Nossob test sites proved somewhat atypical of semi-arid areas due to (1) the limited geological occurrence of clays only as flood-plain deposits; (2) the effects of significant and grossly changing vegetation causing masking and mixed spectral responses, and (3) the masking of the clay deposits by sand overburden.

Vegetation is a difficult problem to deal with because its shortwave infrared responses at the coarse spectral resolution of the Landsat TM are somewhat similar to clay. However, the use of logarithmic residuals and T-Spectra analysis can go some way towards separating these signals. Whereas the studies failed to conclusively show that the methods work in a semi-arid environment, the study provided encouragement that the techniques could be used where more extensive occurrences were exposed, even in the presence of a substantial (though not totally overwhelming) vegetation contribution. It is apparent that further work is required in a more typically semi-arid terrain where vegetation patterns are more invariant, and image processing can be more predictive. In the case of Namibia, interpretation of imagery relies more on discriminating complex ground units defined by associations of composition, vegetation and geomorphology than on the recognition of actual mineral absorptions. The digital merging of Landsat imagery with aerial photography provides a high spatial resolution image that combines many of the individual benefits of each data type.

## 5. SUMMARY, CONCLUSIONS AND RECOMMENDATIONS

*Synopsis: The basis of the remote sensing method is restated, the results outlined and the main conclusions summarised. The advantages and limitations of the approach are briefly reviewed and suggestions made for tackling outstanding research issues in the context of possible operational implementation.*

### 5.1 Summary of approach

Local sources of industrial minerals, including building materials, are important for industry, community development and housing programmes in many developing countries. This study represents an attempt to develop low-cost remote sensing techniques to aid the search for such minerals in arid and semi-arid terrains. The method involves a semi-quantitative approach to interpreting widely-available satellite imagery, such as Landsat TM. The aim of the work has been to develop an operational methodology for reconnoitring poorly known terrain, quickly and cheaply.

The basis of the method is that many minerals of industrial importance, including clays, sulphates and carbonates, exhibit diagnostic spectral responses that can be detected in remotely sensed images. This is manifested, at the coarse spectral resolution of the Landsat TM, by low reflectance in TM7 (shortwave infrared). In the past, this response has been used to recognise rock alteration haloes associated with metallic mineralisation. Although the spectral resolution of Landsat TM is generally insufficient for the precise identification of individual minerals, information contained in the data can be used to make provisional predictions and target likely occurrences of industrial minerals as part of a regional exploration strategy.

The project has involved the comparison of various conventional and new image processing and data analysis procedures. An important emphasis was on a spectral analysis approach to image interpretation, rather than reliance on conventional visual discrimination of image tones. This involved converting the raw radiance signal recorded by the satellite sensor to values more closely approaching true laboratory reflectance using a image processing technique called logarithmic residuals. Once in this form, the data could be analyzed as 'pseudospectra' using spectral analysis software, thereby permitting the study of all six reflective bands at the same time.

The project involved attempts to apply the methods to the search for a limited range of industrial minerals (clays, carbonates and sulphates) in an arid area (Egypt) and a semi-arid region (Namibia). Field investigations were undertaken in both countries. In addition, a desk study was carried out to examine the theoretical potential for extending the method to cover a broader range of industrial minerals and rocks. New software was written to convert full-resolution laboratory reflectance spectra to the waveband intervals of broadband satellite systems.

## **5.2 General results**

The work in Egypt demonstrated that Landsat TM imagery can be successfully used in a well-exposed arid region to discriminate, and in some cases provisionally identify, certain rocks and minerals of industrial significance - in this case kaolinite and gypsum. The success of the method was found to be somewhat variable between sites; it worked best in areas of good rock exposure, undisturbed by development and with simple ground materials dominated by a single mineral. Conventional image interpretation is nevertheless useful in arid terrain, particularly using ratio composite images, and complements the more rigorous spectral approach.

Attempts to apply the method to the search for brick-making clays in the semi-arid environment of Namibia proved more difficult due to (1) the restricted distribution of clay deposits, and (2) problems of masking and spectral mixing caused by dense vegetation cover and sand overburden. Despite this, the studies provided an opportunity to evaluate a range of different image processing techniques for general lithological and mineral discrimination. This included the digital merging of an aerial photograph with a principal components TM image. The overall results support the view that the method could be adapted for a more typical semi-arid environment, provided that the materials sought were reasonably well exposed and that some supporting field information was available.

A new and important approach developed during this project involved the interactive interrogation of the log residuals TM image using a spectral analysis program called T-Spectra. Whereas conventional image processing, such as false colour band composites and ratio composites, can highlight areas of TM7 absorption, the logarithmic residuals images can be used to map spectral responses in direct reflectance-related, mineralogical terms. T-Spectra can be implemented on a simple personal computer and is therefore potentially field-portable. In this approach, simple pseudospectra, corresponding to six of the Landsat TM bands, are compared and their shapes analysed. Since the technique does not depend on the visual interpretation of image colours, the approach is more objective and quantifiable. Individual locations in the image can be examined in terms of their pseudospectra and comparisons made with both known and unknown sites in the image. Because the approach takes account of overall differences in the shape of the pseudospectra, rather than responses only in TM7, the separation and recognition of a range of minerals and lithologies is possible. The main difficulty is in recognizing and interpreting mixed lithologies comprising different materials that individually cause TM7 absorption (such as mixed clay, sulphate and limestone materials). 'False anomalies', caused by materials of no economic interest, occur but can often be distinguished on the basis of differences in albedo, absorptions in other TM bands, outcrop pattern and prior field knowledge.

## **5.3 Remaining problems and solutions**

The project has established the basis of a method for interpreting Landsat TM imagery in a semi-quantitative manner but some questions remain which will need to be addressed prior to, or as part of, any operational implementation. These are summarised below together with possible solutions or approaches.

1. The current log residuals software as applied to Landsat TM produces pseudospectra in which the values in the visible wavebands are higher than expected. This may be due to the atmospheric correction applied or a failure of the data to meet the assumptions of the log residuals calculation. Although these differences are unimportant so far as within-image comparisons are concerned, the lack of correspondence with laboratory spectra precludes library reference spectra being used for direct mineral identification at this stage. The specific problems, and the results of initial attempts to solve them, are summarised in the following paragraph.

The log residuals technique requires that the data are free of any additive atmospheric component; without such a correction it is not possible fully to remove the topographic and illumination factors since the additive component cannot be separated. As this correction is wavelength dependent, any residual atmospheric component will have a greater effect in the short wavelength visible bands. The development of an accurate method for atmospheric correction of satellite data remains a research priority for the remote sensing community. The failure of actual data to meet the assumptions of the log residuals technique has been addressed by Tsuchida *et al.* (1994). By using data for materials known or assumed to have a flat spectral reflectance in the image, the log residuals technique can be recast to yield pseudospectra of more acceptable form in the visible wavebands. Attempts were made to implement this procedure for some of the Egypt data but with limited success, due mainly to the difficulty of identifying reference pixels which have a flat spectral response. However, the results were encouraging and justify further work to better understand the log residuals method.

2. Mixed mineral assemblages cause difficulties for the spectral analysis approach. The simple pseudospectral curves possible with TM, and the large range of potential minerals, make the unmixing of complex mineral pseudospectra extremely difficult. One approach might be to first decide the range of likely minerals based on a knowledge of the geology of the area. Developments of pixel unmixing techniques could significantly improve the usefulness of the spectral approach. Such work should also address the important question of separating out mixed vegetational responses.
3. The desk study has shown that spectra for a range of mineral families, reduced to the band passes of Landsat TM or JERS-1, can be theoretically assigned to one of a few groups on the basis of general shape. A knowledge of the local geology and mineralisation could then be used to make provisional identifications. In this way it should be possible to extend the methods to a much larger range of minerals than was attempted in the present project. This approach again requires that the log residuals computation produces pseudospectra that more closely match the laboratory curves (see 1 above).
4. Whereas the image-interrogation approach has clear advantages, the present implementation of the T-Spectra program displays only a single band black-and-white image on the PC screen. The program would be considerably improved from a user's viewpoint if a colour composite image were displayed instead. It should not be a difficult task to modify the T-Spectra software accordingly.

## 5.4 Conclusions and recommendations

Rapid, cost-effective methods of mineral exploration are important in developing countries particularly where the commodities sought are relatively low unit-value bulk industrial minerals. The use of remote sensing can help stimulate interest by identifying possible targets for mineral exploration in poorly known areas. Used in the initial stages of a field programme, remote sensing could provide valuable and cost-effective inputs to the planning and logistics of the main exploration phase.

Despite certain limitations, the project has demonstrated for the first time that widely available, broadband multispectral satellite imagery such as Landsat TM can be analysed spectrally to *provisionally identify*, rather than merely *discriminate*, ground materials. The technique is capable of targeting a range of industrial minerals as part of a reconnaissance exploration strategy. Moreover, the method is applicable not only to minerals displaying TM7 absorption, but to other industrial minerals and rocks, including gravel aggregates, limestones, and calcrete. Indeed, the approach has considerable potential for general lithological and minerals mapping. The methods work best in arid environments but could be adapted for more vegetated terrain provided the occurrences sought, or their erosional products, are reasonably exposed at the surface.

Implementation of the techniques is immediately feasible in Egypt and in other broadly similar geological and climatic settings. Elsewhere, orientation studies over known occurrences should first be carried out to establish local remote sensing responses, and the methods modified accordingly.

Further verification of the technique is recommended, perhaps in the context of a full feasibility study related to a development project. The approach is regarded as having considerable future potential as newer satellite data with more spectral channels become available. For example, the methods could be considerably improved by using JERS-1 imagery or the planned satellite ASTER which has 5 bands covering TM7 and is due for launch in 1998. Such a study might usefully concentrate on an expanding population centre in an arid region. The exploration targets should include a range of industrial minerals, and research should address the questions of atmospheric correction, alternative implementations of the log residual transform, and pseudospectra unmixing. The aim should be to produce a regional industrial mineral inventory via a classification of the TM (or JERS-1) data.

Finally, it should be stressed that the methods described here in no way purport to be a means of remotely identifying *economic* industrial mineral deposits, even under ideal conditions. Remote sensing is not a substitute for fieldwork, but the methods provide a real means of targeting potential mineral occurrences so that the ensuing field effort can be more directed and cost-effective.

## ACKNOWLEDGEMENTS

Many people contributed to the work described. In Egypt we would like to express our thanks to the Egyptian Geological Survey and Mining Authority, its Chairman Dr G Naim, and to Dr A A Hussein and Mr M A Razeq for assistance during two field seasons. Thanks are due to the Sinai Manganese Company for providing accommodation, and the British Council in Cairo for general help. In Namibia, the Geological Survey provided advice, interest, and logistical support without which the fieldwork would have been much more difficult. Particular thanks are due to the Director, Dr B Hoal, to Dr G I C Schneider and to Erick Iyambo. The British High Commission in Windhoek provided the use of a vehicle. Laboratory support was provided by the NERC Equipment Pool for Field Spectroscopy and BGS Mineralogy and Petrology Group.

## REFERENCES

- Abrams, J.M., Brown, D., Lepley, L. and Sadowski, R. 1983. Remote Sensing for Porphyry Copper Deposits in Southern Arizona. *Economic Geology*, **78**, 591-604.
- Amos, B.J. and Greenbaum, D. 1989. Alteration detection using TM imagery: the effects of supergene weathering in an arid climate. *International Journal of Remote Sensing*, **10**, 515-528.
- Beadnell, H.J.L. 1905. *The topography and geology of Fayum Province*. Survey Department, Cairo, Egypt, 101p.
- Ben-Dor, E., Kruse, F.A., Lefkoff, A.B. and Banin A. 1994. Comparison of three calibration techniques for utilization of GER 63 channel aircraft data of Maktesh Ramon, Negev, Israel. *Photogrammetric Engineering and Remote Sensing*, **60**, 1339-1354.
- Bierwith, P.N. 1990. Mineral and vegetation mapping over mound spring deposits near Lake Eyre: an application of data-calibrated pixel unmixing using Landsat TM data. *Proceedings of the Fifth Australian Remote Sensing Conference, Perth, Australia*, **1**, 341-351.
- Chavez, P.S., 1975. Atmospheric, solar and MTF corrections for ERTS digital imagery. *Proceedings of American Society of Photogrammetry Annual Meeting*, Falls Church, Virginia.
- Chavez, P.S., Berlin, G.L. and Sowers, L.B., 1982. Statistical method for selecting Landsat MSS ratios. *Journal of Applied Photographic Engineering*, **8**, 23-30.
- Crippen, R.B., 1987. The regression intersection method of adjusting image data for band ratioing. *International Journal of Remote Sensing*, **8**, 137-155.
- Crippen, R.B., 1988. The dangers of underestimating the importance of data adjustments in band ratioing. *International Journal of Remote Sensing*, **9**, 767-776.
- Davis, J.C., 1973. *Statistics and data analysis in geology*. Wiley, New York. 646p.
- Denniss, A.M., de Souza, C.R. and Drury, S.A. 1993. Lithological discrimination using Landsat TM and JERS-1 SWIR data; initial results in the Oman ophiolite. In Hilton, K. (ed.). Towards operational applications. *Proceedings of the 19th Annual conference, Remote Sensing Society*, 8p.
- EGSMA (undated). *Geological maps of the Dahsur-Qatrani district*. Scale 1:100 000 and 1:250 000. Cairo.
- EGSMA. 1980a. *Mineral map of Egypt. Non-metallic mineral deposits and occurrences*. Scale 1:2 000 000, Cairo, Egypt.
- EGSMA. 1980b. *Geological map of Egypt*. Scale 1:2 000 000, Cairo, Egypt.

- EGSMA. 1983. *Geological map of greater Cairo area*. Scale 1: 100 000. Cairo, Egypt.
- El-Saiy, A.K. and Salama, I.A. 1993. X-ray diffraction analysis for 18 clay samples. *EGSMA Internal Report*, **56/93**, 3p.
- Geological Survey of Namibia, 1980. *Namibia Geological Map 1:1 000 000 (reprinted 1990)*.
- Gillespie, A.R. 1980. Digital techniques of Image Enhancement. In Siegal, B.S. and Gillespie, A.R. (eds.). *Remote Sensing in Geology*, John Wiley and Sons, New York, 139-226.
- Goetz, A.F.H., Rock, B.N. and Rowan, L.C. 1983. Remote Sensing for exploration: an overview. *Economic Geology*, **78**, 573-590.
- Green, A.A., Huntington, J.F., Gabell, A.R., Fraser S.J., Horsfall, C.L., Cocks, T. and Craig, M.D. 1985. An assessment of the exploration value of Aircraft TM data for Gold Exploration in Queensland. *CSIRO Institute of Energy and Earth Resources, Restricted Internal Report*, **1609R**.
- Green, A.A. and Craig, M.D. 1985. Analysis of aircraft spectrometer data with Logarithmic Residuals. *Proceedings of the First Airborne Imaging Spectrometer Data Analysis Workshop, JPL Publication*, **85-41**, Jet Propulsion Laboratory, Pasadena, CA, 111-119.
- Greenbaum, D., Marsh, S.H., Tragheim, D.G. and O'Connor, E.A. 1994a. Reconnaissance for industrial minerals using satellite remote sensing. In Mathers, S.J. and Notholt, A. (eds.). *Industrial Minerals in Developing Countries*, BGS/AJID Report, **18**, 55-66.
- Greenbaum, D., Marsh, S.H., O'Connor, E.A., McDonald, A.J.W. and Tragheim, D.G. 1994b. Advances in industrial minerals mapping in arid and semi-arid environments. *Proceedings of Tenth Thematic Conference on Geologic Remote Sensing, San Antonio, Texas, I*, 115-126.
- Grove, C.I., Hook, S.J. and Paylor, E.D. 1992. Laboratory reflectance spectra of 160 minerals, 0.4 to 2.5  $\mu\text{m}$ . *JPL Publication*, **92-2**, Jet Propulsion Laboratory, Pasadena, CA, 406p.
- Hälbich, J.W. 1964. First report on a preliminary investigation of clay deposits in central SWA. *Unpublished report Geological Survey of Namibia*, 9p.
- Hunt, G.R. 1977. Spectral signatures of particulate minerals in the visible and near infrared. *Geophysics*, **42**, 501-513.
- Hunt, G.R. 1980. Electromagnetic radiation: The communication link in Remote Sensing, in Siegal, B.S. and Gillespie, A.R. (eds.). *Remote Sensing in Geology*, John Wiley and Sons, New York, 5-45.

- Huntington, J.F., Green, A.A. and Craig M.D. 1989. Identification- the goal beyond discrimination. *Proceedings of IGARRS-89/12th Canadian Symposium on Remote Sensing, Vancouver, BC*, 6-11.
- Inglethorpe, S.D.J, Bloodworth, A.J. and Razek M.A. 1991. Evaluation of clays from the environs of Cairo, Egypt, for brick manufacture and use as bentonites. *British Geological Survey Technical Report, WG/90/38R*, British Geological Survey, Keyworth.
- Kasch, K.W. 1983. Folding and thrust tectonics in the south-eastern portion of the Damara Orogen around Omitara, Namibia. *Special Publication Geological Society of South Africa*, 11, 175-184.
- Marsh, S.H. and O'Connor, E.A. 1992. Exploration for building materials and industrial minerals in arid regions using remote sensing: progress report for 1992. *British Geological Survey Technical Report, WC/92/15*, British Geological Survey, Keyworth.
- Marsh, S.H., O'Connor, E.A. and Greenbaum, D. 1992. Industrial minerals exploration in Egypt using Landsat TM. *Proceedings of the Sixth Australasian Remote Sensing Conference*, 3, Wellington, New Zealand, 314-323.
- Marsh, S.H. and Tragheim, D.T. 1995. Laboratory Spectral Measurements, Industrial Minerals Project. *Remote Sensing Group Project Note, RSG/95/1*, British Geological Survey, Keyworth, 10p.
- Mather, P.M., 1976. *Computational methods of multivariate analysis in physical geography*. Wiley, London. 532p.
- Milton, E.J. and Rollin, E.M. 1987. *The GER IRIS Mk.IV Spectroradiometer: A Guide for UK users*. Department of Geography, University of Southampton, 138p.
- Morgan, D. J. and Inglethorpe, S. D. J, 1990. Report on visit to the Egyptian Geological Survey and Mining Authority (EGSMA), Cairo. 22 January-2 February, 1990. *British Geological Survey Technical Report, WG/90/1R*, British Geological Survey, Keyworth.
- O'Connor, E. A. 1987. Lithotectonic mapping in the central Eastern desert, Egypt, using enhanced TM imagery. In Matheis G. and Schandelmeier (eds.). *Current Research in African Earth Sciences*, Balkema, Rotterdam.
- O'Connor, E.A. 1991. Remote sensing techniques in detecting construction materials in arid regions: Egypt. *BGS Internal Interim Report*, Keyworth, UK, 5p.
- O'Connor, E.A. and Marsh S.H. 1992. Visit to Egypt. *British Geological Survey Technical Report, WC/92/14/R*, British Geological Survey, Keyworth.
- Prior, S. V. 1992. Mineralogical analyses of rock samples from Egypt. *British Geological Survey Technical Report, MPSR/92/8*, British Geological Survey, Keyworth.

- Razek, M.A., Ramadan, T., Tamom, S. and Refat, M. 1993. A note on china clay from the Abu Zenima area, SW Sinai, Egypt. *EGSMA Internal Report*, 2p.
- Said, R. 1962. *The Geology of Egypt*. Elsevier, Amsterdam. 377p.
- Schneider, G.I.C. and Diehl, B.J.M. 1991. Industrial rocks, Mineral Resources Series. *Open File Report, MRS 34*, Ministry of Mines and Energy, Geological Survey, Namibia, 92p.
- Schreuder, C.P. 1980. Verkenningsondersoek van klei-afsettings lang die Okavango Rivier. *Open File Report, EG 034*, Ministry of Mines and Energy, Geological Survey, Namibia.
- Switzer, P., Kowalik, W.S. & Lyon, R.J.P. 1981. Estimation of atmospheric path-radiance by the covariance matrix method. *Photogrammetric Engineering and Remote Sensing*, **47**, 1469-1476.
- Tsuchida, T., Odajima, T., Mirua, T., Tanaka, S., and Mouat, D.A. 1994. Spectral pattern analysis for geobotanical discrimination of rock types. *Proceedings of the Tenth Thematic Conference on Geologic Remote Sensing, San Antonio, Texas, I*, 321-322.
- Qari, M.Y.H.T. 1989. Lithological mapping and structural analysis of the Proterozoic rocks in part of the Arabian Shield using Landsat images. *International Journal of Remote Sensing*, **10**, 499-503.
- Qusa, M.E. 1986. *Clay in Egypt: a commodity package*. USAID Project, **263-0105**, EGSMA, Cairo, 60p.
- Van der Merwe, J.H. 1983. *National Atlas of South West Africa (Namibia)*. Institute for Cartographic Analysis, University of Stellenbosch and Directorate of Development Co-ordination, SWA. Cape Town.
- Wang, G., & Nunez, M. 1992. A new method of estimating path radiance for band ratio applications. *International Journal of Remote Sensing*, **13**, 527-539.
- Zussman, J. 1967. *Physical Methods in Determinative Mineralogy*. Academic Press. London. 514p.

## APPENDIX. LABORATORY DATA AND SAMPLE SITES

*Synopsis: This appendix gives information about the spectra contained in T-Spectra's libraries, samples collected in NE Namibia and the XRD analyses carried out on them. It may be of interest to our counterparts in Egypt and Namibia or geologists working in these areas in the future.*

### 1.1 T-Spectra spectral libraries

The following spectral libraries were installed for this project:

MINLIB	JPL pure mineral spectra
TMLIB	JPL pure mineral spectra, resampled to the TM bandpasses
JERSLIB	JPL pure mineral spectra, resampled to the JERS-1 bandpasses
ROCKLIB	Various BGS rock sample spectra
VEGLIB	Various EPFS and BGS vegetation spectra
EGYPT	Spectra of project samples collected in Egypt
NAMIBIA	Spectra of project samples collected in Namibia
IMAGELIB	TM pseudospectra extracted from the project imagery

#### 1.1.1 MINLIB

Spectra in C:\TSPECTRA\SPECTRA\MINLIB

ACTINOLI.1	ACTINOLI.2	ACTINOLI.3	ALBITE.1
ALBITE.2	ALBITE.3	ALMANDIN.1	ALMANDIN.2
ALMANDIN.3	ALUNITE.1	ALUNITE.2	ALUNITE.3
ALUNITE.4	ALUNITE.5	ALUNITE.6	AMBLYGON.1
AMBLYGON.2	AMBLYGON.3	AMBLYGON.4	AMBLYGON.5
AMBLYGON.6	ANALCIME.1	ANATASES.1	ANDESINE.1
ANDESINE.2	ANDESINE.3	ANDRADIT.1	ANDRADIT.2
ANDRADIT.3	ANGLESIT.1	ANGLESIT.2	ANGLESIT.3
ANHYDRIT.1	ANHYDRIT.2	ANHYDRIT.3	ANHYDRIT.4
ANHYDRIT.5	ANHYDRIT.6	ANORTHIT.1	ANORTHIT.2
ANORTHIT.3	ANTHOPHY.1	ANTHOPHY.2	ANTHOPHY.3
ANTLERIT.1	ANTLERIT.2	ANTLERIT.3	APATITE.1
APATITE.2	APATITE.3	APHTHITA.1	APHTHITA.2
APHTHITA.3	ARSENOPY.1	ARSENOPY.2	ARSENOPY.3
ATACAMIT.1	ATACAMIT.2	ATACAMIT.3	AUGITE.1

AZURITE.1	AZURITE.2	AZURITE.3	BARITE.1
BARITE.2	BARITE.3	BERYL.1	BERYL.2
BERYL.3	BERYLBLA.1	BERYLBLA.2	BERYLBLA.3
BERYLBLA.4	BIOTITE.1	BIOTITE.2	BIOTITE.3
BORAX.1	BORAX.2	BORAX.3	BORNITE.1
BORNITE.2	BORNITE.3	BRUCITE.1	BRUCITE.2
BRUCITE.3	BUDDINGT.1	BUDDINGT.2	BUDDINGT.3
BYTOWNIT.1	CALCITE.1	CALCITE.10	CALCITE.11
CALCITE.12	CALCITE.13	CALCITE.14	CALCITE.15
CALCITE.2	CALCITE.3	CALCITE.4	CALCITE.5
CALCITE.6	CALCITE.7	CALCITE.8	CALCITE.9
CALCITEW.1	CALCITEW.2	CALCITEW.3	CASSITER.1
CASSITER.2	CASSITER.3	CELADONI.1	CELADONI.2
CELADONI.3	CELESTIT.1	CELESTIT.2	CELESTIT.3
CELESTIT.4	CELESTIT.5	CERUSSIT.1	CERUSSIT.2
CERUSSIT.3	CHABAZIT.1	CHALCOCI.1	CHALCOCI.2
CHALCOCI.3	CHALCOPY.1	CHALCOPY.2	CHALCOPY.3
CHLORITE.1	CHLORITE.10	CHLORITE.11	CHLORITE.12
CHLORITE.13	CHLORITE.14	CHLORITE.15	CHLORITE.16
CHLORITE.17	CHLORITE.18	CHLORITE.2	CHLORITE.3
CHLORITE.4	CHLORITE.5	CHLORITE.6	CHLORITE.7
CHLORITE.8	CHLORITE.9	CLINOZOI.1	CLINOZOI.2
CLINOZOI.3	COLEMANI.1	COLEMANI.2	COLEMANI.3
COLUMBIT.1	COLUMBIT.2	COLUMBIT.3	COOKEITE.1
COOKEITE.2	COOKEITE.3	CORDIERI.1	CORDIERI.2
CORDIERI.3	CORRENSI.1	CORRENSI.2	CORRENSI.3
CORUNDUM.1	CORUNDUM.2	CORUNDUM.3	CRISTOBA.1
CRYOLITE.1	CRYOLITE.2	CRYOLITE.3	CUMMINGT.1
CUMMINGT.2	CUMMINGT.3	DICKITE.1	DIOPSIDE.1
DIOPSIDE.2	DIOPSIDE.3	DIOPSIDE.4	DIOPSIDE.5
DOLOMITE.1	DOLOMITE.2	DOLOMITE.3	DOLOMITE.4
DOLOMITE.5	DOLOMITE.6	DOLOMITE.7	DOLOMITE.8
DOLOMITE.9	ENSTATIT.1	ENSTATIT.2	ENSTATIT.3
ENSTATIT.4	ENSTATIT.5	EPIDOTE.1	EPIDOTE.2
EPIDOTE.3	EPIDOTE.4	EPIDOTE.5	EPIDOTE.6
EPIDOTE.7	EPIDOTE.8	EPIDOTE.9	FAYALITE.1
FAYALITE.2	FAYALITE.3	FERROAXI.1	FERROAXI.2
FERROAXI.3	FLUORITE.1	FLUORITE.2	FLUORITE.3
FLUORITE.4	FLUORITE.5	FLUORITE.6	FORSTERI.1
GAHNITE.1	GAHNITE.2	GAHNITE.3	GALENA.1
GALENA.2	GALENA.3	GIBBSITE.1	GLAUBERI.1
GLAUBERI.2	GLAUBERI.3	GLAUCONI.1	GLAUCONI.2
GLAUCONI.3	GLAUCONI.4	GLAUCONI.5	GLAUCONI.6
GLAUCOPH.1	GLAUCOPH.2	GLAUCOPH.3	GLAUCOPH.4
GLAUCOPH.5	GOETHITE.1	GRAPHITE.1	GRAPHITE.2
GRAPHITE.3	GROSSULA.1	GROSSULA.2	GROSSULA.3
GROSSULA.4	GYPSUM.1	GYPSUM.2	GYPSUM.3
GYPSUM.4	GYPSUM.5	GYPSUM.6	GYPSUM.7

GYPSUM.8	GYPSUM.9	HALITE.1	HALITE.2
HALITE.3	HALONREF.1	HALONVSH.1	HEDENBER.1
HEDENBER.2	HEMATITE.1	HEMATITE.2	HEMATITE.3
HEMATITE.4	HEMIMORP.1	HEMIMORP.2	HEMIMORP.3
HORNBLN.1	HORNBLN.2	HORNBLN.3	HOWLITE.1
HOWLITE.2	HOWLITE.3	HOWLITE.4	HOWLITE.5
HOWLITE.6	HOWLITE.7	HOWLITE.8	HOWLITE.9
HYDROXYA.1	HYDROXYA.2	HYDROXYA.3	HYPERSTH.1
ILLITE.1	ILLITE.2	ILLITE.3	ILLITE.4
ILLITE.5	ILLITE.6	ILLITE.7	ILLITE.8
JAROSITE.1	JAROSITE.2	JAROSITE.3	JOHANNSE.1
JOHANNSE.2	JOHANNSE.3	KAOLINIT.1	KAOLINIT.2
KAOLINIT.3	KAOLINIT.4	KAOLINIT.5	KAOLINIT.6
KAOLINIT.7	KERNITE.1	KERNITE.2	KERNITE.3
LABRADOR.1	LABRADOR.2	LABRADOR.3	LABRADOR.4
LABRADOR.5	LABRADOR.6	LEPIDOLI.1	LEPIDOLI.2
LEPIDOLI.3	LEPIDOLI.4	LEPIDOLI.5	LEPIDOLI.6
MAGNESIO.1	MAGNESIO.2	MAGNESIO.3	MAGNESIT.1
MAGNESIT.2	MAGNESIT.3	MAGNETIT.1	MAGNETIT.2
MAGNETIT.3	MALACHIT.1	MALACHIT.2	MALACHIT.3
MARCASIT.1	MARCASIT.2	MARCASIT.3	MICROCLI.1
MICROCLI.2	MICROCLI.3	MIMETITE.1	MIMETITE.2
MIMETITE.3	MIXEDLAY.1	MOLYBDEN.1	MOLYBDEN.2
MOLYBDEN.3	MONTEBRA.1	MONTEBRA.2	MONTEBRA.3
MONTEBRA.4	MONTEBRA.5	MONTEBRA.6	MONTMORI.1
MONTMORI.2	MONTMORI.3	MONTMORI.4	MONTMORI.5
MUSCOVIT.1	MUSCOVIT.2	MUSCOVIT.3	NATROJAR.1
NATROJAR.2	NATROJAR.3	NATROLIT.1	NATROLIT.2
NATROLIT.3	NEPHELIN.1	NEPHELIN.2	NEPHELIN.3
NONTRONI.1	NONTRONI.2	NONTRONI.3	NONTRONI.4
NONTRONI.5	OLIGOCLA.1	OLIGOCLA.2	OLIGOCLA.3
ORTHOCLA.1	ORTHOCLA.2	ORTHOCLA.3	PALYGORS.1
PLUMBOJA.1	PLUMBOJA.2	PLUMBOJA.3	PREHNITE.1
PREHNITE.2	PREHNITE.3	PYRITE.1	PYRITE.2
PYRITE.3	PYROLUSI.1	PYROLUSI.2	PYROLUSI.3
PYROPHYL.1	PYROPHYL.2	PYROPHYL.3	PYROPHYL.4
PYROPHYL.5	PYROPHYL.6	PYRRHOTI.1	QUARTZAL.1
QUARTZAL.2	QUARTZAL.3	QUARTZBL.1	QUARTZBL.2
QUARTZBL.3	QUARTZCH.1	QUARTZCH.2	QUARTZCH.3
QUARTZCH.4	QUARTZCH.5	QUARTZCH.6	QUARTZMI.1
QUARTZMI.2	QUARTZMI.3	QUARTZNO.1	QUARTZNO.2
QUARTZNO.3	QUARTZRO.1	QUARTZRO.10	QUARTZRO.11
QUARTZRO.12	QUARTZRO.2	QUARTZRO.3	QUARTZRO.4
QUARTZRO.5	QUARTZRO.6	QUARTZRO.7	QUARTZRO.8
QUARTZRO.9	QUARTZSA.1	QUARTZSA.2	QUARTZSA.3
QUARTZSM.1	QUARTZSM.2	QUARTZSM.3	REALGAR.1
REALGAR.2	REALGAR.3	RHODOCHR.1	RHODOCHR.2
RHODOCHR.3	RHODONIT.1	RHODONIT.2	RHODONIT.3

RUTILE.1	RUTILE.2	RUTILE.3	SANIDINE.1
SAPONITE.1	SCHEELIT.1	SCHEELIT.2	SCHEELIT.3
SCORODIT.1	SCORODIT.2	SCORODIT.3	SEPIOLIT.1
SEPIOLIT.2	SEPIOLIT.3	SEPIOLIT.4	SEPIOLIT.5
SEPIOLIT.6	SERPENTI.1	SERPENTI.2	SERPENTI.3
SERPENTI.4	SERPENTI.5	SERPENTI.6	SIDERITE.1
SIDERITE.2	SIDERITE.3	SILLIMAN.1	SILLIMAN.2
SILLIMAN.3	SMITHSON.1	SMITHSON.2	SMITHSON.3
SODALITE.1	SODALITE.2	SODALITE.3	SPHALERI.1
SPHALERI.2	SPHALERI.3	SPODUMEN.1	SPODUMEN.2
SPODUMEN.3	STIBNITE.1	STIBNITE.2	STIBNITE.3
STILBITE.1	STILBITE.2	STILBITE.3	STRONTIA.1
STRONTIA.2	STRONTIA.3	SULFUR.1	SULFUR.2
SULFUR.3	TALC.1	TALC.2	TALC.3
TALC.4	TALC.5	TALC.6	TALC.7
TALC.8	TALC.9	TINCALCO.1	TINCALCO.2
TINCALCO.3	TITANITE.1	TITANITE.2	TITANITE.3
TOPAZ.1	TOPAZ.2	TOPAZ.3	TOPAZWIT.1
TOPAZWIT.2	TOPAZWIT.3	TOURMALI.1	TOURMALI.2
TOURMALI.3	TREMOLIT.1	TREMOLIT.2	TREMOLIT.3
TREMOLIT.4	TREMOLIT.5	TREMOLIT.6	TRIPHYLI.1
TRIPHYLI.2	TRIPHYLI.3	TRIPHYLI.4	TRIPHYLI.5
TRIPHYLI.6	TRONA.1	TRONA.2	TRONA.3
TSCHERMI.1	TSCHERMI.2	TSCHERMI.3	ULEXITE.1
ULEXITE.2	ULEXITE.3	VERMICUL.1	VERMICUL.2
VERMICUL.3	VERMICUL.4	VERMICUL.5	VERMICUL.6
VESUVIAN.1	VESUVIAN.2	VESUVIAN.3	WITHERIT.1
WITHERIT.2	WITHERIT.3	WOLLASTO.1	WOLLASTO.2
WOLLASTO.3	ZINCITES.1	ZIRCON.1	ZIRCON.2
ZIRCON.3			

### 1.1.2 TMLIB

Spectra in C:\TSPECTRA\SPECTRA\TMLIB

ACTINOLI.TM	ALBITE.TM	ALMANDIN.TM	ANDRADIT.TM
ANHYDRIT.TM	ANORTHIT.TM	ANTHOPHY.TM	APATITE.TM
AUGITE.TM	BARITE.TM	BIOTITE.TM	BRUCITE.TM
CALCITE.TM	CHLORITE.TM	CORUNDUM.TM	DIOPSIDE.TM
DOLOMITE.TM	ENSTATIT.TM	EPIDOTE.TM	FAYALITE.TM
FORSTERI.TM	GIBBSITE.TM	GLAUCOPH.TM	GOETHITE.TM
GRAPHITE.TM	GROSSULA.TM	GYP SUM.TM	HALITE.TM
HEDENBER.TM	HEMATITE.TM	HORNBLN.TM	HYPERSTH.TM
ILLITE.TM	KAOLINIT.TM	MAGNETIT.TM	MONTMORI.TM
MUSCOVIT.TM	ORTHOCLA.TM	QUARTZCR.TM	QUARTZCH.TM
QUARTZMI.TM	QUARTZRC.TM	QUARTZRO.TM	QUARTZSA.TM
QUARTZSM.TM	RUTILE.TM	SERPENTI.TM	SIDERITE.TM
SILLIMAN.TM	TALC.TM	TREMOLIT.TM	TRONA.TM

### 1.1.3 JERSLIB

Spectra in C:\TSPECTRA\SPECTRA\JERSLIB

ACTINOLI.JER	ALBITE.JER	ALMANDIN.JER	ANDRADIT.JER
ANHYDRIT.JER	ANORTHIT.JER	ANTHOPHY.JER	APATITE.JER
AUGITE.JER	BARITE.JER	BIOTITE.JER	BRUCITE.JER
CALCITE.JER	CHLORITE.JER	CORUNDUM.JER	DIOPSIDE.JER
DOLOMITE.JER	ENSTATIT.JER	EPIDOTE.JER	FAYALITE.JER
FORSTERI.JER	GIBBSITE.JER	GLAUCOPH.JER	GOETHITE.JER
GRAPHITE.JER	GROSSULA.JER	GYPSUM.JER	HALITE.JER
HEDENBER.JER	HEMATITE.JER	HORNBLN.JER	HYPERSTH.JER
ILLITE.JER	KAOLINIT.JER	MAGNETIT.JER	MONJERORI.JER
MUSCOVIT.JER	ORTHOCLA.JER	QUARTZCR.JER	QUARTZCH.JER
QUARTZMI.JER	QUARTZRC.JER	QUARTZRO.JER	QUARTZSA.JER
QUARTZSM.JER	RUTILE.JER	SERPENTI.JER	SIDERITE.JER
SILLIMAN.JER	TALC.JER	TREMOLIT.JER	TRONA.JER

### 1.1.4 ROCKLIB

Spectra in C:\TSPECTRA\SPECTRA\ROCKLIB

**Peru** (Remote Sensing Group)

PERUGRAN.IM4 Granite, crushed

**Egypt** (Remote Sensing Group)

EGSERPEN.IM4		Serpentinite, fresh (Eugene O'Connor)
EGGRANOD.IM4		Granodiorite, fresh (Eugene O'Connor)
EGGABBRO.IM4		Gabbro, fresh (Eugene O'Connor)
EGDACITE.IM4		Dacite, weathered (Eugene O'Connor)
EGANDESI.IM4		Andesite, fresh (Eugene O'Connor)
EGSANDST.IM4	8w	Sandstone, weathered (Stuart Marsh)

**Kenya** (Peter Dunkley, International Division)

Emuruangolak Volcano, North Kenya Rift

KEBASLT1.IM4	100	Basalt, fresh
KETRACH1.IM4	142	Trachyte, fresh
KESYENIT.IM4	98	Syenite, fresh

Barrier Volcano, North Kenya Rift

KEBASLT2.IM4	234	Basalt, fresh
KETRACH2.IM4	221	Trachyte, fresh
KEPHONOL.IM4	216	Phonolite, fresh

## Zimbabwe (Peter Pitfield, International Division)

ZIGNEISS.IM4		Biotite Gneiss, fresh
ZIGREENS.IM4		Greenstone, weathered
ZIGRANUL.IM4		Granulite, fresh
ZIFENITE.IM4		Fenitised Gneiss, fresh

## Australia (Stuart Marsh, PhD samples)

AUSQUART.IM4	257w	Quartzite, weathered
AUSCHIST.IM4	27w	Mica Schist, weathered
AUSGRANI.IM4	5w	Granite, weathered

## Jordan (John Powell, Thematic Maps and Onshore Surveys Division)

JOLIMEST.IM4	JHP13	Limestone, fresh
JOPHOSPH.IM4	JHP2	Phosphorite, fresh
JOCHALK.IM4	JHP6	Chalk, fresh
JOCHERT.IM4	JHP21	Chert, fresh

## 1.1.5 VEGLIB

Spectra in C:\TSPECTRA\SPECTRA\VEGLIB

Basic spectra	GREENVEG.IM4	Leaf, Durham, UK
	DRYVEG.IM4	Dead wood, Australian outback
Temperate areas	GRASS1.IM4	Grass
	SCTPINE.IM4	Scotts Pine Leaves
	BARL1.IM4	Barley Leaves
	GRASS2.IM4	Grass
	SYCAM.IM4	Sycamore Leaves
	NBSAND.IM4	Newborough Warren Sand
	SITSPR.IM4	Sitka Spruce Leaves
	HAZEL.IM4	Hazel Leaves
	CALFLS.IM4	Calluna Flowers
	CALLVS.IM4	Calluna Leaves
	BARL2.IM4	Barley Leaves
	EURLARCH.IM4	European Larch Leaves
	WETSOI.IM4	Wet Soil
	PTERID.IM4	Pteridium Leaves
	PEAT.IM4	Peat
	DCALLVS.IM4	Dry Calluna Leaves
	ELAEAG.IM4	Elaeagnus Leaves (variegated)
	GORFLS.IM4	Gorse Flowers
	PRUN.IM4	Prunus Leaves
	DRYSOI.IM4	Dry Soil

Tropical areas	TLEAF2.IM4 TLEAF5.IM4 TLEAF7.IM4 TLEAF11.IM4	Vanilla leaf Cocoa leaf - orange/green Rubber leaf Breciaceae leaf
Mediterranean areas	CYST8.IM4 EU2.IM4	Cystus speciex Eucalyptus

### 1.1.6 Others

The reflectance spectra of all project samples were measured and stored in the libraries EGYPT and NAMIBIA. IMAGELIB was used to store image pseudospectra.

## 1.2 Sample sites and XRD results for Namibia

Figures A1.1 to A1.7 show the sample sites for the NE Namibia field area. The XRD results for those samples are listed in Table A1.1.

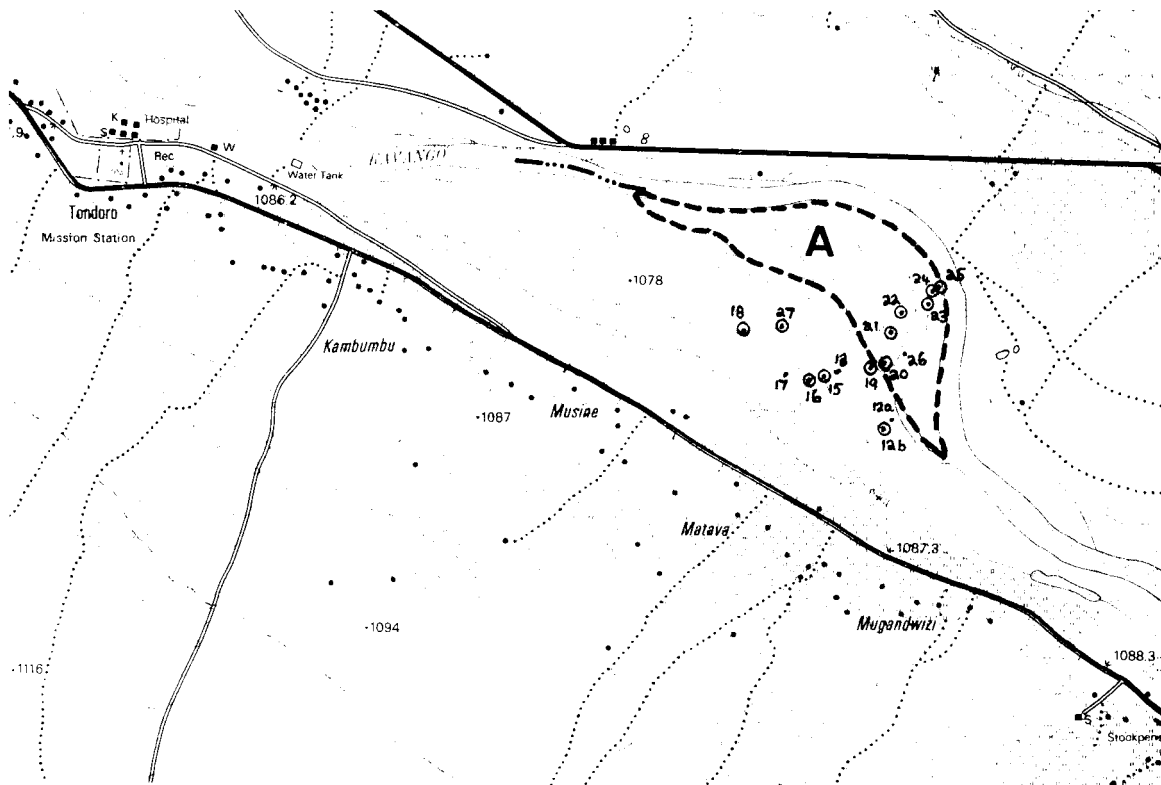


**Figure A1.1** Location map at 1:50 000 scale of the area field-checked near Tondoro. The clay deposit marked A is from Schreuder (1980). In this and the following figures, the clay samples for XRD analysis were taken from the localities ringed by a circle.

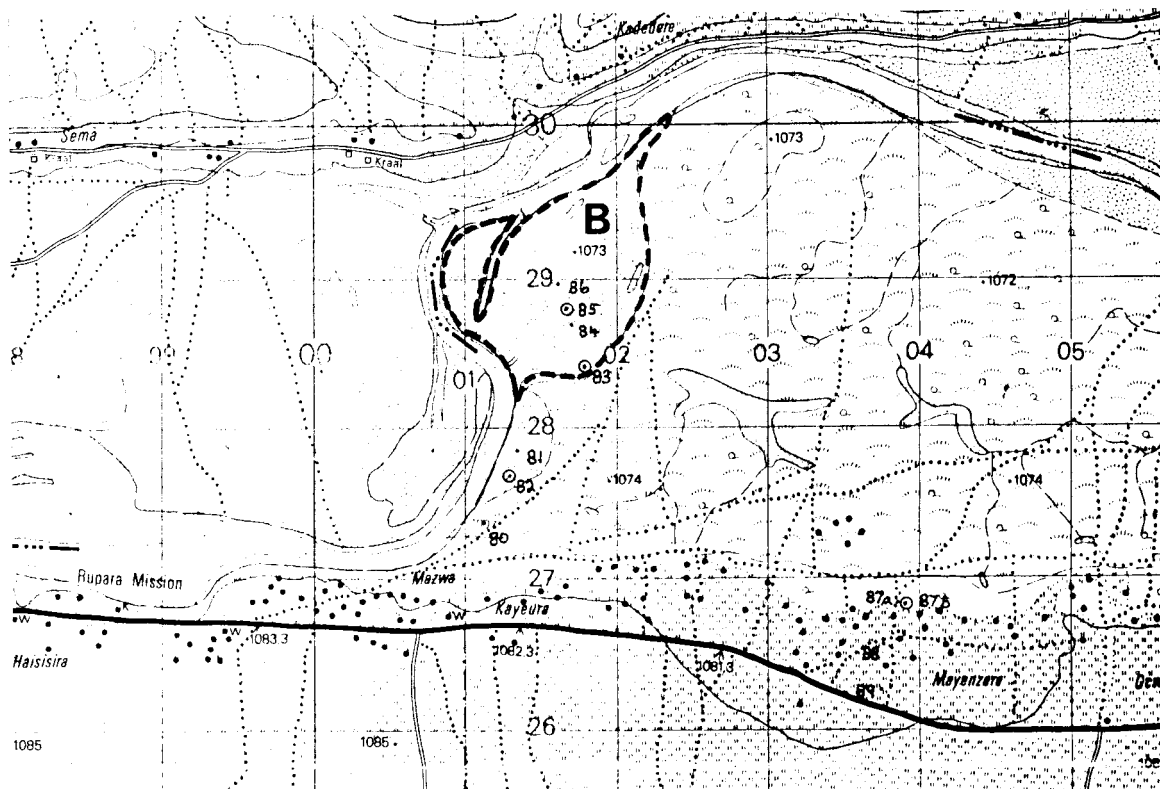


**Figure A1.2** Location map at 1:50 000 scale of the area field-checked near Rupara Mission. The clay deposit marked B is from Schreuder (1980).

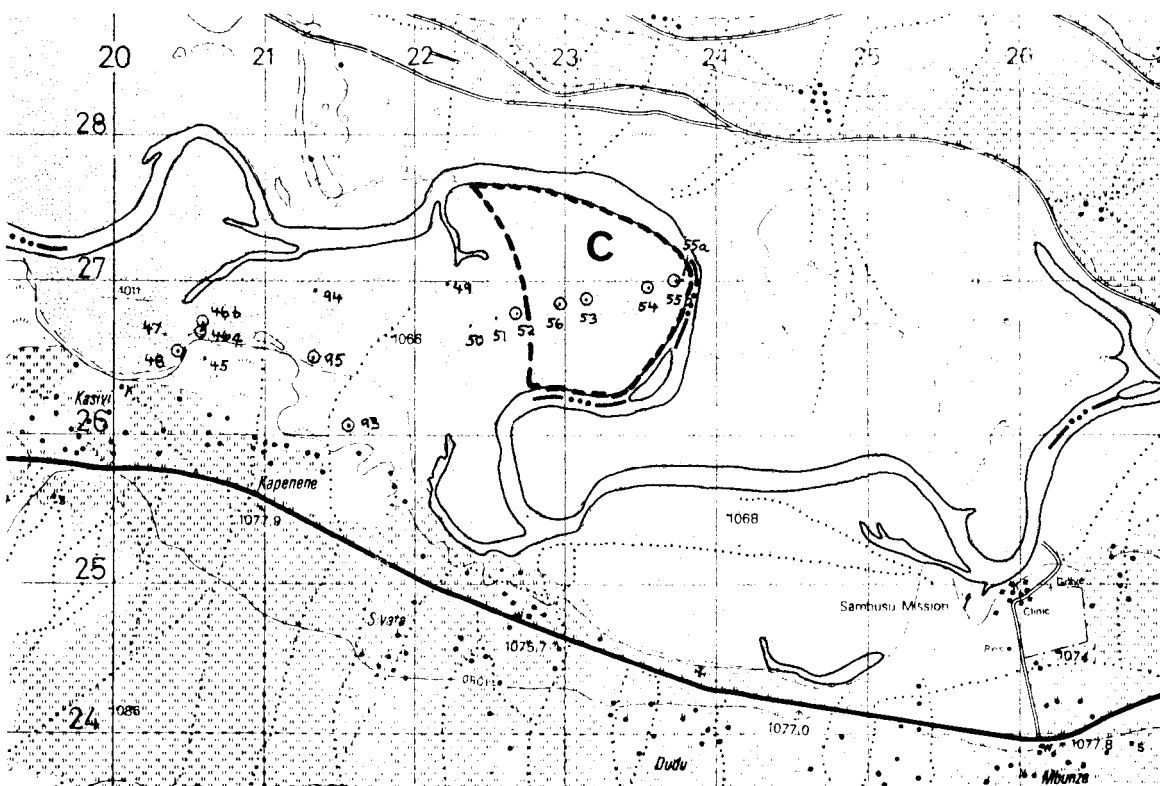


**Figure A1.3** Location map at 1:50 000 scale of the area field-checked near Sambusiu Mission. The clay deposit marked C is from Schreuder (1980).

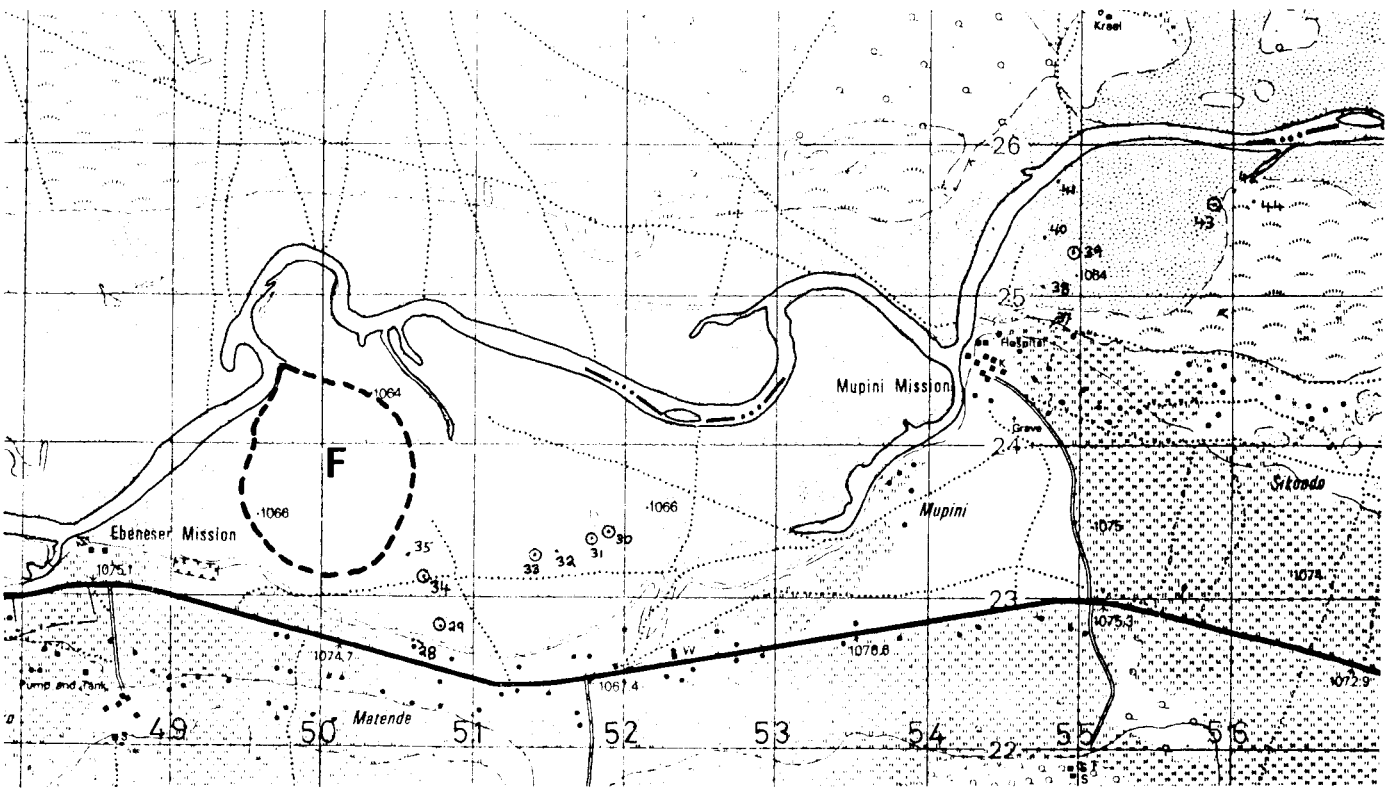


Figure A1.4 Location map at 1:50 000 scale of the area field-checked near Ebeneser and Mupini Missions. The clay deposit marked F is from Schreuder (1980).

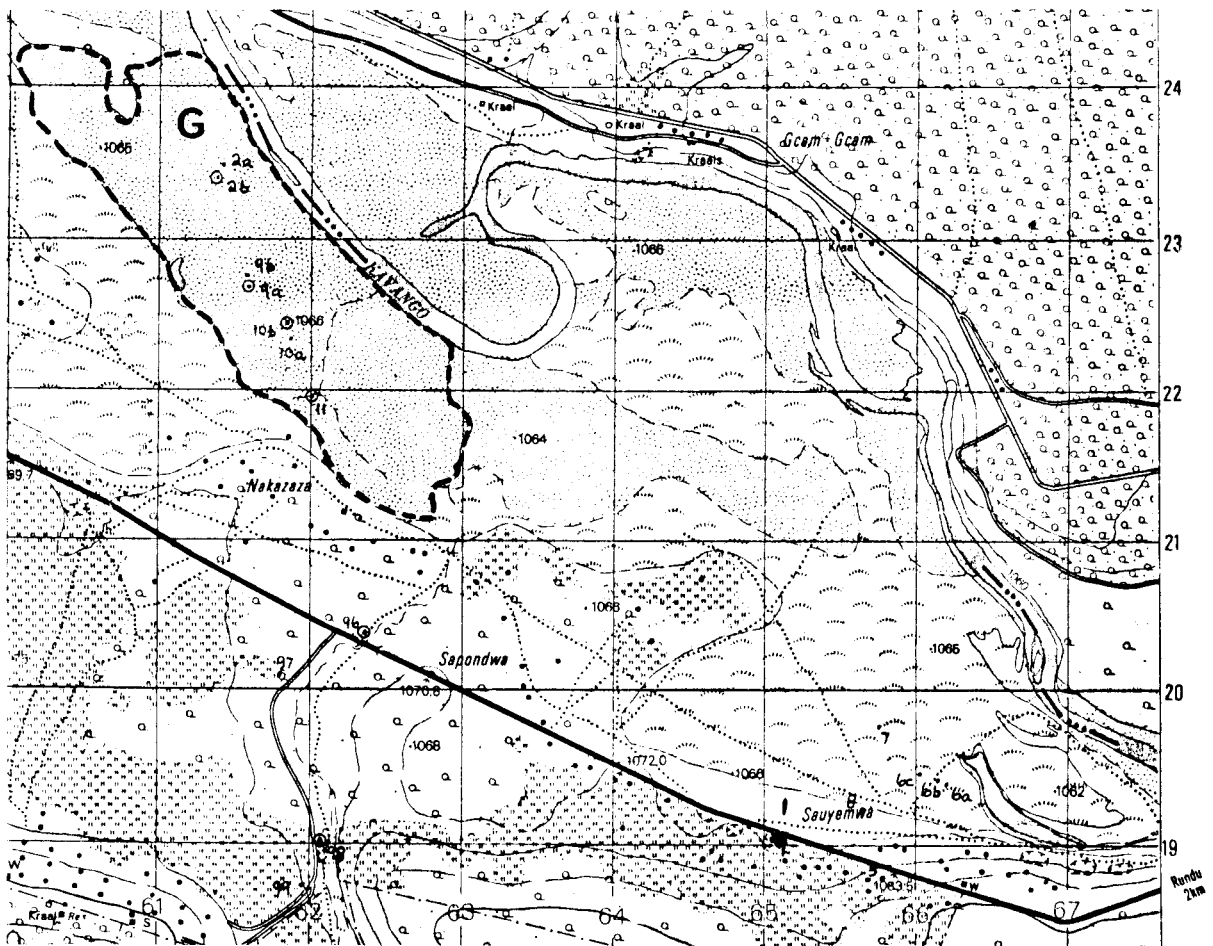
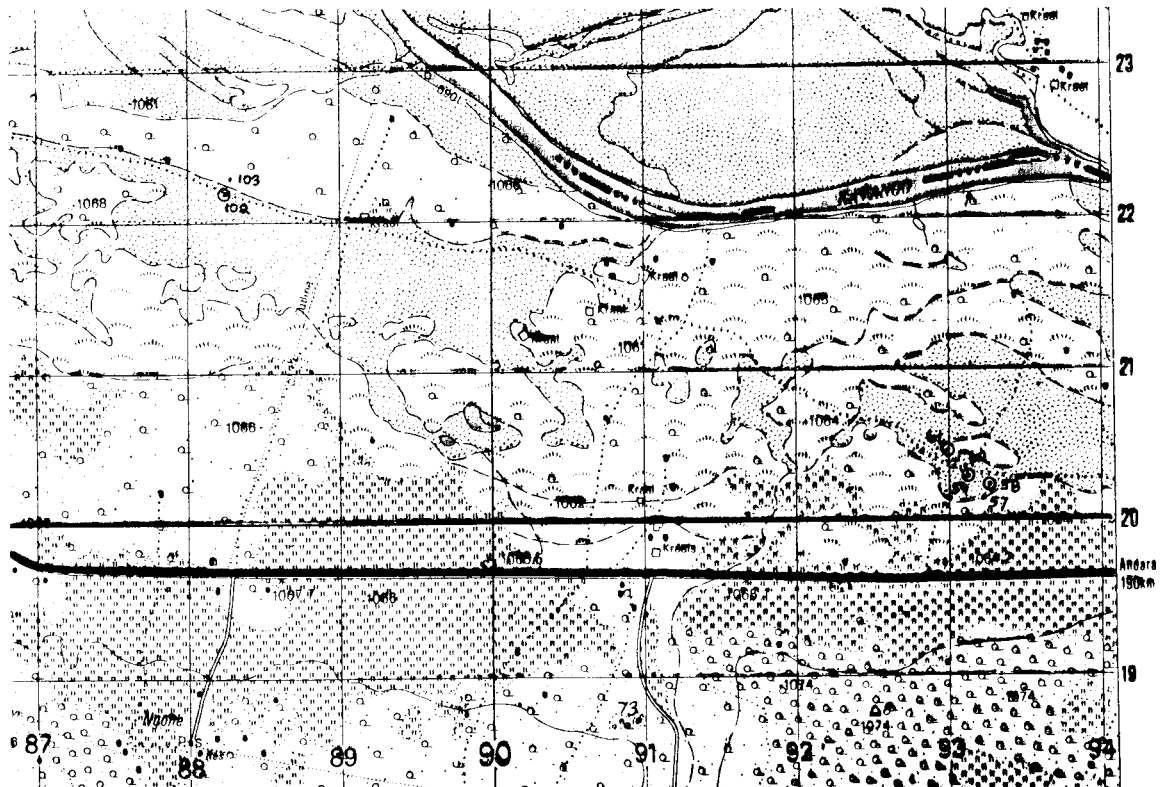
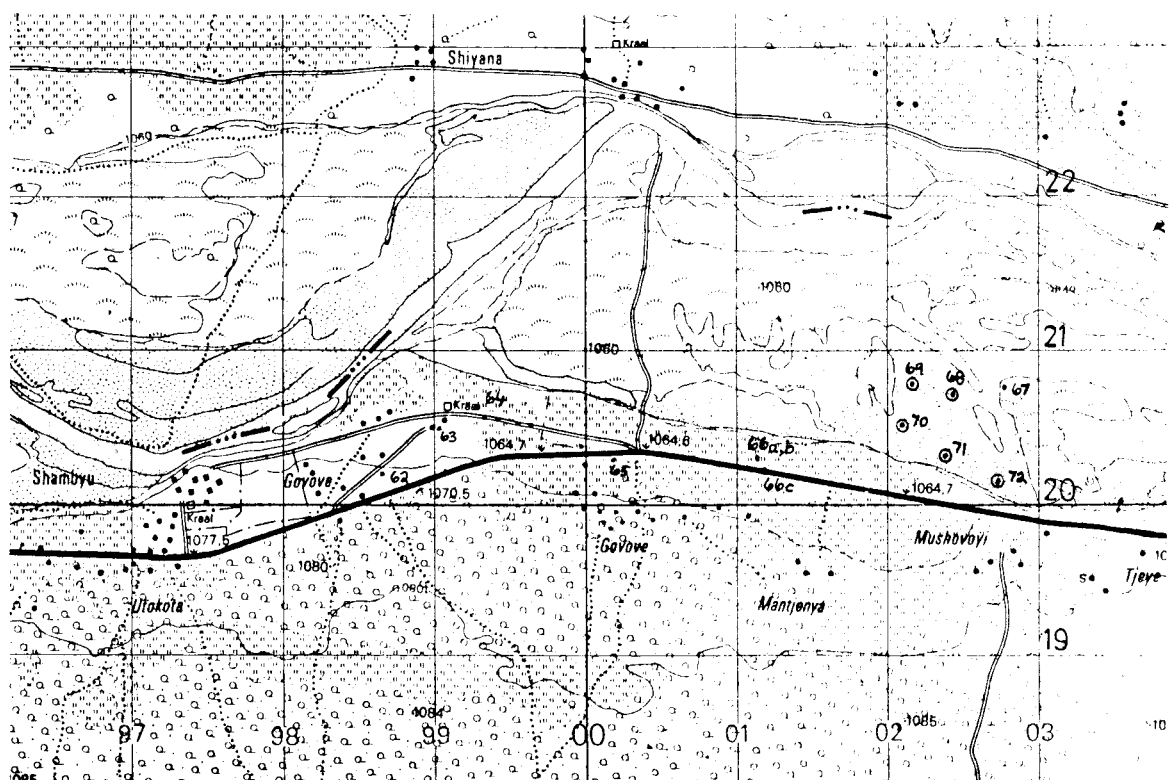


Figure A1.5 Location map at 1:50 000 scale of the area field-checked near Nakazaza and Sauyemwa, west of Rundu. The clay deposit marked G is from Schreuder (1980).



**Figure A1.6** Location map at 1:50 000 scale of the area field-checked between 18 and 23 km east of Rundu.



**Figure A1.7** Location of the area field-checked between 1 and 5 km east of Shambyu, on the Mashari 1:50 000 sheet.

**Table A1.1** List of XRD results of clays from the Okavango River flood-plain, including 3 samples from the Otavi brickworks.

XRD SAMPLE	1:50 000 SHEET	GRID REFERENCE	XRD RESULTS (BULK) Major + + + Minor + + Present + Trace ~	CLASSIFIED XRD SOIL-TYPE	HAND SPECIMEN DESCRIPTION
9A	MUPINI	6160E 2269N	+ + + quartz, ~ montmorillonite	clayey SAND	CLAY
10B	MUPINI	6185E 2245N	+ + + quartz, ~ montmorillonite	clayey SAND	grey CLAY
11	MUPINI	6200E 2195N	+ + quartz, + chlorite, + kaolinite	clayey SILT	medium grey CLAY
12B	TONDORO	?	+ + + quartz, ~ montmorillonite	clayey SAND	pale brown/buff CLAY, silty & sandy
15	TONDORO	?	+ + + quartz, ~ montmorillonite, ~ chlorite	clayey SAND	CLAY
16	TONDORO	?	+ + + quartz, + kaolinite, ~ montmorillonite, ~ chlorite	clayey SAND	CLAY, silty
18	TONDORO	?	+ + kaolinite, + quartz, ~ mica	silty CLAY	CLAY
19	TONDORO	?	+ + + quartz, + kaolinite, ~ montmorillonite	clayey SAND	light brown/grey CLAY, silty
20	TONDORO	?	+ + + quartz, + kaolinite, ~ montmorillonite, ~ chlorite	clayey SAND	light grey CLAY, silty & sandy
21	TONDORO	?	+ + + quartz, + kaolinite, ~ montmorillonite	clayey SAND	brown to buff CLAY, limonitic stains
22	TONDORO	?	+ + + quartz, + kaolinite, ~ montmorillonite	clayey SAND	light grey & or/br CLAY, silty
23	TONDORO	?	+ + + quartz, + kaolinite, ~ montmorillonite	clayey SAND	light grey & brown CLAY
24	TONDORO	?	+ + quartz, + kaolinite, + montmorillonite	clayey SILT	CLAY
25	TONDORO	?	+ + + quartz, + montmorillonite, ~ kaolinite	clayey SAND	light brown CLAY, silty
27	TONDORO	?	+ + + quartz, + + montmorillonite	clayey SAND	CLAY, silty
29	MUPINI	5080E 2280N	+ + quartz, + + kaolinite, + montmorillonite	silty CLAY	medium grey CLAY, sandy, silty
30	MUPINI	5190E 2343N	+ + + quartz, + kaolinite, + montmorillonite	clayey SAND	light brown, fine sandy, silty CLAY
31	MUPINI	5178E 2338N	+ + + quartz, ~ montmorillonite	clayey SAND	pale brown CLAY, silty, sandy
33	MUPINI	5140E 2328N	+ quartz, + kaolinite, ~ montmorillonite	clayey SILT	light grey, silty CLAY
34	MUPINI	5068E 2313N	+ + quartz, + + kaolinite	silty CLAY	light grey CLAY, very light weight
39	MUPINI	5495E 2530N	+ + quartz, + + kaolinite, ~ montmorillonite	sandy CLAY	grey & or/br fine sandy, silty CLAY

XRD SAMPLE	1:50 000 SHEET	GRID REFERENCE	XRD RESULTS (BULK) Major +++ Minor ++ Present + Trace ~	CLASSIFIED XRD SOIL-TYPE	HAND SPECIMEN DESCRIPTION
43	MUPINI	5589E 2560N	++ quartz, + kaolinite	clayey SILT	brownish grey CLAY, silty, limonitic
46A	SAMBUSU	2059E 2669N	++ quartz, + kaolinite, ~ montmorillonite	silty CLAY	light brown, silty CLAY, very light
46B	SAMBUSU	2060E 2673N	++ quartz, + montmorillonite, ~ kaolinite	clayey SAND	light brownish grey, silty, CLAY
48	SAMBUSU	2043E 2655N	++ quartz, + kaolinite, ~ montmorillonite	silty CLAY	dark brown/black CLAY, weathers grey
52	SAMBUSU	2269E 2680N	++ kaolinite, + quartz	CLAY	CLAY
53	SAMBUSU	2315E 2690N	++ quartz, + kaolinite, ~ montmorillonite	silty CLAY	dark, humic CLAY
54	SAMBUSU	2355E 2697N	++ quartz, + kaolinite	silty CLAY	CLAY
55B	SAMBUSU	2374E 2700N	++ kaolinite, + quartz, + montmorillonite	silty CLAY	CLAY
56B	SAMBUSU	2297E 2686N	++ quartz, + kaolinite, ~ montmorillonite	clayey SAND	CLAY, silty
58	RUNDU	9327E 2023N	++ quartz, + montmorillonite	clayey SAND	grey, humic, fine sandy, silty CLAY
59	RUNDU	9312E 2029N	++ quartz, + montmorillonite	clayey SAND	medium-light brown, sandy CLAY LOAM
61	RUNDU	9299E 2046N	++ quartz, + montmorillonite	clayey SAND	pale SANDY LOAM, medium-fine
66A	MASHARI	0113E 2030N	++ quartz, + montmorillonite	clayey SAND	brown silty SANDY LOAM, medium-fine
68	MASHARI	0244E 2072N	++ quartz, + kaolinite, ~ montmorillonite	clayey SILT	medium grey, fine sandy, silty CLAY
69	MASHARI	0218E 2080N	++ quartz, ~ montmorillonite	clayey SILT	pale brown, silty CLAY, very light
70	MASHARI	0210E 2052N	++ quartz, + montmorillonite, ~ kaolinite	clayey SAND	pale brown, silty CLAY, light
71	MASHARI	0240E 2032N	++ quartz, + montmorillonite	clayey SAND	light grey, silty, CLAY
72	MASHARI	0274E 2015N	++ montmorillonite, ++ quartz, + kaolinite	silty CLAY	light grey, silty CLAY, + calcrete
74	1724AD+BC	?	++ quartz, + montmorillonite	clayey SAND	light brown, fine sandy, silty LOAM
75	1724DC	?	++ quartz, + montmorillonite	clayey SAND	medium brown, fine sandy silty CLAY
76	1724DC	?	++ quartz, + montmorillonite, ~ kaolinite	clayey SAND	medium grey, fine sandy, silty CLAY

XRD SAMPLE	1:50 000 SHEET	GRID REFERENCE	XRD RESULTS (bulk) Major +++ Minor ++ Present + Trace ~	CLASSIFIED XRD SOIL-TYPE	HAND SPECIMEN DESCRIPTION
77	1724DC	?	+++quartz, ~ montmorillonite	clayey SAND	light brown, silty CLAY
78A	1724DC	?	+++quartz, ++ montmorillonite, + kaolinite	silty CLAY	grey, termite mound CLAY, silty
78B	1724DC	?	+++ montmorillonite, ++ quartz	silty CLAY	grey, CLAY, silty
78C	1724DC	?	not analysed	not analysed	medium grey CLAY, very light weight
82	RUPARA	0130E 2768N	+++ quartz, ++ kaolinite, ++ montmorillonite	silty CLAY	light brown/grey, silty CLAY
83	RUPARA	0180E 2840N	+++ quartz, ++ kaolinite, ~ montmorillonite	clayey SAND	light brown/grey, sandy, silty CLAY
84	RUPARA	0170E 2869N	+++ quartz, ++ kaolinite, ~ montmorillonite	silty CLAY	grey/brown, silty CLAY, very light
85	RUPARA	0167E 2880N	+++ quartz, ~ kaolinite	clayey SILT	grey/brown, silty CLAY, very light
86	RUPARA	0161E 2895N	+++ quartz, + kaolinite, + montmorillonite	clayey SAND	grey/brown, fine sandy, silty CLAY
87B	RUPARA	0391E 2683N	+++ quartz, + montmorillonite, ~ kaolinite	clayey SAND	grey, silty CLAY
93	SAMBUSU	2156E 2606N	+++ quartz, + + montmorillonite, ~ kaolinite	clayey SAND	CLAY & SAND mixture
95	SAMBUSU	2132E 2651N	+++ quartz, + kaolinite, + montmorillonite	clayey SAND	medium grey, fine sandy, silty CLAY
96	MUPINI	6237E 2038N	+++ quartz, + + + ?????	unknown	white powdery EFFLORESCENCE
98	MUPINI	6207E 1902N	?????	unknown	white, buff + yell/or EFFLORESCENCE
102	RUNDU	8826E 2220N	+++ quartz, + montmorillonite	clayey SAND	dark grey, sandy, silty CLAY
OTAVI 1	?	BRICKWORKS	+++ quartz, + montmorillonite	clayey SAND	crushed CLAY
OTAVI 2	?	BRICKWORKS	+++ quartz, + + mica, ~ montmorillonite	unknown	"scali" (talc ?)
OTAVI 3	?	BRICKWORKS	+++ quartz, ~ mica, ~ montmorillonite	clayey SAND	CLAY (from pit)